Spatiotemporal evolution of non-diffracting plasmonic pulses

Dissertation
zur Erlangung des akademischen Grades
doctor rerum naturalium (Dr. rer. nat.)

vorgelegt dem Rat der Physikalisch-Astronomischen Fakultät
der Friedrich-Schiller-Universität zu Jena

von M.Sc., M.Tech. Amit Vikram Singh
geboren am 03.05.1989 **in** Sultanpur, Indien

To my parents

Zusammenfassung

Beugung ist ein allgegenwärtiges Phänomen in der Optik. In den späten 80er Jahren wurden zur Auslösung der Beugung Bessel-Strahlen vorgeschlagen und beobachtet. Bessel-Strahlen breiten sich im freien Raum ohne Beugung aus, sie können jedoch nur in drei Dimensionen existieren. Im letzten Jahrzehnt hat sich nach der bahnbrechenden Arbeit von Siviloglou und Christodoulides über Airy-Strahlen erhebliches Interesse an nicht-beugenden Strahlen entwickelt. Da die Airy-Strahlen auch in zwei Dimensionen existieren können, eignen sie sich besonders für die planarephotonik, z. B. an Metall-Dielektrikum-Grenzflächen. In dieser Doktorarbeit wird die Erzeugung von Airy-Strahlen und deren Eigenschaften an der Metall-Dielektrikum-Grenzfläche eingehend untersucht. Der Kern dieser Arbeit untersucht die räumliche und raumzeitliche Entwicklung von Airy-Plasmonen. Ausreichendes Hintergrundwissen über elektromagnetische Theorie und numerische Methoden wurde dafür benötigt. Wir haben die räumlichen Eigenschaften von Airy-Plasmonen mit Hilfe der Photoemissions-Elektronenmikroskopie untersucht und eine rigorose Finite-Differenzen-Zeitbereichsmethode angewendet. Die Ergebnisse wurden auch durch die Verwendung einer Strahlpropagationsmethode (BPM) bestätigt. Die BPM bietet eine Simulationsmethode zur schnelleren Optimierung der Struktur des anregungsgitters der Airy-Plasmonen. Diese Arbeit quantifiziert weiter die Erzeugungseffizienz der nichtparaxialen Airy-Plasmonen eines Beugungsgitters. Es wurde eine breitbandige Erzeugungsbandbreite von Airy-Plasmonen gefunden, was einen gangbaren Weg zur Untersuchung von ultrakurz gepulsten Airy-Plasmonen darstellt. Das Beugungsgitter wurde optimiert, um die ultrakurzen Airy-Plasmonenpulse zu erzeugen. Die raumzeitliche Entwicklung von Airy-

Plasmonenpulsen wurde numerisch untersucht. Ein analytisches, semi-analytisches und numerisches Modell wurden eingesetzt, um die Trajektorie der zeitgemittelten Airy-Plasmonenpulse zu untersuchen. Zeitlich gemittelte Airy-Plasmonenpulse behalten die nicht-beugenden Eigenschaften wie ihre CW-Gegenstücke. Die Ergebnisse dieser Arbeit können bei der Entwicklung von gepulsten Airy-Airy plasmonischen Strahlen genutzt werden, die sich im Raum ohne Beugung und in der Zeit ohne Dispersion ausbreiten können. Diese sogenannten zweidimensionalen linearen 'light-bullets' können das verborgene Potenzial der Plasmonik freisetzen.

Abstract

Diffraction is a ubiquitous phenomenon in optics. In the late '80s to capture the diffraction, Bessel beams were proposed and observed. Bessel beams propagate in free space without diffraction, however, they can exist only in three dimensions. In the last decade, considerable interest has spurred in nondiffracting beams after the seminal work of Siviloglou and Christodoulides on Airy beams. Since the Airy beams can also exist in two dimensions, they are particularly suited for flat-land photonics *e. g.* the metal-dielectric interface. This thesis presents the in-depth study of Airy beams' generation and their properties on the metal-dielectric interface. The core of this thesis studies the spatial and spatiotemporal evolution of Airy plasmons. Sufficient background on electromagnetic theory and numerical methods has been provided to develop Airy plasmons theory. We have investigated the spatial properties of Airy plasmons using photoemission electron-microscopy and have performed a rigorous finite difference time domain method. The results were also confirmed by using a beam propagation method (BPM). The BPM provides an efficient simulation method to optimize the grating structure for exciting the Airy plasmons. This work further quantifies the nonparaxial Airy plasmons' generation efficiency of a diffraction grating. A broadband generation bandwidth of Airy plasmons was found, which provided a viable route to investigate ultrashort pulsed Airy plasmons. The diffraction grating has been optimized to generate the ultrashort Airy plasmon pulses. The spatiotemporal evolution of Airy plasmon pulses is investigated numerically. An analytical, semi-analytical, and physical model was developed and deployed to study the trajectory of time-averaged Airy plasmon pulses. Time-averaged Airy plasmon pulses retain the nondiffractive

properties akin to their CW counterparts. The results of this work can be utilized in engineering the pulsed Airy-Airy plasmonic beams, which can propagate in space without diffraction and in time without dispersion. These so-called two-dimensional linear 'light-bullets' can unleash the hidden potential of plasmonics.

Contents

I. Introduction

This introductory chapter provides an overview of the past and recent development in the Airy wave's research field. A vast plethora of information has been generated in this field. The chapter focuses on the Airy beams' generation, characteristics, and application, followed by the transformation of Airy beams' research knowledge into Airy plasmons. Eventually, an introduction and motivation to spatiotemporal Airy plasmon pulses are presented.

Optics has been playing a key role in the development of science. It has provided useful tools in the history of science for gathering information and building a knowledge base. The tools such as eyeglasses, microscope, telescope, camera, lasers have solved practical human problems and also have been instrumental in developing other areas of science. One of the recent breakthroughs in extreme ultraviolet optics has opened up doors for manufacturing 5 nm semiconductor chips and has brought a boom in the semiconductor industry. These tools can be put into three categories based on their evolution over time: geometrical optics, physical optics, and modern photonics. In this work, we are mainly concerned with a prominent subfield of modern photonics with emphasis on the light-matter interaction at the nanometer scale.

In this thesis, the classical electromagnetic description of modern photonics is considered. The electromagnetic description involves light's properties such as intensity, direction, coherence, phase, and polarization. The mathematical framework of electromagnetic optics is provided by Maxwell's equation. The solution of the wave equation spreads in space upon propagation. Optics researchers have always been interested in finding a propagation invariant solution to Maxwell's equation. The quest

for finding nonspreading localized wave packets has attracted attention since the late 80s after the seminal work of Berry and Balazs [1] in the context of quantum mechanics. They proposed theoretically that the Schrödinger equation [2] describing a free particle can exhibit a nonspreading Airy wave packet solution. As pointed out in Berry's paper, this Airy wave packet happens to be the only nontrivial solution in one dimension (1D). The Airy wave packet corresponds to a family of orbit and the envelope of the family of the orbit (also known as caustic) accelerates even in free space. The work remained hibernated due to difficulty in preparing such quantum states and realizing it experimentally. However, in the same decade, an interesting class of nonspreading or nondiffracting wave configurations was introduced in two and three dimensions (2D and 3D) in the area of optics and atom physics [3–8]. The mathematical analogy between the Schrödinger equation and the paraxial wave equation has helped the ideas to sail from the quantum mechanics world to the optics world. In addition, optics has provided a fertile ground for the experimental realization of such nonspreading waves. Perhaps, the most famous example of such 2D nondiffracting beams is the so-called 'Bessel beams'. First introduced [3] and experimentally realized [4] by Durnin et al., Bessel beams have sparked considerable interest in finding other classes of nondiffracting beams. The interest has not only spurred into finding the solution of the paraxial wave equation (PWE) but also to find a generic class of solutions of 3D Helmholtz equations (HE). These generic classes are also known as propagation invariant optical fields (PIOF) [5, 9–11]. A comprehensive review by Turunen and Friberg [11] on PIOF has included the discussion of custom designs, vectorial extension, and partial coherence. Over the years, many reviews have been presented on nondiffracting waves [11–15], each having its focus. Particularly, a review on 'Light modes of free space' by Levy et al. [15] classifies the solution sets of free space of Maxwell's equations. The classification divides Waves (solution of the Helmholtz equations) and Beams (solution of the paraxial wave equation) into four coordinate systems. The four waves, plane waves, Bessel waves, Weber waves, and Mathieu waves are solutions of the exact Helmholtz equation corresponding to

space	time	spacetime
Airy infinite beams Airy finite beams Airy-Airy beams Airy-Plane beams **Airy plasmons**	**Gaussian pulses** Airy pulses	Airy²-Airy pulsed beams **Airy plasmon pulses**

Table I.1. Classification of Airy waves based on natural dimensions of electromagnetics: space, time, and spacetime. Texts shown in red color are areas of our research work.

cartesian, circular-cylindrical, parabolic-cylindrical, and elliptical-cylindrical coordinate systems respectively. Similarly, there are 14 beam solutions of the partial wave equation in four coordinate systems. A summary of this classification can be found in Table 1 of reference [15]. The PWE solution in the cartesian coordinate system has a special type of nonspreading beams known as Airy beams. The Airy beam is our main focus of interest in this thesis; however, our exploration is not limited to free space. This work investigates Airy beams and their properties on the metallic surface in different dimensions of space, time, and spacetime.

We provide a classification based on this research work in Table I.1. This work is devoted to Airy plasmons and their evolution in space and time. Therefore, only a cartesian coordinate system is considered. In electromagnetics, space and time are the natural dimensions so we begin first by classifying in terms of dimensions: space, time, and spacetime. In space, Airy plasmons are investigated in Chapter III. In the time domain, only Gaussian pulse is considered. Combining space (Airy plasmons) and time (Gaussian pulse) provides an interesting insights into nonspreading wave packets and is presented in Chapter IV.

The first column of Table I.1 briefly presents the research development in the area of Airy beams over the last decade. Airy beams have been extensively studied by different research groups. Tremendous research work has been devoted to theoretical and ex-

perimental investigations and a large number of applications has been demonstrated. Airy infinite beams are solutions of the 1D paraxial wave equation and have been derived in direct analogy with the Airy nondispersive solution of the quantum mechanical Schrödinger equation [1]. Airy beams like other types of propagation-invariant beams, carry infinite energy, which is a direct outcome of their nondiffracting nature. However, unlike other propagation invariant beams, Airy beams cannot be generated by using the conical superposition of plane waves. The characteristic property of Airy infinite beams is their ability to freely accelerate even in the absence of any index gradients. Perhaps, the self-accelerating property makes Airy beams unique among other types of nondiffracting beams. The self acceleration does not violate Ehrenfest's theorem, which describes the motion of the center of gravity of a wave packet [16, 17]. In the case of Airy infinite beams, the center of gravity is not defined due to the infinite extent of the beams in the transverse direction. An alternative explanation to the freely accelerating beams was given by Greenberger through the principle of equivalence [18]. A ray optics description of Airy beams can be carried out by solving the Rayleigh-Sommerfeld diffraction formula as shown in reference [19]. The fundamental principles of ray optics and catastrophe theory can be utilized to gain a deeper theoretical understanding of Airy beams, particularly the trajectory of parabolic caustics and their formation from straight rays [1, 20, 21].

Airy infinite beams are not possible to realize experimentally. Finite energy Airy beams can be realized using a truncated initial Airy function. The truncated finite energy Airy beams are achieved using different types of aperture functions [10, 22, 23]. The First solution of Airy finite beams was provided by Siviloglou and Christodoulides [10], almost three decades after Berry and Balazs' pioneering work. This work has been a big leap in terms of understanding Airy waves. It has been well understood that what matters is not the trajectory of the 'center of mass,' but the curved evolution of the field itself. The interaction of particles or other waves with Airy beams happens due to accelerating local field structures. As mentioned in Siviloglou and Christodoulides' seminal work, an exponential aperture function was taken to ensure

the containment of the infinite Airy tail to produce Airy beam with finite energy. The exponentially apodized Airy function is used as the initial condition to solve the paraxial wave equation. The finite energy solution was found to possess the most important characteristics of Airy waves i.e. its ability to freely accelerate. The truncated finite energy Airy beam is not strictly nondiffracting. The diffraction of the Airy finite beam depends on the attenuation parameter of the aperture function, which can be controlled to make the beam almost nondiffracting over the desired propagation distance. The finite energy and finite transverse extent of the Airy beam can be experimentally realized using several different methods [24–29]. A common method for generating an Airy beam is the use of a spatial light modulator (SLM) for imposing an appropriate phase map on an input beam. The Fourier spectrum (or angular spectrum) of a truncated Airy beam consists of a Gaussian with a cubic phase resulting from the Fourier transform of the Airy function itself. This angular spectrum is obtained by imposing a cubic phase with an SLM on a broad Gaussian. A typical experimental setup [24] involves a continuous-wave (CW) laser, an SLM, a detector (CCD), and a cylindrical lens. A linearly polarized collimated fundamental Gaussian beam is reflected from the front facet of the computer-controlled SLM. The SLM imposes the cubic phase on the Gaussian beam which is then converted to a 1D Airy beam using a cylindrical lens placed at its focal distance from the SLM. The 1D Airy beam is then carefully imaged on the CCD through a microscopic objective.

Airy beams in two dimensions were first suggested by Besieris et al. [30]. In the context of optics, Bandres [31] has presented a complete theory of accelerating beams. There exist a one-to-one correspondence between accelerating solutions of the paraxial wave equation and solutions of the two-dimensional linear potential Schrödinger equation. Therefore, the solution of the linear potential Schrödinger equation can be used to find all possible solutions of accelerating beams. A general approach was developed by providing a canonical form (Equation 11 in reference [31]) in Fourier space. In this paper, it was concluded that there are unique line spectra for each accelerating beam. The line spectrum of the accelerating beam is analogous to the angular

spectrum of nondiffracting beams. A novel accelerating beam can be created using different line spectra. However, Airy and parabolic accelerating beams are the only two explicit closed-forms of complete and orthogonal accelerating beams. The line spectra of the orthogonal families of accelerating beams can be found in Table 1 of reference [31]. The Fourier spectrum of Airy-Airy beams is simply a two-dimensional extension of 1D Airy beams. It is generated experimentally in a similar fashion as the 1D Airy beams. Instead of imposing a 1D cubic phase, we now imprint a 2D cubic phase using an SLM and the cylindrical lens is replaced with a spherical lens for performing a 2D Fourier transformation. Besides using an SLM, Airy beams can also be formed utilizing an assembly of lenses [28], through nonlinear processing [27], as a direct output of microchip lasers [29], or utilizing metasurfaces [32–38].

As previously mentioned, the accelerating parabolic beam is also the exact solution of the two-dimensional paraxial wave equation. They are parabolic beams because of their inherent parabolic trajectory. Similar to Airy beams, the accelerating parabolic beam is also nondiffracting and shifts in the transverse direction upon propagation. Like other nondiffracting beams, they also carry infinite energy and are realized experimentally by using an appropriate apodization function. The finite energy parabolic beam retains its unusual properties over a finite propagation distance and was first generated experimentally by encoding both amplitude and phase of the Fourier spectrum using a single liquid crystal display [39].

The ballistic dynamics of Airy beams has been explored to engineer the trajectory, launch angle, nondiffracting propagation distance, controllable focal distance (i.e., working distance), and main lobe width. Airy beams' parabolic trajectory can be changed by applying an additional linear phase gradient at the input plane [40]. The pre-engineered trajectory can circumvent an obstacle and hence can be utilized in particle manipulation [41]. As discussed earlier, the experimental setup to generate an Airy beam involves cylindrical (1D Airy beam) or spherical (2D Airy beam) lenses. The launch angle of the Airy beam can be controlled by the transverse displacement of the imaging lens. The transverse displacement operation is equivalent to the shift-

ing property of the Fourier transform [42] and therefore, provides control over the initial launch angle of the Airy beam [40]. However, the setup gives some degree of control over the ballistic dynamics (trajectory and launch angle), the overall setup is bulky and an SLM is also limited in phase discretization due to its large pixel and pitch sizes (typically 10 times the wavelength of light). In recent years, metasurfaces have been utilized for amplitude and phase control in Airy beam generation. The ultrathin metasurfaces have improved the phase discretization and resulted in a compact all-in-one device integration. The conversion efficiency and generation bandwidth of Airy beams has also increased. Further control over their ballistics was achieved by using synthetic-phase metasurfaces [43]. Combining cubic phase of the Airy beam with the Fresnel lens phase on the metasurface has enabled focal length control, which can be utilized in adjusting the working distance between a sample and the metasurface. Furthermore, combining the cubic Airy beams' phase, Fresnel lens phase, and Dammann grating phase generated an array of Airy beams with the same characteristics.

Perhaps one of the most remarkable properties of a nondiffracting beam is its ability to reform its shape despite the severity of the perturbation. The shape-preservation after perturbation or this so-called self-healing property has been experimentally demonstrated by Broky et al. [44]. In this experiment, the main corner lobe of the 2D Airy beam was obstructed by an opaque object. The main lobe of the Airy beam was later reborn and persisted upon propagation up to a long distance. It was also found in this paper that the Airy beam can be regenerated, even if any part of the beam is severely perturbed. The self-healing process can be better understood by monitoring the transverse power flow of the beams, which provides an insight into the process of self-reconstruction of lobes. The robustness of the Airy beam has been further examined in scattering and turbulent media. The Airy beam has retained its shape under turbulent conditions, whereas other diffracting beams (e.g. Gaussian beam) suffer massive deformations. The evolution of the Airy beam has also been studied in different kinds of turbulent settings and be shape-preserving in all circumstances. Theoretically, the self-healing process can be understood in the framework of Babinet's

principle [45]. At the input plane, the total field can be considered as a superposition of a propagation invariant solution (e.g. the Airy beam) and the field generated from an obstruction. As the propagation distance increases, the field generated from the obstruction diffracts, and the diffraction-free beam is reconstructed.

Demonstrated applications of Airy beams include filamentation [46–50], imaging [51–55], particle manipulation [56–61], material processing [62–64]. Airy beam-based Superresolution fluorescence microscopy [53] and light-sheet microscopy [54, 55] have found commercial applications in optical imaging. In reference [53], isotropic three-dimensional localization was achieved using the self-bending point spread function (SB-PSF) derived from the Airy beam. The Airy-based SB-PSF has shown a substantial improvement in spatial resolution over Gaussian-based PSF. The axial measurement was performed by calibrating the experimental setup for the known bending trajectory of the Airy beam. The transverse resolution was achieved by suppressing the side lobe's of the Airy beam and hence improving the contrast of the main lobe. The side lobes suppression was achieved using a special type of phase profile shown in Figure 2 of the supplementary information of reference [53]. In another application of Airy beam in Light-Sheet microscopy [54] it has been found to provide high contrast, and resolution over an extended field-of-view compared to a Gaussian and Bessel beam. The Bessel and Airy beam have lower contrast at the focus, but they maintain their contrast upon large propagation due to their propagation invariant property. Among Bessel and Airy beams, it was observed [54] that those side lobes of Airy beams contribute positively to the image contrast. The self-accelerating and non-diffracting properties of the Airy beam have enabled microfluidic applications within the colloidal and biological sciences [57, 60]. The Airy beam is shown to invoke the precise transfer of colloidal particles from one chamber to an other without any complex beam steering [57]. In addition, the self-healing property of the Airy beam makes such 'optically mediated particle clearing' robust and efficient. Furthermore, circular Airy beam [65, 66] was used to create hot spots, which provides more control in particle manipulation. The intensity of the hot spot or the focal spot can be enhanced by

applying topological charges (vortex) to the circular Airy beam [67]. The bending of
the Airy beam is an important parameter in steering the particle trajectories, there-
fore it is desired to have a configuration in which a large curvature to Airy lobes can
be achieved. The non-paraxial case of Airy beams [19, 68] provides a strongly bend
trajectory as compared to paraxial Airy beam. The Airy beam trajectory is further en-
gineered by applying a linear phase in the input plane. The linear phase can induce
zero acceleration (straight line) or even reverse the acceleration, hence providing pre-
determined ballistic motions [40, 41]. A comprehensive overview of Airy beams and
their generation in different types of media can be found in reference [69].

One of the most remarkable applications of Airy beams has been found in the field
of plasmonics. Surface plasmon polaritons (SPP) are strongly localized collective os-
cillations of free electrons when coupled to photons at a metal-dielectric interface.
Plasmonics has substantially transformed the optics and photonics research on the
fundamental [70–73] and application level. The applications have resulted in many
multifunctional ultrathin optical devices such as biosensors [74–76], optical switch-
ing [77], photolithography [78–81], light beam shaping [82–86], optical imaging,
and spectroscopy [87–92]. Since Airy beams are 1D propagation invariant solution,
they are particularly suited for plasmonics. The so-called Airy plasmons were first
proposed in the seminal work of Salandrino and Christodoulides [93]. The problem
to describe Airy plasmons analytically is that is polarization-dependent and therefore,
is strictly vectorial [94]. The problem was solved using the scalar Helmholtz equa-
tion for the component of the electric field normal to the metal-dielectric boundary
[10]. The in-plane field components were calculated using the paraxial approxima-
tion. The Airy plasmons along with their localization on the metal-dielectric interface,
have been found to possess the free space Airy beams' properties i.e. Airy plasmons are
non-spreading, self-accelerating, and self-healing. The self-healing property keeps the
field profile relatively unaffected in case of metallic rough surfaces and fabrications
defects. This property makes the Airy plasmons relatively easy to realize experimen-
tally, however, matching the surface plasmon wave vector with the free space wave

vector is challenging. The challenge was overcome by three different groups [95–97] contemporarily by utilizing different excitation schemes. Airy plasmon generation can be viewed in two parts. The first is the generation of the amplitude and phase profile of the Airy beam and the second, is the coupling of free-space radiation to a metal-dielectric interface. The mismatch between the free-space wave vector and surface plasmon wave vector is overcome by employing a grating element. There are different ways in which the grating element can be utilized to generate the Airy plasmons. Zhang et al. [95] generated the Airy beams in free space using an SLM applied to a free space Gaussian beam and then converted the Airy beam on the back focal plane of the microscope objective to the Airy plasmons utilizing a linear grating inscribed at the metal-dielectric interface. Even though, the experimental setup is bulky, it provides real-time control over the trajectory of Airy plasmons by manipulating the free space Airy beams. Minovich et al. [96] have utilized a different coupling scheme, in which a specially designed grating is used to imprint the phase of the Airy profile while simultaneously coupling the free-space radiation to the metal-dielectric interface. In this scheme, the grating was excited with an extended light source at a wavelength of 784 nm and the generated Airy plasmons were imaged with a near-field scanning microscope. The generated Airy plasmons were in the non-paraxial regime as desired for high bending applications.

We have investigated a similar design by using a photoemission electron microscope (PEEM) in chapter III of this thesis and have also provided a formulation to quantify the Airy plasmon generation efficiency from such grating designs. The non-paraxial solution is not limited only to Airy plasmons but has also been shown for other types of accelerating surface plasmon beams (Mathieu beam and Weber beam) [98, 99]. Following the analogy of Airy beams, the interference of two Airy plasmons was demonstrated [100], which led to the generation and control of hot spots on the surface of the metal film. Similar to the free space Airy beam case, ballistic dynamics control of Airy plasmons was achieved by utilizing wedged metal-dielectric-metal structure [101] to mimic a linear index potential. A different method for generating

second harmonics of Airy plasmons has been suggested and implemented [102, 103].

In this classification (Table I.1), the temporal analog of the spatial finite Airy beam, the Airy pulse has been shown to possess the self-acceleration in time [104]. The Airy pulse can be considered as a superposition of monochromatic Airy beams with many wavenumbers over a certain spectral distribution. The spectral distribution depends on the Airy beam's scaling parameters, giving rise to different types of Airy pulses. In addition to spectral distribution, the spectral width also determines the Airy pulses propagation characteristics. The narrowband Airy pulses are found to preserve their transversal profile during propagation, while the broadband pulses change substantially [104]. Airy pulses have been widely studied in nonlinear media [105] and exhibit stable propagation even in media with strong nonlinearity [106]. An application of femtosecond Airy pulses in supercontinuum generation was experimentally demonstrated in reference [107].

In our previous discussion, we have seen that Airy waves are diffraction-free in space and dispersion-free in time. By employing both space and time characteristics, it is possible to generate a spatiotemporal wave packet, which is impervious to diffraction and dispersion. Indeed such localized field configuration is formed in three dimensions by combining a 2D Airy-Airy beam in space and an Airy pulse in time. Such Airy-Airy-Airy wavepacket [10, 108] propagates without diffraction and dispersion and gives rise to so-called stable light bullets. An other configuration of free space light bullets combines a Bessel beam in space and an Airy pulse in time [109]. These studies are based on separable spatiotemporal degrees of freedom. Recently, the spatiotemporal coupling effects have been exploited to efficiently synthesize diffraction-free and dispersion-free wave packets independent of the characteristics of the medium [110–113]. The spatiotemporal evolution has been understood well in free-space, but the plasmonics system still lacks a detailed investigation of the combined effects of space and time.

Therefore, the motivation of this work is in the direction of such spatiotemporal plasmonic systems. In chapter IV of the thesis, we discuss Airy plasmons evolution under
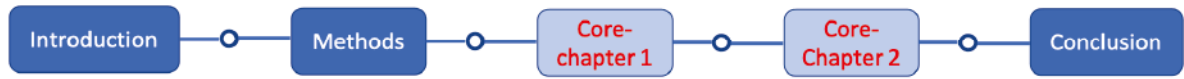
Figure 1.1. structure of thesis.

an ultrashort Gaussian pulse excitation. The Airy plasmon pulses manifest remarkable properties and set the course for future development for diffraction and dispersion-free pulsed beams. It should be noted that our research concerns only linear media. For shape-preserving pulsed beams in a nonlinear medium, one can explore the vast pool of knowledge base in the following references [114–118] .

The thesis is divided into five chapters. After this first introductory chapter, we lay the theoretical and mathematical foundations in chapter II. This chapter also provides an overview of the computational methods used in our research work. The chapters III and IV are the core chapters of the thesis, which discuss the original research work. In chapter III, we investigate the Airy plasmons with a multiphoton Photoemission electron microscope (n-PEEM) and also quantify the broadband Airy plasmon generation using modal overlap calculations. The work done in this chapter led to the possibility of generating ultrashort nondiffracting pulsed beams. Chapter IV numerically investigates the ultrashort Airy plasmon pulses in detail supplemented with a physical model to understand the spatiotemporal dynamics of nondiffracting pulsed beams. With these two substantial steps forward, we summarize our findings and discuss the viable future research paths.

The successful research work described in this thesis is a result of meticulous teamwork, which was not possible without the contributions from my colleagues and collaborators. The n-PEEM experiment was performed by M. Falkner, who currently works at the Institute of Applied Physics Jena. The fabrication of the sample in chapter 3 was performed by M. Steinert using a focussed ion beam etching method at the same institute. Goran Isić from the Institute of Physics, Belgrade, Serbia has provided many useful insights into design and simulations. Numerous discussions with Matthias Zilk and Thomas Kaiser, both had been at the Institute of Applied Physics Jena as well,

have helped in shaping chapter III of this thesis.

II. Theory and computational methods

The physics of electromagnetic waves and light-matter interaction can be well understood in the classical framework of electromagnetism using Maxwell's equations. Between 1961 and 1962, James clerk Maxwell established that light is a form of the electromagnetic wave and provided a set of mathematical equations [119, 120]. This mathematical model has opened new doors in our scientific understanding of nature. Maxwell's equations have wide applicability across the entire electromagnetic spectrum ranging from radio waves, visible light to gamma rays. This forms the foundation of classical optics and electrical engineering. Since the underlying concepts are the same, this has led to fruitful interdisciplinary research among physicist and electrical engineers [121–125]. Electrical circuits usually deal with low-frequency signals where only ohmic losses are present. In optics, radiative losses become significant due to the high frequency of electromagnetic radiation [126, 127]. This makes the system-level engineering highly dependent on the material's dispersive properties even though Maxwell's equations are scale-invariant.

In this chapter, the fundamentals of electromagnetic theory will be briefly discussed with an emphasis on material modeling, which will be important for our research. The optical radiation is described using Maxwell's equations under classical field theory. Therefore in most cases, we will use a classical approach to describe the radiation in a nano-optical system. An exception to this will be the study of photoemission of electrons from the metal surface in Photoemission Electron Microscopy (PEEM). The photoemission phenomenon can be understood only under a quantum mechanical picture and is briefly presented in chapter III. In addition, this chapter discusses the

various numerical methods that have been used in our research work to compute the electromagnetic response of such materials.

2.1. Maxwell's equations and wave propagation on a surface

2.1.1. Maxwell's equations and material modeling

Maxwell's equations in the time domain are given by

$$\nabla \cdot \mathbf{D}(\mathbf{r}, t) = -\rho_{\text{ext}}(\mathbf{r}, t), \tag{2.1a}$$

$$\nabla \cdot \mathbf{B}(\mathbf{r}, t) = 0, \tag{2.1b}$$

$$\nabla \times \mathbf{E}(\mathbf{r}, t) = -\frac{\partial \mathbf{B}(\mathbf{r}, t)}{\partial t}, \tag{2.1c}$$

$$\nabla \times \mathbf{H}(\mathbf{r}, t) = \mathbf{J}_{\text{ext}}(\mathbf{r}, t) + \frac{\partial \mathbf{D}(\mathbf{r}, t)}{\partial t}. \tag{2.1d}$$

These equations link the four macroscopic fields, the dielectric displacement $\mathbf{D}$, the electric field $\mathbf{E}$, the magnetic field $\mathbf{H}$, and the magnetic flux $\mathbf{B}$. The $\mathbf{D}$ and $\mathbf{H}$ incorporate the material effect such as polarization $\mathbf{P}$ and magnetization $\mathbf{M}$. The introduction of $\mathbf{D}$ and $\mathbf{H}$ are motivated by its usefulness in expressing Maxwell's equation in terms of external charge and current density. The auxiliary equations that define the displacement field $\mathbf{D}$ and magnetic field $\mathbf{H}$ are given by

$$\mathbf{D}(\mathbf{r}, t) = \varepsilon_0 \mathbf{E}(\mathbf{r}, t) + \mathbf{P}(\mathbf{r}, t), \tag{2.2}$$

$$\mathbf{H}(\mathbf{r}, t) = \frac{1}{\mu_0} \big[\mathbf{B}(\mathbf{r}, t) - \mathbf{M}(\mathbf{r}, t) \big], \tag{2.3}$$

where $\mathbf{P}$ and $\mathbf{M}$ are polarization and magnetization at the macroscopic scale. They can be defined in terms of internal charge and current as follows

$$\rho(\mathbf{r}, t) = \nabla \cdot \mathbf{P}(\mathbf{r}, t), \tag{2.4}$$

$$\mathbf{J}(\mathbf{r}, t) = \nabla \times \mathbf{M}(\mathbf{r}, t) + \frac{\partial \mathbf{P}(\mathbf{r}, t)}{\partial t}. \tag{2.5}$$

The division of total charge and the total current is arbitrary. They can be divided into a set of external and internal or into a set of a free and bound charges. In the case of noble metals, it is more suitable to use the external and internal sets and they can be explicitly written as follows

$$\rho_{tot}(\mathbf{r}, t) = \rho_{ext}(\mathbf{r}, t) + \rho(\mathbf{r}, t), \tag{2.6}$$

$$\mathbf{J}_{tot}(\mathbf{r}, t) = \mathbf{J}(\mathbf{r}, t) + \mathbf{J}(\mathbf{r}, t). \tag{2.7}$$

The polarization and magnetization are a material response to the electric and magnetic fields. The electric field induces electric dipole moment. These macroscopic electric dipole moment result in polarization which is defined as dipole moment per unit volume. The dependence of polarization can be linear in the external electric field resulting in a domain called linear optics. For high power laser pulses, the polarization depends on higher orders of the electric field and the resulting phenomena are studied under the subject area called nonlinear optics. The magnetization of the material is also a similar process. The application of the field $\mathbf{H}$ induces currents. The bound currents are the consequence of tiny current loops that are formed by moving electrons around the atomic orbit. The tiny current loops produce a magnetic moment. In the case of diamagnetic materials, the magnetic moment is along the magnetic field while in the case of paramagnetic material, opposite to the $\mathbf{H}$. The magnetization which is defined as magnetic moment per unit volume is the resultant of the induced magnetic moments of the material. The response to the applied field is linear in the case of paramagnetic and diamagnetic materials. However, in the case of a ferromagnetic material such as Iron, Nickel, and Cobalt, the magnetization depends on the history of the material and is nonlinear to the applied field $\mathbf{H}$. In optics, the materials usually have magnetic permeability $\mu = 1$ and the magnetization can be neglected, however, the μ can be changed even with artificial optical materials. Such artificial materials are called metamaterials. Metamaterials derive their properties by engineering the shape, geometry, size, orientation, and arrangement of nanostructures that provide the capabilities to manipulate electromagnetic waves [128–139].

The polarization and magnetization deal with only macroscopic bound charges and currents so hide the complexity behind the atomic scales microscopic charge currents and field distributions. However, the macroscopic description is still discrete enough to capture the spatial and time-dependent variation in the materials. The origin of the polarization and magnetization can be well understood by the deriving of macroscopic Maxwell's equation from microscopic Maxwell's equation [126]. The **P** and **M** can be expressed in terms of microscopic quantities, which results in higher order quadrupoles and octuples terms. The relevance of these terms becomes significant while studying high dielectric constants nanostructured media [140, 141].

The electric field **E** and magnetic flux density **B** are physical quantities in their own right, whereas the displacement field **D** and magnetic field **H** are the consequence of Maxwell's macroscopic description. So far, we have been using **D**, **E**, **H**, and **B** interchangeably in a different context. This sometimes confuses the readers. The fields that are more used in daily practices are those which can be measured via external means. For example in the pair of **D** and **E**, electric field **E** is used more often, simply because we can measure the potential difference using a device rather than measuring free charges that result in displacement field **D**. In the case of **H** and **B**, the quantity **H** is more common to use as it can be measured and controlled using external current, whereas **B** depends on the specific material used. The more popularity of one term over others is a purely practical consideration, from the theoretical point of view they are on equal footings.

Now, we derives the radiation fields (**E** and **H**) from Maxwell's equations in time domain using wave-equations. From Eq. (2.1)c and Eq. (2.1)d, it is straightforward to get

$$\nabla \times \nabla \times \mathbf{E}(\mathbf{r}, t) = -\mu_0 \nabla \times \frac{\partial \mathbf{H}(\mathbf{r}, t)}{\partial t}, \tag{2.8}$$

$$\nabla \times \nabla \times \mathbf{E}(\mathbf{r}, t) = -\mu_0 \frac{\partial \mathbf{J}(\mathbf{r}, t)}{\partial t} - \mu_0 \frac{\partial^2 \mathbf{D}(\mathbf{r}, t)}{\partial t^2}. \tag{2.9}$$

Using $\mathbf{J}(\mathbf{r}, t) = 0$ and the auxiliary equation (Eq. (2.2)), the above equation can be

simplified as

$$\nabla \times \nabla \times \mathbf{E}(\mathbf{r}, t) + \frac{1}{c^2}\frac{\partial^2 \mathbf{E}(\mathbf{r}, t)}{\partial t^2} = -\mu_0 \frac{\partial \mathbf{P}(\mathbf{r}, t)}{\partial t}. \tag{2.10}$$

This is the wave equation in $\mathbf{E}$. The right-hand side of this inhomogeneous equation is material-dependent terms. For Maxwell's equations to be self-consistent the electric field must also satisfy $\nabla[\varepsilon_0 \mathbf{E} + \mathbf{P}] = 0$. The electric field is obtained by solving the above wave equation. The magnetic fields $\mathbf{H}$ can be further calculated using Eq. (2.1)c.

Similarly, one can also solve the wave equation for the magnetic field $\mathbf{H}$ and obtain the electric field $\mathbf{E}$ using equation 2.1d. Sometimes this approach is more suitable for inhomogeneous media as will be discussed in detail in section 1.1.2. Furthermore, the time domain equations can be solved numerically using the finite difference time domain method and are discussed in section 2.1 of this chapter.

In linear media, we have the advantage of using one of the most versatile mathematical tools called Fourier transformation. The most generalized waveform of pulsed beams can be solved in linear media using frequency-domain Maxwell's equations. A pulsed beam is a continuous superposition of stationary plane waves with different wave vectors (propagation directions) and different frequencies. The solution of these stationary plane waves or so-called normal modes can be easily obtained with the help of the Fourier transformation. The definition of the Fourier transform used in this thesis is as follows

$$\mathbf{E}(\mathbf{r}, t) = \int_{-\infty}^{\infty} \mathbf{E}(\mathbf{r}, \omega) \exp(-i\omega t)\, d\omega, \tag{2.11a}$$

$$\mathbf{E}(\mathbf{r}, \omega) = \frac{1}{2\pi}\int_{-\infty}^{\infty} \mathbf{E}(\mathbf{r}, \omega)\exp(i\omega t)\, dt. \tag{2.11b}$$

The set of Maxwell's equations in the time domain Eq. (2.1) can now be solved more easily using the above Fourier decomposition of fields. With a little calculus, the

Maxwell's equations can now be written as

$$\nabla \cdot \mathbf{D}(\mathbf{r}, \omega) = -\rho_{\text{ext}}(\mathbf{r}, \omega), \tag{2.12a}$$

$$\nabla \cdot \mathbf{H}(\mathbf{r}, \omega) = 0, \tag{2.12b}$$

$$\nabla \times \mathbf{E}(\mathbf{r}, \omega) = i\omega\mu_0\mathbf{H}(\mathbf{r}, \omega), \tag{2.12c}$$

$$\nabla \times \mathbf{H}(\mathbf{r}, \omega) = \mathbf{J}(\mathbf{r}, \omega) - i\omega\mathbf{D}(\mathbf{r}, \omega). \tag{2.12d}$$

The relationships between $\mathbf{D}$ and $\mathbf{E}$ as well as between $\mathbf{H}$ and $\mathbf{B}$ are given by

$$\mathbf{D}(\mathbf{r}, \omega) = \varepsilon_0\varepsilon(\mathbf{r}, \omega)\mathbf{E}(\mathbf{r}, \omega), \tag{2.13}$$

$$\mathbf{B}(\mathbf{r}, \omega) = \mu_0\mu(\mathbf{r}, \omega)\mathbf{H}(\mathbf{r}, \omega), \tag{2.14}$$

where, permittivity $\varepsilon(\mathbf{r}, t)$ is related to susceptibility $\chi(\mathbf{r}, t)$ as follows: $\varepsilon(\mathbf{r}, \omega) = 1 + \chi(\mathbf{r}, \omega)$. The material properties vary across the electromagnetic spectrum and are important factors in device characterization. The explicit dependence of ε and μ on space and frequency will be discussed in the material model section.

The wave equation can be derived simply by using equation Eq. (2.12)c and Eq. (2.12)d as

$$\nabla \times \nabla \times \mathbf{E}(\mathbf{r}, \omega) - \frac{\omega^2}{c^2}\mathbf{E}(\mathbf{r}, \omega) = i\omega\mu_0\mathbf{J}(\mathbf{r}, \omega) + \mu_0\omega^2\mathbf{P}(\mathbf{r}, \omega). \tag{2.15}$$

Together with the above wave equation, the divergence condition should also be satisfied $\nabla[\varepsilon_0\mathbf{E}(\mathbf{r}, \omega) + \mathbf{P}(\mathbf{r}, \omega)] = 0$ to have self-consistent solutions of Maxwell's equations. The magnetic field can be calculated by using equation Eq. (2.12)c. After getting the $\mathbf{E}$ and $\mathbf{H}$ in the frequency domain, one can obtain the time domain solution for the nonstationary field simply by taking inverse Fourier transformation (2.11a).

In an inhomogeneous medium or piecewise homogeneous medium, the fields $\mathbf{E}, \mathbf{D}, \mathbf{B}$, and $\mathbf{H}$ are in general discontinuous at the boundary of the two mediums. The relationship is described using boundary conditions. The normal component of $\mathbf{E}$ and $\mathbf{H}$

on either side of the boundary are related through

$$(\varepsilon_2 \mathbf{E}_2 - \varepsilon_1 \mathbf{E}_1) \cdot \mathbf{n} = \sigma_{\text{ext}}, \tag{2.16a}$$

$$(\mathbf{H}_2 - \mathbf{H}_1) \cdot \mathbf{n} = 0. \tag{2.16b}$$

In words, the normal component of the magnetic field $\mathbf{H}$ is continuous across the boundary while the electric field component is discontinuous by the dielectric permittivity of the medium $\varepsilon_{1,2}$ and external surface charge density σ_{ext}.

Analogously, the tangential component of $\mathbf{E}$ and $\mathbf{H}$ on either side of the boundary are related through

$$\mathbf{n} \times (\mathbf{E}_2 - \mathbf{E}_1) = 0, \tag{2.17a}$$

$$\mathbf{n} \times (\mathbf{H}_2 - \mathbf{H}_1) = \mathbf{K}_{\text{ext}}, \tag{2.17b}$$

where the amount of discontinuity in the magnetic field is given by the magnitude of surface current $\mathbf{K}_{\text{ext}}$ and the direction is $\mathbf{K}_{\text{ext}} \times \mathbf{n}$. It can be noticed that the discontinuity in the magnetic field is a vectorial quantity. From the above boundary conditions, it can be inferred that the tangential component of the electric field is continuous across the boundary while the tangential component of $\mathbf{H}$ is discontinuous by the external surface current density.

In this thesis, we are generally concerned with the propagation of electromagnetic waves on the metal-dielectric interface. Some assumptions are made which are valid throughout this thesis:

- There is no external charge density ρ_{ext} and external current density $\mathbf{J}$.

- The materials used do not possess any magnetization effect $\mathbf{M}(\mathbf{r}, t) = 0$. Strictly speaking, the noble metals are diamagnetic at optical frequencies but its magnetization effects are so low that they can be ignored for any practical purposes.

- We will be considering the system with linear, inhomogeneous, isotropic, and dispersive media implying that χ is a function of position and frequency ($\chi(\mathbf{r}, \omega)$).

In Fourier domain such system is represented by the susceptibility $\chi(\mathbf{r}, \omega)$ as follows: $\mathbf{P}(\mathbf{r}, \omega) = \varepsilon_0 \chi(\mathbf{r}, \omega) \mathbf{E}(\mathbf{r}, \omega)$. In time domain, the system is described using a response function $R(\mathbf{r}, t')$ and the relation reads as:

$$\mathbf{P}(\mathbf{r}, t) = \varepsilon_0 \int_0^\infty R(\mathbf{r}, t') \mathbf{E}(\mathbf{r}, t - t') dt'$$

, where $R(\mathbf{r}, t')$ is response function.

Solving Maxwell's equations under these assumptions provides the radiation fields such as electric field $\mathbf{E}$ and magnetic field $\mathbf{H}$. Once we know the $\mathbf{E}$ and $\mathbf{H}$, other quantities of interest such as the Poynting vector and energy density can be calculated very easily. Maxwell's equations are not exact but a classical limit of more general quantum electrodynamics. In the scope of our work, the light-matter interaction can be well treated under the classical framework. It means electromagnetic radiation, as well as matter, can both be treated under the classical regime. The justification of using a classical picture for the light source is the abundance of photons under continuous-wave (CW) excitation or pulsed excitation. Any detector used in this context will be unable to see individual photons and rather will encounter a cumulative macroscopically observable response. The quantum treatment of electromagnetic fields is considered for example in the case of spontaneous emission of radiation by atoms, or by any other system that initially lacks photons and has only a small number of photons finally [142–145]. On the other hand, the matter is also considered under the classical picture. A macroscopic amount of matter at rest contains of the order of 10^{23} electrons and nuclei per cm^3, all in incessant motion because of thermal agitation, zero-point vibration, or orbital motion. The microscopic electromagnetic fields produced by these charges vary extremely rapid in space and time. The spatial variations occur over distances of the order of 10^{-10} m or less, and the temporal fluctuations occur with periods ranging from 10^{-13} s for nuclear vibrations to 10^{-17} s for electronic orbital motion. Macroscopic measuring devices generally average over intervals in space and time much larger than these. All the microscopic fluctuations are therefore averaged

out, giving relatively smooth macroscopic quantities, that appear in the macroscopic Maxwell's equations. Even metallic nanostructures down to sizes on the order of a few nanometers can be described without a need to resort to quantum mechanics since the high density of free carriers results in minute spacings of the electron energy levels compared to thermal excitations of energy $k_B T$ at room temperature.

In the scope of this thesis, the interaction of the metal with electromagnetic radiation is important. Metals occupy a special place in the study of solids due to their peculiar properties such as high conductivity of heat and electricity as well as high reflectivity at visible frequency. Physicists have been trying in the past century to construct models to account for these properties qualitatively and quantitatively. The behaviors of metals vary considerably over the spectral range of electromagnetic radiation. This means the devices engineered at radio frequencies can not be simply reproduced at an optical frequency just by simply applying the scale invariance property of Maxwell equations. One needs to know the explicit dependence of material properties on frequencies. The actual task of modeling the material is quantum mechanical, however, the phenomenological model given by Drude was able to describe most of the properties of the material accurately with a classical treatment. In the Drude model [146, 147] the electrons move freely and the model is based on the kinetic theory of an ideal gas. The electron density distribution follows the Maxwell-Boltzmann distribution. The model was able to describe frequency-dependent behaviors (dispersive properties), AC and DC conductivity of metals, and the Hall effect however it overestimated the heat capacity of metals. Later Sommerfeld made a quantum statistical treatment of the problem by assuming that free electron gas follows Fermi-Dirac distribution [148, 149]. With this Sommerfeld was able to remove many discrepancies of the classical model of Drude. We will now consider the Drude-Sommerfeld's theory in certain detail. The equation of motion for the free electron is given by

$$m_e \frac{\partial^2 \mathbf{r}}{\partial t^2} + m_e \Gamma \frac{\partial r}{\partial t} = e\mathbf{E}_0 e^{-i\omega t}, \tag{2.18}$$

where e and m_e are the charge and effective mass of free electrons. $\mathbf{r}(t)$ represents

the displacement of the electron from the equilibrium position under the influence of the applied electric field of amplitude $\mathbf{E}_0$ and frequency ω. The quantity $\Gamma = v_F/l$ is the overall damping of the system calculated using the Fermi velocity v_F and mean free path l between scattering events. At room temperature, the mean free path for a typical metal is $\approx 10\,nm$ (much larger than the interatomic spacing) and it can increase by orders of magnitude at low temperature. Notice that this equation is similar to a harmonic oscillator with no restoring force. Using the time harmonic ansatz $\mathbf{r}(t) = \mathbf{r}_0 e^{-i\omega t}$ and the relations $\mathbf{P} = \varepsilon_0 \chi(\omega)\mathbf{E}$, $\varepsilon(\omega) = 1 + \chi(\omega)$ with the given definition of polarization $\mathbf{P} = ne\mathbf{r}$, n being the number of electrons per unit volume, one can derive easily

$$\varepsilon(\omega) = 1 - \frac{\omega_p^2}{\omega^2 + i\Gamma\omega}, \tag{2.19}$$

here, $\omega_p = \sqrt{ne^2/m_e\epsilon_0}$ is the eigenfrequency of the system known as the plasma frequency. The above equation can be more conveniently separated into real and imaginary parts as follows

$$\varepsilon(\omega) = 1 - \frac{\omega_p^2}{\omega^2 + \Gamma^2} + i\frac{\Gamma\omega_p^2}{\omega(\omega^2 + \Gamma^2)}. \tag{2.20}$$

Metals like sodium involve no d-band and the above model describes the real and imaginary part of epsilon accurately. However, for a metal like silver and gold which involves d-bands, the above model fails to describe accurately the discrepancies in the imaginary part of epsilon at high frequencies. Partly this happens due to interband transitions taking place at these frequencies. The interband effect can be mimicked by adding a restoring force term in Eq. (2.18)

$$m_e \frac{\partial^2 \mathbf{r}}{\partial t^2} + m_e \gamma \frac{\partial r}{\partial t} + \alpha \mathbf{r}(t) = e\mathbf{E}_0 e^{-i\omega t}, \tag{2.21}$$

where m_e is an effective mass of the bound electrons, γ is the damping constant describing mainly radiative damping in the case of bound electrons, and α is the spring constant of the potential that keeps the electron in place. Applying similar steps as in

solving equation Eq. (2.18), the dielectric function can be written as

$$\varepsilon(\omega) = 1 + \frac{f}{(\omega_0^2 - \omega^2) - i\gamma\omega}, \qquad (2.22)$$

here, $\tilde{\omega}_p^2 = f = \tilde{n}e^2/m\epsilon_0$ is introduced in analogy with plasma frequency for but the bound electron density $\tilde{n}$ and $\omega_0 = \sqrt{\alpha/m}$.

The effect of the interband transition and the free electron model can be integrated in a single equation by combining equation 2.19 and 2.22

$$\varepsilon(\omega) = \varepsilon_\infty + \frac{f}{(\omega_0^2 - \omega^2) - i\gamma\omega} - \frac{\omega_p^2}{\omega^2 + i\Gamma\omega}. \qquad (2.23)$$

Any residual polarization due to vacuum or other resonance can be written as ε_∞.
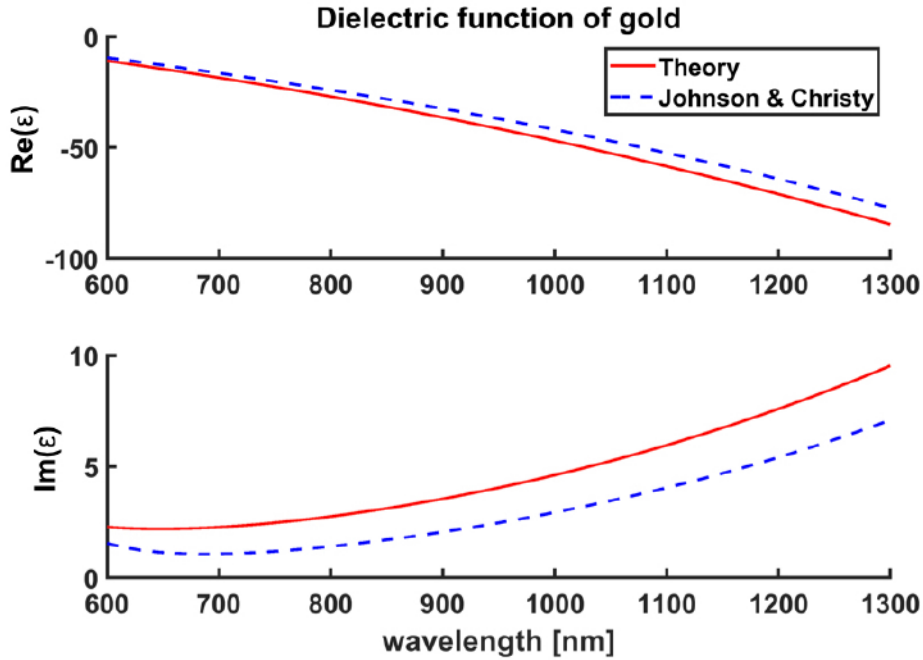

Figure 2.1. Dielectric function of gold: Experimental values and model. Upper panel: Real part, Lower panel: Imaginary part. Blue line shows the experimental data taken from [150]. Red line: model of dielectric function taking into account the free electron model and the contribution of a single interband transition.

This can be considered as a contribution to epsilon which does not change with respect to frequency. Moreover, there can be many interband transitions due to the availability

of d-bands in noble metals. This can be represented using oscillators with different transition frequencies. By considering these factors above equation becomes

$$\varepsilon(\omega) = \varepsilon_\infty + \sum_j \left\{ \frac{f_j}{(\omega_{0j}^2 - \omega^2) - i\gamma\omega} \right\} - \frac{\omega_p^2}{\omega^2 + i\Gamma\omega}. \tag{2.24}$$

Fig. 2.1 shows the material model fitted to the experimental values of the dielectric function of gold. In the model, the effect of the interband transition is considered by using a single oscillator along with the free electron contribution. The experimental data is in good agreement with the fitted model. The real part of the dielectric function shows a large negative value characteristic for reflection at visible and IR frequencies. The positive imaginary part is responsible for the dissipation of energy in metals.

In the above material model, the electron and ion interactions have been modeled using a classical harmonic oscillator. It has also been discussed that the mean free path at room temperature is an order of magnitude higher than interatomic spacing. This fact can not be explained based on classical models. The quantum mechanical treatment of the lattice and electrons must be taken into account. F. Bloch addressed this basic problem [151] and said, the mystery was 'how the electrons could sneak by all the ions in a metal'. He latter proved the important theorem that the solutions of the Schrödinger equation for a periodic potential of the lattice must be of a special form

$$\Psi_k(\mathbf{r}) = u_k(\mathbf{r}) \exp(i\mathbf{k} \cdot \mathbf{r}), \tag{2.25}$$

where $u_k(\mathbf{r})$ has the period of the crystal lattice with $u_k(\mathbf{r}) = u_k(\mathbf{r} + \mathbf{T})$. This mathematical expression is known as the Bloch theorem and can be stated as follows "The eigenfunctions of the wave equation for a periodic potential are the product of a plane wave $\exp(i\mathbf{k} \cdot \mathbf{r})$ times a function $u_k(\mathbf{r})$ with the periodicity of the crystal lattice." This has described the origin of bands in metal and had eventually helped to classify metals, semiconductors, and insulators. The formalism that was derived to treat the electron motion in the presence of a periodic potential can be applied to any periodic system

[152–155]. The analogy of the periodic ionic lattice has been applied to experimentally investigate the periodic layers of dielectric stacks and it has been found that such a system (known as 1D photonic crystals or Brag mirrors) possess photonic bandgap in one dimension [156, 157]. These bandgaps correspond to the 'forbidden' frequency ranges for which no propagating solutions of Maxwell's equations exist. This is exploited into making high reflectivity mirrors that are employed in laser cavities and the highly reflective coating in LED lights. A cavity can be formed using a sets of two Bragg mirrors known as Fabry-Perot resonator which can provide very high enhancement of the intensity inside the cavity. The Fabry-Perot resonator finds applications in spectrometers, lasers with an active medium for gain, and non-linear optics. The periodicity can be employed also in 2D and 3D with different geometric, and lattice configurations resulting in 2D and 3D photonic crystals. Different configurations can be used to engineer the band gaps resulting in various applications [158–162].

In optics, at large we are interested in guiding the wave in layer system [163–165]. For many applications, it is desired to have the propagation of light without diffraction and dispersion [118, 166, 167]. The waveguides are the backbone in modern-day communications as they carry the information at the speed of light over long distances [168]. They are used to trap the wave within a finite layer system. The light is confined in a direction perpendicular to the direction of propagation. The confinement can be achieved using so-called total internal reflection (TIR) in a slab waveguide [169–171], or by bandgap engineering to allow only a few modes such as hollow-core photonic crystal fibers [172], or utilizing the novel antiresonant waveguides [173]. Trapping of light in a single layer system can also be achieved through the coupled electromagnetic wave and collective electron oscillations in matter for example through surface phonon polaritons or surface plasmon polaritons [94, 174].

2.1.2. Plane wave surface plasmon polaritons

In this section, we describe the guided wave along a single interface system. Surface plasmon polaritons (SPP) are coupled electromagnetic oscillations of surface electron density at such metal-dielectric interfaces. Let us consider a planar interface between two media of dielectric function ε_1 and ε_2 and derive the conditions for the wave to propagate along the interface. We assume a TM polarized plane surface wave bound to a material interface in the xz plane at y = 0 and decaying exponentially at both sides of the interface along the y-direction. The material above the interface has the permittivity ε_1 and the material below the interface has the permittivity ε_2. The inhomogeneous and dispersive medium leads to all field components coupled. Solving the wave equation for the magnetic field **H** the surface plasmon is given by

$$\mathbf{H}(x,y,z) = \mathbf{H}_0 \exp(ik_x x + iqz) \begin{cases} \exp(\text{-}\alpha_1 y) & \text{for } y > 0 \\ \exp(+\alpha_2 y) & \text{for } y < 0 \end{cases} \tag{2.26}$$

As the SPP is a TM wave, the magnetic field is parallel to xz plane, i.e. $H_y = 0$, and continuous across the material interface. The magnetic field is divergence-free $(\nabla \cdot \mathbf{H} = 0)$, hence it has to be

$$k_x H_x + q H_z = 0. \tag{2.27}$$

This is fulfilled for

$$\mathbf{H}_0 = H_0 \left(\frac{q}{\beta} e_x - \frac{k_x}{\beta} e_z \right) \tag{2.28}$$

with

$$\beta^2 = k_x^2 + q^2. \tag{2.29}$$

The electric field follows from Maxwell's curl equation

$$\nabla \times \mathbf{H} = -i\omega\varepsilon_0\varepsilon\mathbf{E} \tag{2.30}$$

which yields

$$E(x, y, z) = \exp\left(ik_x x + iqz\right) \begin{cases} E_1 exp(-\alpha_1 y) & \text{for } y > 0 \\ E_2 exp(+\alpha_2 y) & \text{for } y < 0 \end{cases} \tag{2.31}$$

with

$$E_1 = -\frac{H_0}{\omega\varepsilon_0\varepsilon_1}\left(-i\alpha_1\frac{k_x}{\beta}e_x + \beta e_y - i\alpha_1\frac{q}{\beta}e_z\right) \tag{2.32}$$

and

$$E_2 = -\frac{H_0}{\omega\varepsilon_0\varepsilon_2}\left(i\alpha_2\frac{k_x}{\beta}e_x + \beta e_y + i\alpha_2\frac{q}{\beta}e_z\right). \tag{2.33}$$

The continuity of the tangential electric field components at the interface requires

$$\frac{\alpha_1}{\varepsilon_1} + \frac{\alpha_2}{\varepsilon_2} = 0 \tag{2.34}$$

For a bound surface wave both $\mathrm{Re}(\alpha_1)$ and $\mathrm{Re}(\alpha_2)$ have to be greater than 0. This implies $\mathrm{Re}(\varepsilon_1)\mathrm{Re}(\varepsilon_2) < 0$ and shows that a surface plasmon polariton can only exist at the interface between a metal ($\mathrm{Re}(\varepsilon_1) < 0$) and a dielectric ($\mathrm{Re}(\varepsilon_2) > 0$). Above the interface the decay constant is

$$\alpha_1^2 = \beta^2 - k_0^2\varepsilon_1 \tag{2.35}$$

and below is

$$\alpha_2^2 = \beta^2 - k_0^2\varepsilon_2. \tag{2.36}$$

Combining equations 2.34 and 2.36 yields the dispersion relation

$$\beta^2 = k_0^2\frac{\varepsilon_1\varepsilon_2}{\varepsilon_1 + \varepsilon_2}. \tag{2.37}$$

Since we are interested in a propagating wave along with the interface, so β^2 must be positive. This is only possible if the denominator is negative. Therefore the conditions

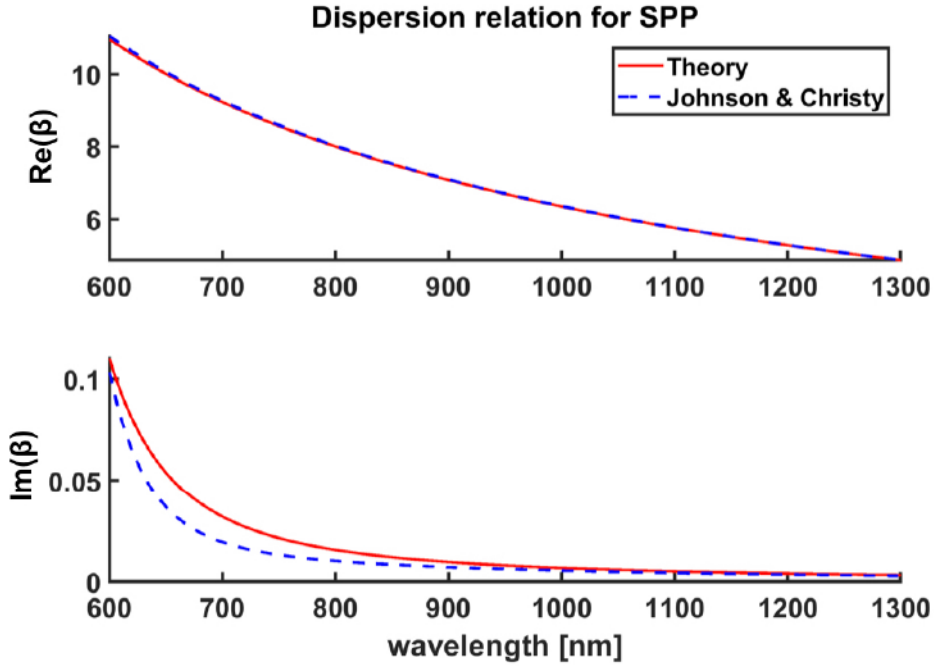**Dispersion relation for SPP**

Figure 2.2. Dispersion relation for air-gold system. Upper panel: Real part, Lower panel: Imaginary part. Blue line shows the data taken from [150]. Red line: model of dielectric function taking into account for free electron model and contribution of a single interband transition.

for a bound surface plasmon polariton on an interface are

$$\varepsilon_1(\omega) \cdot \varepsilon_2(\omega) < 0, \qquad (2.38\text{a})$$

$$\varepsilon_1(\omega) + \varepsilon_2(\omega) < 0. \qquad (2.38\text{b})$$

The above conditions can be easily fulfilled by an interface having a positive dielectric constant on one side and large negative dielectric constants on the other side. As it can be seen in Fig. 2.1 that gold has a large negative real part of the dielectric constant, therefore, posses to be the natural ally for the generation of surface plasmons polaritons. Fig. 2.2 depicts that the real part of the propagation constant has a positive value, therefore the air-gold interface is suitable for SPP propagation. Controlling the diffraction and dispersion of such propagating surface plasmons are the core of this thesis work and will be discussed qualitatively and quantitatively in chapters III and

IV.

2.2. Numerical methods for modelling computational electromagnetics

Computational electromagnetics (CEM) are procedures to model and simulate the behavior of electromagnetic fields in devices or the structures in an optical system. Most often, this implies using numerical techniques to solve Maxwell's equation instead of obtaining the analytical solution. Numerical techniques offer the ability to solve virtually any electromagnetic problem of interest. These methods are useful because very often, exact analytical solutions or even good approximate solutions are not available. So basically CEM provides an opportunity to perform numerical experiments akin to the laboratory environment. The numerical experiment can be performed by changing various design parameters with more flexibility and feasibility over fabricating each design and carrying out laboratory experiments on them. These advantages of numerical experiments further help to explore prospective applications for future generations of technologies. Computational photonics is also utilized in a reverse scientific approach in which the experiment is performed first and then numerical simulations are used to interpret and understand the experimental results.

The computational methods can be classified based on size scale or approximations. Classification by size scale can be divided into high-frequency methods ($\lambda \ll a$) and low-frequency methods ($\lambda \sim a$). The high-frequency methods are suitable for structural dimensions (a) much larger than the wavelength. In this case, the computation becomes rather easy as one can often consider the fields as scaler quantities. This results in a realm of geometric and physical optics [175–177]. In contrast, the device that we are modeling is of the order of wavelength so we will consider the low-frequency method. At this scale the polarization and vector nature of the electromagnetic fields become important and one has to consider the full-wave nature of electromagnetism

[178–180].

Computational problems can be further classified based on the approximations used in the numerical treatment of the electrodynamics problem. Three basic categories can be identified: rigorous methods, full wave methods, and scalar methods. A method is rigorous if there exists a resolution parameter that when taken to infinity, finds an exact solution to Maxwell equations. Some examples of this method are the finite-difference time domain (FDTD), finite-difference frequency domain, finite element method, rigorous coupled-wave analysis, and method of lines. A full-wave method although it accounts for the vector nature of the electromagnetic field, needs not be necessarily rigorous. Examples are the method of moments, boundary element method, and beam propagation method (BPM). A scaler method is used when the vector nature of the field is not required to understand the optical system and BPM or transfer matrix methods can be used for such purposes.

Before we dive into an overview of different methods, it is important to consider some general practices that are applied in CEM. Virtually all numerical methods have a 'resolution parameter' (spatial or temporal) that when taken to infinity, it solves Maxwell's equation in principle exactly. In practice this can not be done because of limiting computing power and prohibitively long simulation time. So one goes with a finite resolution value. To make sure the chosen value calculates a sufficiently accurate result, one needs to perform a so-called convergence test. Convergence is the tendency of calculated parameters to asymptotically approaching a fixed value as their resolution is increased. However one has to be careful in the convergence test for any possibilities of unstable solutions [181–185].

Now let us consider an overview of some computational methods with their real-world applications. The simplest method of all is the transfer matrix method (TMM) [186–188]. The method assumes an infinite extent in the transverse directions. It is suitable for layered structures in the longitudinal direction and of infinite extent in the transverse direction. Examples are Bragg mirrors used in lasers or thin-film optical filters used in mobile camera lenses. In both examples, the transverse dimension is very

large as compared to the wavelength, and the material property changes only along the longitudinal direction. The transfer matrices method derives the relationship of the fields present at the interface between the layers. Transmission through all the layers is described by multiplying all the individual transfer matrices. This method provides the transmission and reflection coefficients which are experimentally accessible quantities and hence can be verified easily. In addition to TMM, there exists a more mature and proven approach known as the scattering matrix method. The transfer matrix method using scattering matrices is rigorous, accurate, unconditionally stable, robust, efficient, and simple to implement. The thickness of the layer can be anything and the method is also able to exploit the longitudinal periodicity. It can calculate the reflection and transmission parameters for oblique incidence as well as for arbitrary polarization of incident fields. The method also incorporates material dispersion and anisotropic materials very efficiently. With all the advantages stated, this method also suffers from some drawbacks. It can model only a limited number of geometries and can handle only linear, homogeneous, and infinite slabs in the transverse direction.

2.2.1. Finite difference time domain method

One of the most popular numerical methods used in computational electrodynamics is the finite difference time domain (FDTD) method [189–194]. Each tool has its strengths and weaknesses. No single computational method can be applied to all types of photonic devices. As far as the FDTD method is concerned, it is a highly versatile, accurate, robust, and mature method. The sources of error are well understood and can be bounded to permit accurate models for a large variety of complex electromagnetic problems. FDTD is a fully explicit solutions of Maxwell's equations and does not rely on demanding linear algebra. This approach provides no intrinsic upper bound to solve many electromagnetic fields unknown. Being a time-domain method, FDTD treats impulsive behavior naturally. Therefore, a single FDTD simulation can provide either ultrawideband temporal waveforms or the sinusoidal steady-state response at

any frequency within the excitation spectrum. Furthermore, nonlinear behaviors are inherently time-domain numerical problems, so FDTD can directly calculate the nonlinear response of the electromagnetic system. The FDTD method has a straight forward implementation, although the requirements on the computational resources are demanding in 3D problems due to discretization of space over volume. The discretization of space is performed using the so-called YEE grid [189]. The Yee grid can ensure inherently divergence-free solutions.

Space and time derivatives of the time-dependent Maxwell's equations are first discretized using the central difference approximation and then the electromagnetic field is evolved in a leapfrog manner. The computational procedure works as follows:

- The magnetic field vector components are calculated at $(n + 1/2)\Delta t$, using the spatial differences of E field that are known for time step $n\Delta t$.

- Then using the spatial differences of the H field that are now known for the time step $(n + 1/2)\Delta t$, the E field at the time step $(n + 1)\Delta t$ is calculated.

The above procedure is repeated over and over again to compute magnetic and electric fields at subsequent time steps until the desired transient or steady-state electromagnetic field behavior is fully evolved. The proposed scheme for marching in time mandates an upper bound on the time-step to ensure numerical stability [195]. To ensure stability, the Courant-Friedrichs-Lewy condition has to be fulfilled [183], which states that temporal and spatial discretization can not be chosen independently. The relation between the size of the time step to the spatial discretization in 1D is given by: $c\Delta t = S\Delta x$. Usually S is chosen to be 0.5 and in general it should have the value $S < n_{min}/\sqrt{\# dimensions}$.

In practice, all devices are simulated in a finite sized computational domain. To treat the finite computational domain size the simulation should be truncated in space. There are three basic types of boundary conditions: perfectly conducting material boundary conditions, Floquet-Bloch periodic boundaries, and perfectly matched layer boundaries. In the perfectly conducting material boundary or so-called metallic walls,

the fields are forced to be zero at the boundary as if the computational domain was surrounded by a perfect metal (zero absorption, zero skin depth). The Floquet-Bloch periodic condition is especially suitable for infinitely periodic structures such as modes in waveguides, the band structure of photonic crystals, and transmission-reflection problems in gratings. The implementation of such boundaries follows from Bloch's theorem on periodic structures (equation 2.25). The most efficient boundary condition known so far is a perfectly matched layer (PML). PML is, strictly speaking, not a boundary condition, rather, it is a special absorbing material placed adjacent to the boundaries. It helps to simulate open boundaries by absorbing all incident waves on it with no reflection. This is performed by matching the impedance of the medium by its surrounding [196]. In addition to these different types of numerical boundary conditions, FDTD also supports all types of materials. There exists a variety of approaches to include dispersive, metallic, and nonlinear materials, but usually, all of them require to simulate quantities such as current density (**J**), polarization (**P**) and displacement (**D**) in addition to the electric field (**E**), and magnetic field (**H**). In our research work, metals and their dispersion characteristics will be of main concern. This can be implemented in the FDTD algorithm directly using the Lorentz model in the time domain (Eq. (2.21)).

FDTD can be used in some basic ways to analyze electromagnetic problems. Perhaps it is the most efficient method to compute the broadband response of a finite structure. This is achieved by Fourier transforming the device response to a short pulse. This brute force approach can be applied to many tasks such as transmittance/reflectance spectra of resonant cavities, to compute the eigenmodes of waveguides or the near fields at metallic structures. To extract the broadband or temporal response of a structure with FDTD, the basic idea is very simple. First, the boundary conditions with Bloch-periodic and/or absorbing boundaries are set up depending on whether it is a periodic or open system. Then the system is excited using a short pulse as an input source. The broadband frequency response is calculated using the Fourier transform of recorded fields over time. The recorded field can also be used to generate an an-

imation of temporally evolving fields. This will be the main computational tool in the thesis for the temporal and spatial analysis of the plasmonic structures. However, this method suffers from one technical difficulty in efficient FDTD simulation of ultra-short pulses having oblique incidence. The oblique incidence of short pulse imposes numerical problems in the Fourier analysis as it requires periodicity of the fields over the simulation area. A nice workaround to this problem is possible by calculating the Green's function [197, 198] of a system for a plane wave CW source over a range of frequencies. This Green's function is then convolved with the oblique incidence pulse. The resultant convolved pulse is the time-dependent response to the dispersive system under the oblique incidence of a broadband pulse. In this work, an open source electromagnetic solver 'MEEP' and commercial software 'Lumerical FDTD' solutions are used to calculated the electromagnetic response of nano-structures. In this thesis, simulation results are presented only from Lumerical. Meep simulation results are found similar to Lumerical results, therefore, validates the Lumerical simulations. The simulations results will be discussed in detail in chapter III.

2.2.2. Beam propagation method

Beam propagation method (BPM) has been one of the most popular approaches used in the modeling and simulation of electromagnetic wave propagation in guided wave optoelectronics and fiber-optic devices [199–202]. A simple numerical model can be used to simulate scalar wave propagation along the waveguide axis in weakly guiding structures [203–206]. The BPM method inherently calculates the forward propagating electromagnetic waves only. The basic assumption of the BPM methods is that the index variation in the propagation direction is small. This assumption effectively eliminates the reflected wave from the formulation. Despite this limitation, there are several reasons for the popularity of BPM, perhaps the most significant being that concepts have straight forward interpretation and allow rapid implementation of the basic technique. In addition to its relative simplicity, BPM is a very efficient method and can

simulate electromagnetic behavior in complex geometries. Another characteristic of BPM is that the approach automatically includes the effects of both guided and radiating fields as well as mode coupling and conversion. Last, the BPM techniques are very flexible and extensible, allowing the inclusion of most of the effects of interest (e.g. polarization, nonlinearities) by extension of basic methods that fit within the overall framework [186].

The basic BPM algorithm solves the scalar wave equation under paraxial approximation

$$\frac{\partial u}{\partial z} = \frac{i}{2\beta}\left(\frac{\partial^2 u}{\partial x^2} + \frac{\partial^2 u}{\partial y^2} + (k^2 - \beta^2)u\right). \tag{2.39}$$

where $k = k_0 n(x,y)$, $\beta = k_0 n_0$ and u denotes the scalar electric or magnetic field. In free space, $k_0 = 2\pi/\lambda$. β is the propagation wavenumber, $n(x,y)$ is the refractive index distribution of the waveguide structure, and n_0 the reference refractive index to be appropriately chosen. In this equation, we have assumed that the propagation is restricted to a narrow range of angles so that the second-order derivative of the field u with z is negligible. The above equation determines the evaluation of fields in space for $z > 0$ for a given field $u(x,y,z=0)$. The above approach has mainly two advantages. First, the elimination of second-order derivative in z, reducing the problem from a second-order boundary value problem requiring iteration or eigenvalue analysis, to a first-order initial value problem that can be solved by a simple integration of the above equation along the propagation direction. Second, the factoring of the rapid phase variation allows the slowly varying field to be represented numerically on a longitudinal grid (i.e., along z) with much coarser grid points. In the following section, the numerical solution of the basic BPM equation will be considered. In every numerical approach, one needs to satisfy numerical boundary conditions. Since BPM simulates a domain, which has a finite extension in the transverse direction there should be no reflected wave from the boundaries. In practice, this can be implemented using transparent boundary conditions [196, 207–209].

Numerical solution using fast Fourier transform (FFT-BPM)

Simplification of the basic BPM to 2D can be obtained by assuming no dependency on y-direction. In this case Eq. (2.39) becomes

$$\frac{\partial u}{\partial z} = \frac{i}{2\beta}\left(\frac{\partial^2 u}{\partial x^2} + (k^2 - \beta^2)u\right). \tag{2.40}$$

In the BPM, one propagates the input field $u(x, z_0)$ over a small distance Δz to obtain the field at $u(x, z_0 + \Delta z)$ [206, 210]. Separating the amplitude and phase term $u(x, z_0 + \Delta z)$ can be written as

$$u(x, z_0 + \Delta z) = \psi(x, z_0 + \Delta z)\exp(i\Gamma), \tag{2.41}$$

where ψ satisfies equation 2.40. The phase correction also called propagator is given by

$$\Gamma = \frac{k^2 - \beta^2}{2\beta}\Delta z. \tag{2.42}$$

$\psi(z_0 + \Delta z)$ can be calculated using FFT method. If $\psi_n(z)$ denotes the discrete Fourier transform (DFT) of $\psi(x, z)$, we have

$$\psi(x_i, z) = \frac{1}{N}\sum_{n=-N/2}^{N/2}\psi_n(z)\exp(-ik_n x_i), \tag{2.43}$$

where $k_n = 2n\pi/(N\Delta x)$ is the discrete k wavevector.

$$\psi_n(z_0 + \Delta z) = \psi_n(z_0)\exp\left(-i\frac{k_n^2}{2\beta}\Delta z\right), \tag{2.44}$$

where the computational domain in x-direction has been discretised into N equal subdivisions.

The basic steps in applying FFT-BPM involves applying equation Eq. (2.41) and Eq. (2.42) where $\psi(x, z_0 + \Delta z)$ is obtained by

1. performing a FFT on $\psi(x, z_0) = u(x, z_0)$ to obtain $\psi_n(z_0)$,

2. computing the $\psi_n(z_0 + \Delta z)$ from Eq. (2.44),

3. performing an inverse FFT on $\psi_n(z_0 + \Delta z)$ to obtain $\psi(z_0 + \Delta z)$.

This basic step is applied repeatedly to obtain the field at any finite propagation distance z. The accuracy of the method, of course, depends on the smallness of the step size Δz and the grid size Δx as well as on the size of the computation domain and the choice of β. This method will be used in section Chapter 3 in our analysis of surface plasmons propagation.

Numerical solution using finite difference beam propagation method (FD-BPM)

In FD-BPM the field is represented at a discrete plane along the propagation direction (z-direction) and is calculated using the YEE grid in the transverse direction [204]. Given the discretized field on a transverse plane, the goal is to derive numerical equations that determine the field at the next plane using a propagator

$$E_{i+1} = P_{i \to i+1} E_i, \tag{2.45}$$

and the propagator P is calculated using Maxwell's equations discritized on the YEE grid

$$P = \left(\mathbf{I} - \frac{i\Delta z}{4n_{eff}} A_{i+1} \right)^{-1} \left(\mathbf{I} - \frac{i\Delta z}{4n_{eff}} A_i \right), \tag{2.46}$$

where $\mathbf{A}$ is a matrix given by

$$\mathbf{A} = \mu_{xx}^i D_x^H (\mu_{zz}^i)^{-1} D_x^E + \mu_{xx}^i \varepsilon_{yy}^i - n_{eff}^2 \mathbf{I}, \tag{2.47}$$

with the derivative operators D_x in x direction.

In the BPM, we have assumed the scaler and paraxial approximation of Maxwell's equations. The BPM can also be adapted for vectorial waves to incorporate the polarization effects [203, 207, 211–213] as well as for wide-angle propagation [209, 214, 215] utilized in high index contrast waveguides. A discussion of these methods

is outside the scope of this thesis.

In this chapter, the theoretical framework has been developed that will be used in the rest of the thesis. The analogy between the Schrödinger equation and paraxial wave equation is found to be very fruitful in developing new ideas in the field of photonics and plasmonics. In the next chapter, such manifestations will be shown for a non-diffracting beam propagating in a dispersive system.

III. Broadband propagation characteristics of Airy plasmons

Curved and accelerating beams have been the subject of intense investigation in the last 10 years [1, 10, 17, 69, 93]. The concept of self-accelerating wave packets first appeared in the context of quantum mechanics in the seminal work of Berry and Balazs [1]. Such self accelerating, shape preserving wave packet is the solution to a potential free Schrödinger equation in the form of an Airy wave. The work has remained dormant for decades probably due to limited practical applications. Until the isomorphism between Schrödinger equation and paraxial wave equation was exploited in the work of Siviloglou and Christodoulides in 2007 [10] and was further experimentally observed [24]. The research has opened new pathways to utilize the properties of Airy waves in the field of optics with attractive applications such as trapping, guiding, sorting of micro-objects, and signal processing [57, 60, 216, 217]. In addition to the non-diffracting and self-accelerating properties, Airy beams also possess a self-healing character which makes them robust against strong perturbation or turbulent media. Airy beams are the only non-trivial non-diffracting solution of the paraxial wave equation in one dimension. These remarkable properties make Airy beams different compared to other non-diffracting solutions such as Bessel, Mathieu, and Weber beams [3–8, 98]. The one-dimensional nature of Airy beams renders them particularly interesting for plasmonics system.

A Metal-dielectric interface serves as the best companion of Airy beams in a planar system. These interfaces are known to support surface plasmon polaritons (SPPs).

40

Combining the properties of Airy beams and surface plasmon polaritons gives non-spreading plasmonic beams in the planar system known as Airy SPPs. Airy plasmons can be defined as propagating surface plasmons having the properties of Airy beams.

The chapter is organized as follows: In section 3.1, the theory of paraxial and non-paraxial Airy plasmons is presented. Section 3.2 provides the design for the generation of Airy plasmons along with numerical and experimental results. We further obtain the generation efficiency and bandwidth of the Airy grating in section 3.3. Section 3.4 summarizes the results and related publication.

3.1. Theory of Airy surface plasmons

Diffraction-free beams preserve their shape along the propagation direction. The ideal Airy beams carry infinite energy and retain their nondiffracting properties for infinite propagation distance. In practice, only finite energy Airy beams are realizable and are achieved by exponentially apodizing the Airy wave profile. The metal interface for the generation of Airy plasmons imposes further restrictions. The losses in the metal limit the propagation length over which the Airy plasmons remain diffraction-free. In this section, we provide first the solution of the paraxial wave equation and then we derive the exact solution of Maxwell's equations to obtain a nonparaxial solution. The analytics incorporate the finite energy Airy plasmons with losses.

3.1.1. Airy surface plasmons under paraxial approximation

The analytical solution for paraxial Airy plasmons was first derived and analyzed by Salandrino et al. [93]. In a plasmonic system, the exponential decay of the transverse field distribution is fixed. Therefore, the plasmon propagation properties are exclusively dictated by its one-dimensional (1D) angular spectrum. The angular spectrum is obtained by solving the paraxial wave equation. Let us assume a planer interface at $y = 0$, the material above the interface has the permittivity ε_1 and material below

has the permittivity ε_2. In this case, the normal component of the electric field follows scaler the Helmholtz equation

$$\nabla^2 E_y + k_0^2 \varepsilon_d E_y = 0, \tag{3.1}$$

where k_0 is the free space wavenumber. The solution to the above equation should have functional dependence to include the exponential decay of plasmon fields away from the surface. This can be expressed as follows

$$E_y(x,y,z) = A(x,z)\exp(i\beta z) \begin{cases} \exp(-\alpha_1 y) & \text{for } y > 0 \\ \exp(+\alpha_2 y) & \text{for } y < 0 \end{cases}, \tag{3.2}$$

where $\beta = k_0\sqrt{\varepsilon_1 \varepsilon_2/(\varepsilon_1 + \varepsilon_2)}$ is the wavenumber for surface plasmon propagation. The decay amplitudes $\alpha_{1/2}$ are related via the dispersion relation and are given by $\alpha_{1/2}^2 = \beta^2 - k_0^2 \varepsilon_{1/2}$ above/below the interface. Here, we have also assumed that SPP propagation is along the z-direction. For a transverse profile that varies slowly along the propagation direction z, the problem can be further simplified into a paraxial wave equation

$$\frac{\partial^2 A}{\partial x^2} + 2ik_z \frac{\partial A}{\partial z} = 0. \tag{3.3}$$

This equation has a solution for the complex amplitude A(x, z) of the normal component of the electric field in the form of finite energy Airy profile

$$
\begin{aligned}
A(x,z) = \text{Ai}&\left[\frac{x}{x_0} - \left(\frac{z}{2k_z x_0^2}\right)^2 + i\frac{az}{k_z x_0^2}\right] \\
&\times \exp\left[i\left(\frac{x + a^2 x_0}{2x_0}\frac{z}{k_z k_0^2} - \frac{1}{12}\left(\frac{z}{k_z x_0^2}\right)^3\right)\right] \\
&\times \exp\left[a\frac{x}{x_0} - \frac{a}{2}\left(\frac{z}{k_z x_0^2}\right)^2\right],
\end{aligned}
\tag{3.4}
$$

where a is the exponential apodization parameter, $2x_0$ is the width of the main lobe, and 'Ai' denotes the Airy function. The free parameters a and x_0 are used to optimize the spectrum, propagation length, and acceleration of Airy plasmons. From the above

Eq. (3.4), it can be deduced that the Airy plasmon propagates on a parabolic trajectory $x = [1/(4k_z^2 x_0^3)]z^2$. The angular spectrum of this solution is given by

$$\tilde{A}_0(k_x, z) = x_0 \exp(\frac{a^3}{3}) \exp(-iax_0 k_x) \exp(-ax_0^2 k_x^2) \exp(\frac{-ix_0^3 k_x^3}{3}) \exp(-i\frac{k_x^2 z}{2k_z^2}).$$

$$(3.5)$$

In the above equation, the Gaussian spectrum arises due to exponential apodization and the cubic phase term is the signature of the Airy function itself. The gaussian spectrum is further used to define the condition of paraxiality

$$\sqrt{ln2/(ax_0^2)} \ll \beta \tag{3.6}$$

This relationship between free parameter x_0 and λ is optimized to provide experimentally observable Airy plasmons. One can define the characteristic propagation distance Z_c for which the beam is displaced approximately one full width $2x_0$ (taking the quantity $2x_0$ as the measure of the width of the main lobe). Equation 3.4 can be used to estimate the characteristic propagation length $Z_c = 2\sqrt{2}k_z x_0^2$. This characteristic parameter was used to estimate an upper limit of propagation losses that can be tolerated in an experimental setup on an air-silver interface in reference [93]. However, in the case of paraxial limit, the bending of the beam is low which may be unobservable for a small propagation length in a highly lossy metallic surface.

3.1.2. Nonparaxial solution

In chapter II, the foundation of SPP is laid by providing a new perspective on propagation dynamics. Along the same line, we take the first step towards deriving the analytical expression of the electric and magnetic fields. In this section we will perform the theoretical analysis of nonparaxial Airy plasmons. The nonparaxial Airy plasmons are exact solutions of Maxwell's equations and provide highly bending trajectories along the propagation direction.

Let us assume a TM polarized plane surface wave bound to the material interface

in the xz-plane at y= 0 and decaying exponentially along the the y-direction. The material above the interface has the permittivity ε_1 and the material below the interface has the permittivity ε_2. The solution of Maxwell's equations for the TM-polarized surface plasmons in real space is given by

$$\mathbf{H}(x,y,z;x_0,a) = \hat{\mathbf{H}}(x,z;x_0,a) \begin{cases} \exp(-\alpha_1 y) & \text{for } y > 0 \\ \exp(+\alpha_2 y) & \text{for } y < 0 \end{cases} \tag{3.7}$$

with

$$\hat{\mathbf{H}}(x,z;x_0,a) = \int_{-\infty}^{\infty} \tilde{A}_0(k_x;x_0,a)\left(\frac{q(k_x)}{\beta}\mathbf{e}_x - \frac{k_x}{\beta}\mathbf{e}_z\right)\exp\left(ik_x x + iq(k_x)z\right)dk_x \tag{3.8}$$

where $\tilde{A}_0(k_x)$ is magnetic field amplitude and the in-plane wavenumber is given by $\beta^2 = k_x^2 + q^2$. The parameters β and α are related through the dispersion relation, above the interface $\alpha_1^2 = \beta^2 - k_0^2\varepsilon_1$ and below the interface $\alpha_2^2 = \beta^2 - k_0^2\varepsilon_2$.

The magnetic field amplitude to generate the initial Airy beam profile $\text{Ai}(x/x_0)$ $\exp(ax/x_0)$ is given by [68]

$$\tilde{A}_0(k_x) = \frac{1}{2\pi}\exp\left(-ak_x^2 x_0^2 + \frac{i}{3}[k_x^3 x_0^3 - 3a^2 k_x x_0 - ia^3]\right) \tag{3.9}$$

The parameter a is a measure of the strength of the exponential apodization of the field profile and x_0 is a scaling parameter which characterizes the width of the main lobe of the Airy beam.

The electric field components are calculated by applying Maxwell's curl equation and are given by the following equations

$$E_x(x,y,z;x_0,a) = -\frac{1}{\omega\varepsilon_0}H_z(x,y,z;x_0,a)\begin{cases} \frac{i\alpha_1}{\varepsilon_1}\exp(-\alpha_1 y) & \text{for } y > 0 \\ -\frac{i\alpha_2}{\varepsilon_2}\exp(+\alpha_2 y) & \text{for } y < 0 \end{cases} \tag{3.10}$$

$$E_z(x,y,z;x_0,a) = -\frac{1}{\omega\varepsilon_0}H_x(x,y,z;x_0,a)\begin{cases} \frac{i\alpha_1}{\varepsilon_1}\exp(-\alpha_1 y) & \text{for } y > 0 \\ -\frac{i\alpha_2}{\varepsilon_2}\exp(+\alpha_2 y) & \text{for } y < 0 \end{cases} \tag{3.11}$$

and

$$E_y(x, y, z; x_0, a) = \hat{E}_y(x, z; x_0, a) \begin{cases} \frac{1}{\varepsilon_1} \exp(\text{-}\alpha_1 y) & \text{for } y > 0 \\ \frac{1}{\varepsilon_1} \exp(+\alpha_2 y) & \text{for } y < 0 \end{cases} \tag{3.12}$$

with

$$\hat{E}_y(x, z; x_0, a) = -\frac{\beta}{\omega \varepsilon_0} \int_{-\infty}^{\infty} \tilde{A}_0(k_x; x_0, a) \left(\frac{q(k_x)}{\beta} e_x - \frac{k_x}{\beta} e_z \right) \exp\left(i k_x x + i q(k_x) z \right) dk_x \tag{3.13}$$

The above solution is exact and the paraxial approximation can be obtained when the spatial spectrum of the propagating wave is wide [10, 96].

3.2. Generation of Airy surface plasmons

A variety of techniques have been proposed and demonstrated for the generation of Airy surface plasmons (Airy SPPs). Airy SPPs are essentially surface plasmons with the properties of an Airy beam. The generation of an Airy beam in free space is fairly straightforward. One has to utilize the fact that in k-space the exponentially apodized Airy function has a Gaussian shape spectrum with a cubic phase modulation $\phi_0 = exp(-ak_0)exp(ik^3/3)$. Therefore, an Airy beam is generated at the back focal plane when a phase mask with the cubic phase distribution is illuminated by a Gaussian laser beam and Fourier transformed by an optical lens. However, in the case of Airy SPPs, there are additional constraints due to the k-vector mismatch between free space and surface plasmons. This challenge was overcome by three different groups contemporarily using different approaches [95–97]. Zhang *et al.* [95] have proposed using an SLM and a microscope objective to generate an Airy beam in free-space and then coupling the free space radiation to surface plasmons using a linear diffraction grating. The SLM is used to imprint the desired cubic phase and the microscope objective performs the Fourier transform to provide the Airy beams at the back focal plane.

The homogeneous diffraction grating couples the Airy beams to surface plasmon mode to form the Airy SPPs. The usage of SLM and microscope objective gives additional degrees of freedom in controlling the propagation length, trajectory, and peak intensity location along the main lobe. In a different method, Li and co-workers [97] demonstrated the in-plane generation of Airy SPPs using a carefully designed nano-array structure. An array of nanocavities with chirped separation allowed for in-plane propagation of Airy-like SPP waves along with the air-silver interface. Both of the above methods were experimentally verified using leakage radiation microscopy [218]. Minovich *et al.* [96] have utilized a different grating coupling scheme exploiting the uniqueness and self-healing properties of Airy plasmons. A specially designed grating was used to imprint the phase profile of Airy function. The intensity distribution was probed with a near-field scanning optical microscope (NSOM) with single-photon counting capabilities at our research group [174, 219–223]. The experimental characterization using NSOM captures essentially all the details of scattered fields, however, the method has some limitations. The near-field probe used to collect the intensity can perturb the fields being measured and therefore may not be a true representation of the fields being generated at the surface. Another disadvantage performing a scan over a large area with high resolution requires an extremely large time. We have attempted to overcome limitations imposed by NSOM by using photoemission electron microscopy (PEEM) as another versatile experimental method. The scientific work of Minovich and co-workers acted as a bootstrap process to our research work. In our work, we have investigated the diffraction grating using an n-photon photoemission electron microscope (n-PEEM) over a large set of CW excitations. There are many advantages of using this experimental method over previously used experimental techniques e.g. SNOM and leakage radiation microscopy. PEEM can provide a spatial resolution down to 20 nm and can measure the fields over a large area in a relatively short span of time. It can be utilized to directly map the SPPs at nanometer resolution through photoemission, without the need for molecular reporters or a scanning probe tip. The diffraction grating for the Airy plasmon excitation is based
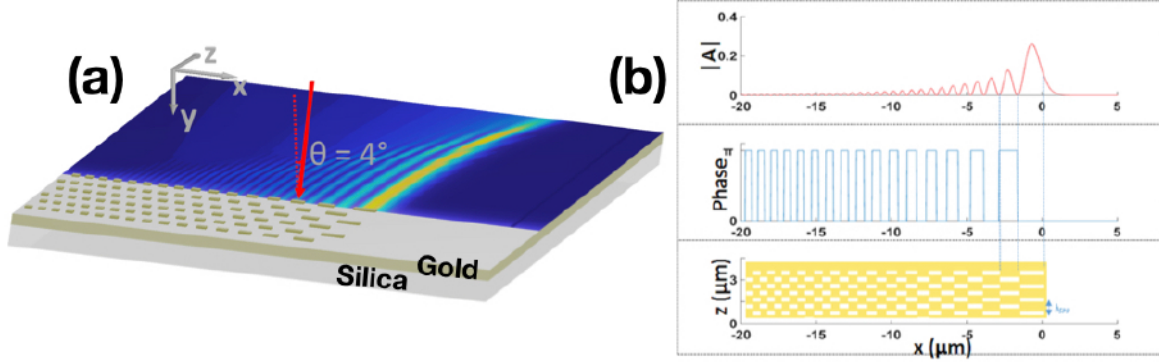
Figure 3.1. Generation of Airy plasmons: (a) schematic of the experimental set-up. A grating is excited from the top (airside). The airy plasmon is generated at the air-gold interface. The grating is composed of 11 periods with 200 nm thick slits (in the z-direction) and varying width in the x-direction. The Grating period is chosen according to the surface plasmon wavelength λ_{SPP} (= 745 nm) (b) Absolute value and phase of the airy function. The varying width of the grating along the x-direction is in accordance with the zeros of the Airy profile. Each consecutive column is displaced in the z-direction by $\lambda_{SPP}/2$ to match the phase change of π. The half-width of the main lobe is $x_0 = 700$ nm.

on the idea of Minovich et al. [96]. The specially designed grating generates the Airy plasmons by fulfilling the two basic requirements. First, the period of the grating provides the extra momentum to bridge the gap between the free space k-vector and the SPP k-vector. Second, it imprints the phase profile of the Airy wave by choosing the appropriate groove width along the transverse direction in accordance with the zeros of the Airy profile. The grating design is shown in Fig. 3.1 a. It consists of 11 arrays of periodic holes, whose period in the z-direction is governed by the SPP wavelength λ_{SPP} (745 nm). Every alternate column was shifted by half of the SPP wavelength to apply the required phase modulation of π. The hole size in the z-direction is fixed (200 nm) and in the x-direction represents the roots of the Airy function (Fig. 3.1 b). The first column width has been chosen to be $2x_0$ where x_0 is 0.7 µm. The scaling parameter is comparable to the SPP wavelength λ_{SPP}, therefore the paraxial solution does not describe precisely the propagation of the plasmon beam. The nonparaxial solution is provided in the above theory section by solving Maxwell's equations analytically.

Nonparaxial Airy plasmons provide a highly bending trajectory which is desirable to provide the noticeable change in trajectory over the short propagation length of Airy plasmons.
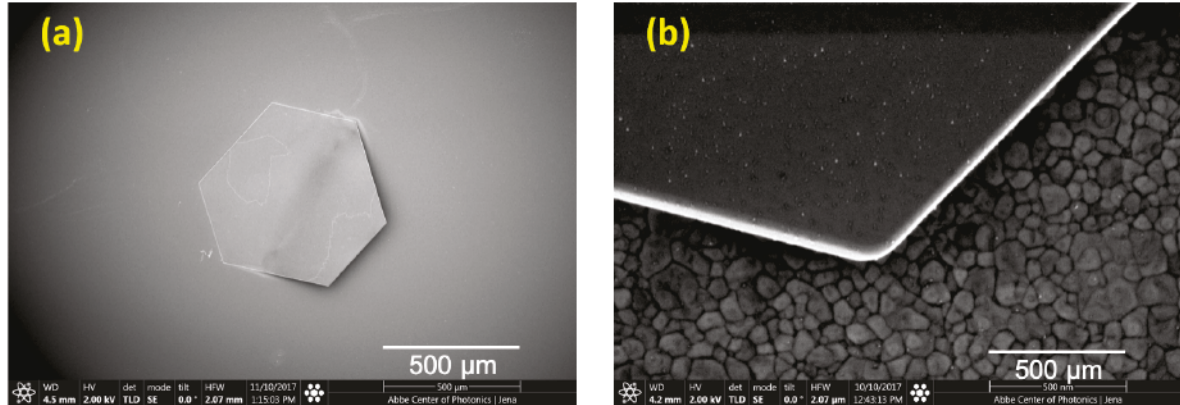

Figure 3.2. SEM image of self-assembled single-crystalline gold flake: (a)The flake has a very large diameter (700 μm) and (b) has locally very low surface roughness as compared to evaporated gold. The low roughness can make the n-photon photoemission process more deterministic. Figure courtesy of Stefan Fasold and Matthias Falkner at Abbe Center of Photonics, Germany.

The grating pattern was milled by a Focused Ion Beam (FIB) [224, 225] into a 200 nm thick polycrystalline gold film which was deposited on a fused silica substrate by evaporation (see inset in Fig. 3.3 a for an SEM micrograph). The FIB has removed the metal particles completely from the rectangular slits. The surface roughness of polycrystalline gold does not affect the Airy plasmon profile owing to the self-healing nature of the Airy wave. However, PEEM measurements are extremely sensitive to the surface roughness and might affect the n-photon photoemission yield. For this purpose, our group has also been involved in developing single-crystalline gold flakes to improve the deterministic process in PEEM measurements. This method is based on the self-assembly of gold nanoparticles [226, 227]. It produces single-crystalline gold flakes of large diameter (700 μm) (Fig. 3.2 a). Fig. 3.2 b shows a comparison of a gold flake and an evaporated gold surface. The gold flake surface has very low surface roughness as compared to the granular nature of evaporated gold.
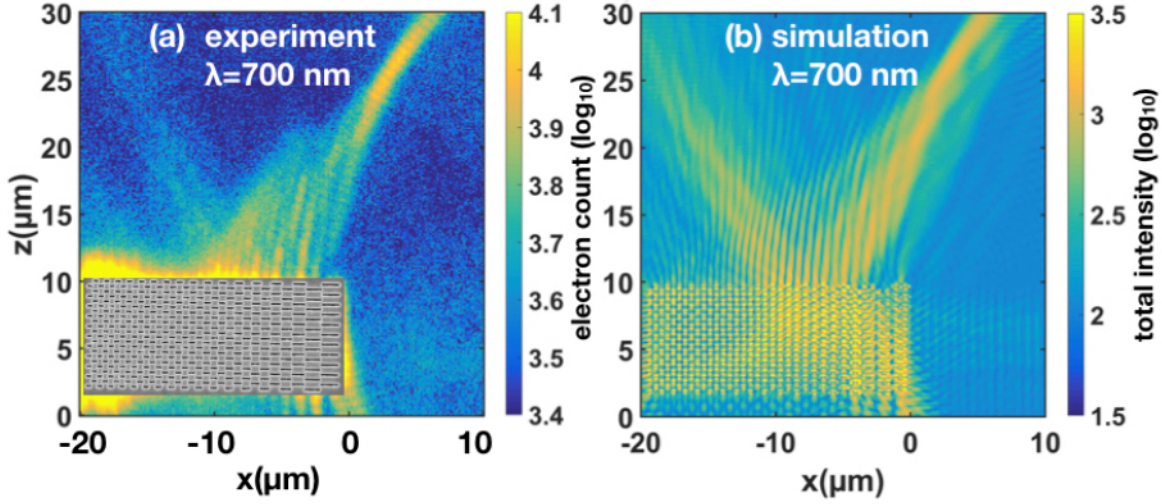
Figure 3.3. (a) Logarithmic plot of the experimentally measured PEEM electron yield of the Airy surface plasmon polaritons at inclined (4°) incidence illumination with a wavelength of $\lambda = 700$ nm. The image is overlaid with an SEM micrograph of the fabricated gold grating structure for the excitation of Airy plasmon(b) Logarithmic plot of the numerically calculated distribution of total intensity of Airy surface plasmon polaritons 5 nm above the gold-air interface at a wavelength of 700 nm. Here, the total intensity is obtained by interference of incident plane wave and scattered plasmon polaritons from the grating. Note that, the simulated result captures all the details found in the experimentally obtained image. Figure reproduced from reference [228].

As discussed before we used a PEEM (Focus GmbH, Germany) [229] to experimentally observe the generation of Airy SPPs. It studies the spatial dynamics of surface plasmons propagation from the grating by imaging the emitted photoelectrons from the metal surface. The emitted photoelectrons provide a map of the total fields as a result of interference of the plasmon polariton with the exciting electromagnetic fields. For the excitation light source, we used a home-built tunable optical parametric chirped pulse amplifier, which provides an average output power of 100 mW at the sample position with a repetition rate of 1 MHz, corresponding to a pulse energy of $0.1\,\mu$J. A TM polarized wide Gaussian beam is used to excite the grating at an angle of incidence of 4° from the normal in the yz-plane. The central wavelength of the excitation was varied between 670 nm and 840 nm. We used a pulse length of 500 fs with a

spectral bandwidth of 15 nm. The total exposure time for one image was 20 minutes. The rate of emitted electrons per laser pulse is small enough in order to suppress the detrimental interaction between multiple photoemitted electrons and was optimized to give the best signal-to-noise ratio in the experiments. Fig. 3.3 displays the qualitative comparison of experimental findings and numerically simulated results for an excitation wavelength of $\lambda = 700\,\text{nm}$. An overlaid SEM micrograph of the fabricated grating structure with the experimentally obtained image by the PEEM is shown in Fig. 3.3 a. On the air-gold interface, Airy SPP is launched by the diffractive grating and simultaneously interferes with the incident inclined plane wave at 4° with respect to the surface normal in the yz-plane. The photoemitted electrons provide the direct visualization of the resultant field. The area of constructive and destructive interference leads to higher and lower nonlinear photoemission yield. The measured electron yield by the multiphoton PEEM identifies the regions of constructive and destructive interference and provides a clear contrast between the higher and lower photoemission yield. This result clearly shows surface plasmon generation consisting of all the properties of the Airy beam such as bending of main lobe, non-diffracting nature of plasmon propagation. The main lobe of the Airy SPP propagates along a parabolically curved trajectory over a distance of $\approx 25\,\mu\text{m}$. In Fig. 3.3 b we compare the experimentally measured results with the one obtained theoretically by finite difference time domain method (FDTD) [189]. Large-scale 3D simulations have been performed using the commercially available software Lumerical FDTD solver [230]. The total field scattered field (TFSF) source is used for the simulation. This type of source is useful when an inclined plane wave illumination of nonperiodic devices is required. To perform the numerical calculation, we used multiple sources at a large set of wavelengths with 10 nm bandwidth under 4° incidence. The numerical results have been simulated using a narrowband source. The single frequency (or CW or steady-state) response is obtained with a Fourier transform of E(t) to give $E(\omega)$. The bandwidth chosen in the numerical simulation is comparable (10 nm) to the experimental source (15 nm). Since it is a narrowband source, the simulation must run for a sufficiently long time
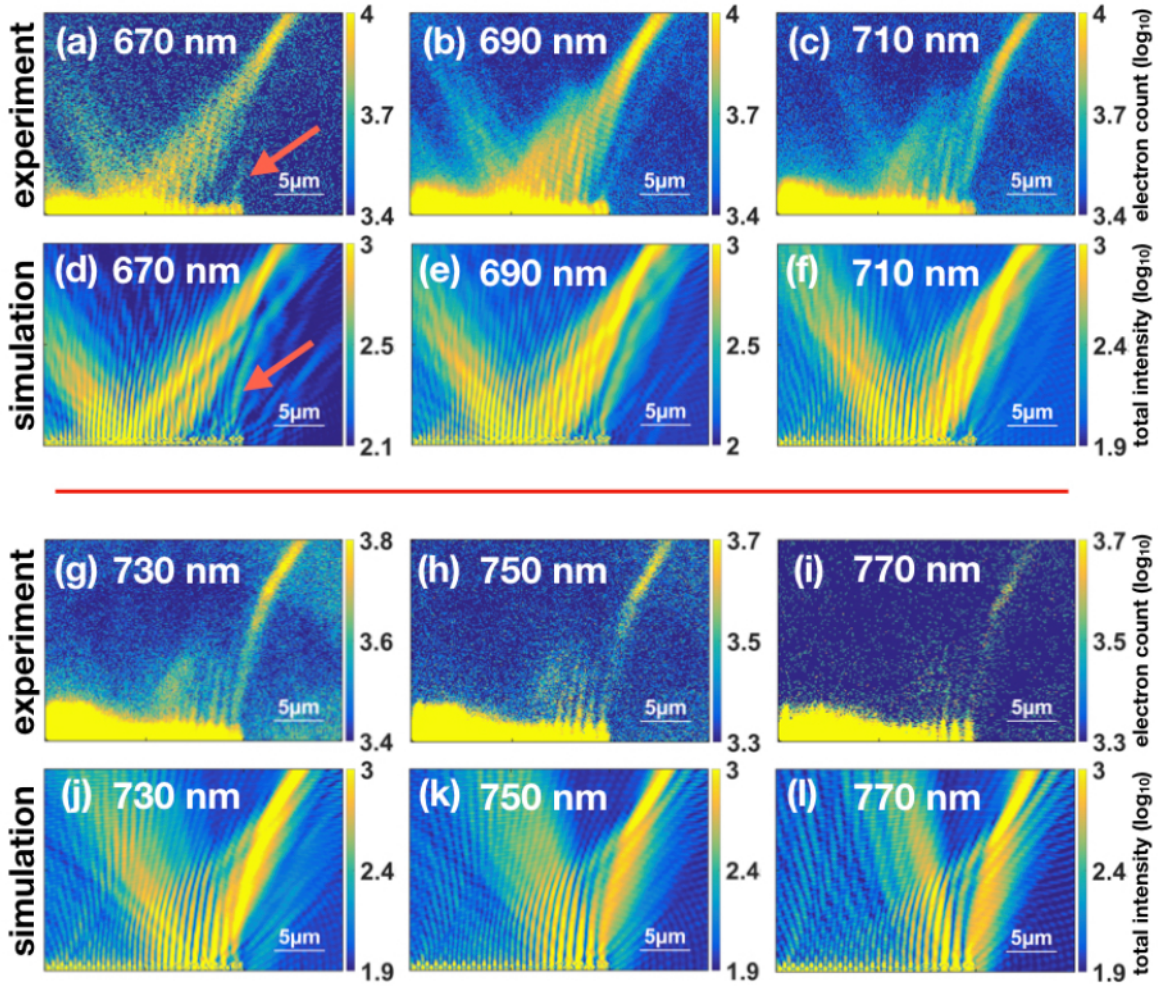
Figure 3.4. Qualitative comparison of experimental and FDTD near field intensity of Airy plasmon polaritons excited by a grating at 4° incidence: (a-c, g-i) Experimentally observed PEEM yield at wavelengths from 670 to 770 nm for wavelength steps of 20 nm. The log-scaled color bars are individually adjusted for the different wavelengths due to the nonlinear n-photon process in the photo emission. (d-f, j-l) Numerically calculated total light intensity 5 nm above the gold-air interface at the same wavelengths as for the PEEM experiments. The experimental electron yield distributions show a good agreement with the numerically calculated total intensity distributions at the different wavelengths, both indicating a travelling of the Airy SPPs along curved trajectories. At 670 nm, we observe generation of a weak lobe indicated by an arrow (Fig. 3.4 a,d), due to the excitation of second order modes in the slits of the grating. The effect diminishes at the longer wavelengths. Figure reproduced from the reference [228].

in order to reach a steady-state. Therefore, The simulation time is set to be 3000 fs. The spatial resolution used is $\Delta x = \Delta y = \Delta z = 5$ nm and $\Delta t = 0.0095$ fs. The near field intensity distribution is recorded 5 nm above the interface. The simulation region is chosen to be 30 µm × 0.85 µm × 30 µm. In Fig. 3.3 the total field is recorded which shows the interference of the incident source and the scattered field from the diffractive grating. Qualitatively, there is a good agreement between the electron yield in the experiment and the simulated total light intensity. Both plots capture similarly the details of the generated Airy plasmons and interference pattern with inherent phase information. Furthermore, the beam propagation method (BPM) was used to calculate the forward and backward propagating wave on the planer metal surface. The results have been found to match with the rigorous FDTD simulations.

The diffraction pattern is also suitable for the generation of the Airy plasmons over a broad range of wavelengths. For this purpose, we have studied the effect of a change in the excitation wavelength on the propagation dynamics from 670 nm to 770 nm at 20 nm wavelengths interval. The effect is comprehended in Fig. 3.4. The qualitative comparison of the measured PEEM yield and numerical simulations shows a good agreement. In this case, the numerical simulation records only the field scattered from the grating. At 670 nm, the first column of the grating shows the generation of a weak main lobe (indicated by a red arrow Fig. 3.4 a,d), which is a signature of excitation of second-order modes inside the grating grooves. The trajectory of the generated plasmon polaritons changes with the wavelength and the second-order mode effect diminishes at a longer wavelengths. The characteristic Airy plasmons properties such as bending and non-diffracting nature are preserved over the broad range of wavelengths. However, at longer wavelengths, the effect of non-paraxiality becomes more pronounced. The main lobe starts to breaks along the propagation direction beyond the wavelength of 750 nm (Fig. 3.4 k,l). Furthermore, a detailed insight of the structure in the perforated grating region gives information about localized surface plasmons as well (Fig. 3.5). This supports the generation of higher-order modes at lower wavelengths. The study becomes more fruitful in the context of n-photon PEEM
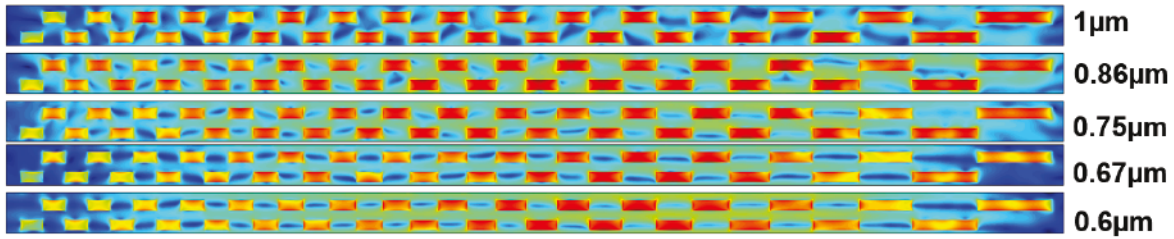
Figure 3.5. Localized plasmons inside a grating: numerically simulated image of 1 period of the grating under normal incidence at various wavelengths. The largest groove clearly shows a second order mode at lower wavelengths.

measurements. The experimental images clearly show that the electron yield starts decreasing significantly beyond 750 nm (Fig. 3.4 h,i). This can be explained by the fact that the photoemission in multiphoton PEEM is a nonlinear process and is very sensitive to the surface properties of the material. The work function of the evaporated gold used in our experiment is about 5 eV. The incident photon energy is 1.65 eV at 750 nm. This requires a three photon process for the electrons to reach the vacuum state. At higher wavelengths, the number of photons needed is even larger, and therefore the electron yield is very low. It should be noted that in our qualitative comparison, we have displayed the image on a logarithmic scale. It must be emphasized here that the photoemitted electron yield is not only a map of the actual electromagnetic field at the interface. The physics behind the photoemission process is complex. It requires a deeper understanding to provide a quantitative explanation of the correlation between electron yield and total electromagnetic field. As explained in chapter 2, the n-photon photoemission phenomenon can be described under the semi-classical theory of light-matter interaction. Under this framework, the matter is described under a quantum mechanical picture with the standard N-step linear photoemission model [143]. The model describes that for the photoelectron yield for n photon process, the photoemission intensity is proportional to the 2n power of the total electric field integrated over time. Here, the total value of the instantaneous electric field involves

polarization contributions perpendicular and parallel to the surface [231–234].

$$Y(\mathbf{r}) \propto \int_{-\infty}^{+\infty} |\mathbf{E}(\mathbf{r},t)|^{2n}\,dt$$
$$= \int_{-\infty}^{+\infty} \left[E_{\perp}^2(\mathbf{r},t) + E_{\parallel}^2(\mathbf{r},t)\right]^n dt \qquad (3.14)$$

Here $E_{\perp}(\mathbf{r},t)$ is the electric field normal to the metallic surface, and $E_{\parallel}(\mathbf{r},t)$ is the transverse field along the interface.

Effect of inclined incidence on asymmetric diffractive grating

The diffractive grating can generate co-propagating and counter propagating plasmons. In the previous sections we have presented experimental and numerical results on the co-propagating Airy plasmons. In this section, we present the counter-propagating plasmons and the effect of the asymmetric grating. In the case of counter-propagating plasmons (-4°) we observe an enhanced contrast of the total fields. The propagation dynamics differs significantly from the co-propagating case (Fig. 3.5). The coupling of plasmons starts at the first column of the grating edge at lower wavelengths (670 nm). As one can observe in Fig. 3.6 d,e,f the first column has significant extra radiation. This may be minimized by further optimizing the width of the first column hole. Fig. 3.6 depicts the comparison of experimental and numerical simulations. The photoemission yield decreases more rapidly than the co-propagating case with the increases in the wavelength of excitation. It can been observed by comparing Fig. 3.5 and Fig. 3.6 for wavelength 750 nm.

3.3. Bandwidth of Airy plasmons generation

The discussion in this chapter shows clearly that the diffractive grating can excite Airy plasmon for a broad range of wavelengths. Now we will calculate the efficiency of such plasmon generation over the wavelengths. We have seen in Fig. 3.4 the PEEM yield decreases significantly for longer wavelengths and is due to lower photon energy being
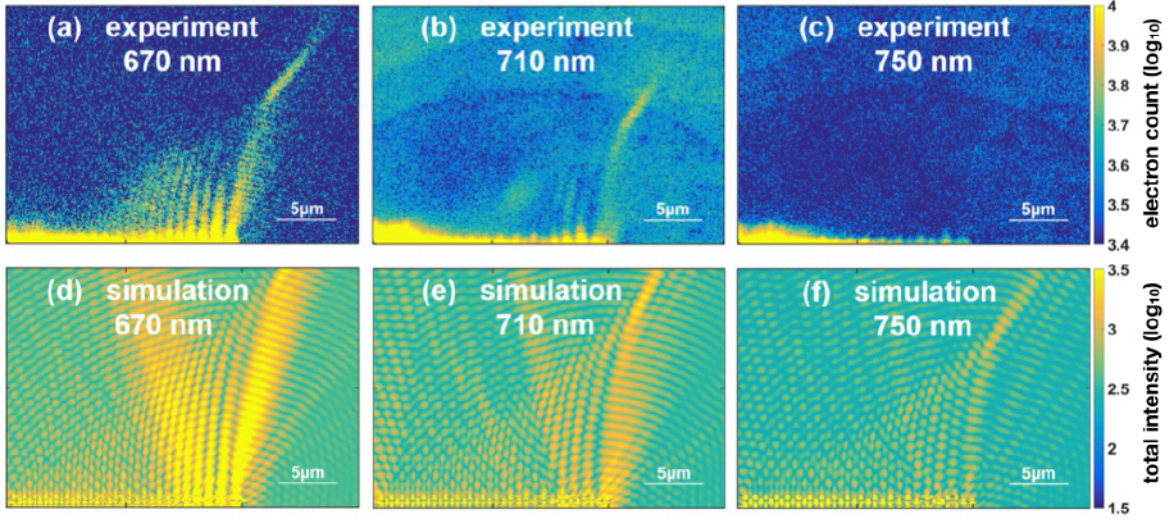
Figure 3.6. Qualitative comparison of experimental and simulated Airy plasmons at -4° incidence (counter-propagating): (a-c) static images of PEEM yield at wavelengths (a) 670 nm (b) 710 nm (c) 750 nm. (d-f) intensity map of simulated fields, recorded 5 nm above the interface at (d) 670 nm (e) 710 nm (f) 750 nm.

unable to extract photoelectrons from the metal surface. However, good correspondence between experimental and numerical results justifies extrapolating our studies to broader excitation wavelengths based on numerical simulations. Such broad wavelength studies are useful in a prospective application of ultrashort pulse excitation of the diffractive grating. In this section, we will calculate numerically if this diffractive structure has sufficient bandwidth for ultrashort pulse excitations or in other words to estimate numerically the bandwidth of the Airy plasmon's efficient excitation. In addition, we also study the effect of the angle of incidence on the generation efficiency, which can be further utilized in pulsed Airy plasmons investigation in a later section. The Airy plasmons generation efficiency is calculated by employing modal overlap calculations. The idea here is Airy plasmons' contribution to the scattered fields by the grating. This overlap integral analysis is performed over the wavelength range from 600 nm to 1100 nm for normal and oblique (4°) incidence. It measures the overlap of our numerical solution with an analytically derived Airy wave profile. This is done using the following overlap integral formula
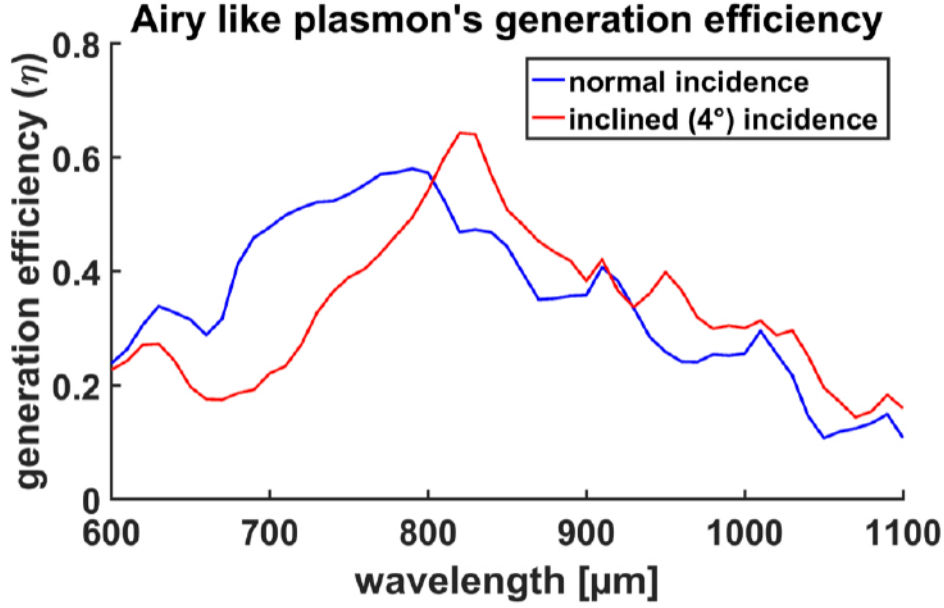
Figure 3.7. Generation efficiency η of Airy plasmons under normal incidence (blue curve) and 4° oblique incidence (red curve), calculated by the developed semianalytical model in Eq. (3.15) taking the overlap between numerical plasmons at $z_0 = 10\,\mu$m and analytically evolved Airy fields. For normal incidence the maximum generation efficiency is found to be $\eta \approx 58\%$ at 790 nm. At 4° incidence the efficiency is $\eta \approx 62\%$ and the maximum is shifted to 820 nm. Figure taken from the reference [228].

$$\eta = \left| Re\left[\frac{(\int \mathbf{E_a} \times \mathbf{H}_n^* . d\mathbf{S})(\int \mathbf{E}_n \times \mathbf{H}_a^* . d\mathbf{S})}{(\int \mathbf{E_a} \times \mathbf{H}_a^* . d\mathbf{S})} \right] \frac{1}{Re(\int \mathbf{E}_n \times \mathbf{H}_n^* . d\mathbf{S})} \right| \qquad (3.15)$$

here, subscript 'a' means analytical solution and 'n' stands for numerical solution. The numerical electric and magnetic field are calculated using Lumerical FDTD solutions.

Analytical electric and magnetic fields are calculated using the simple formulation from section 3.1.2, which provides an exact solution to the paraxial Helmholtz equation. We used the forward propagating analytical field to overlap with the numerical field at distance $z_0 = 10\,\mu$m. Since the numerical fields have no backward propagating mode, it is justified to use the overlap integral formula to calculate the Airy-like plasmon's generation efficiency. Fig. 3.7 depicts the dependence of Airy plasmon's generation efficiency on the wavelength of excitation under normal incidence (blue curve) and 4° oblique incidence (red curve). The maximum generation efficiency at
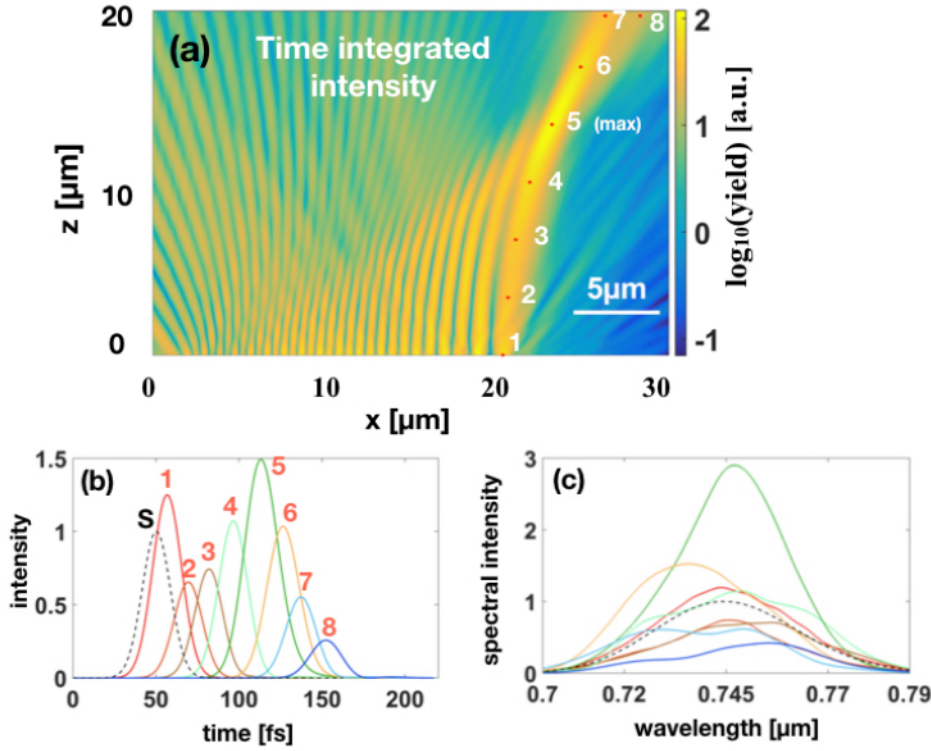
Figure 3.8. Simulated propagation dynamics of an Airy plasmon pulse: (a) Time-integrated spatial intensity evolution of the Airy plasmon for a pulsed 20 fs (FWHM) excitation centered at $\lambda = 745$ nm having a bandwidth of 40 nm (FWHM). Its noteworthy that despite of different acceleration trajectory of the different spectral components, the Airy plasmon pulse shows a common trajectory. (b) Time traces of the excitation source (dashed line) and Airy plasmon pulses (solid lines) at different spatial locations along the main lobe. 'S' stands for source. (c) Spectral intensity of source and pulsed Airy plasmons. The generation bandwidth of the grating is clearly of the same order as the incident source bandwidth. Figure reproduced from the reference [228].

normal incidence is 58% at 790 nm. At oblique incidence (4°) it becomes 64% and shifted to 820 nm. It is clear that the bandwidth of generation is large. It opens new pathways to excite the grating with short pulses. Now we will study the spatiotemporal propagation characteristics of Airy plasmon pulses generated at metal-dielectric interfaces by ultrashort pulse excitation with 20 fs (FWHM) gaussian pulses having a bandwidth, which easily fits into the excitation bandwidth demonstrated in

No.	x	z	$4\sigma_t$	$4\sigma_\nu$	$\Delta t \Delta \nu$
S	-	-	33.96	37.48	1.27
1	20.35	0	35.96	37.20	1.34
2	20.65	3.35	38.76	38.00	1.47
3	21.10	6.70	36.64	40.48	1.48
4	21.92	10.06	40.96	38.72	1.59
5	23.21	13.41	44.00	30.92	1.36
6	24.91	16.76	41.24	35.00	1.44
7	26.35	19.75	42.40	39.56	1.68
8	28.35	19.75	45.68	38.68	1.77

Table III.1. Time-bandwidth product of Airy plasmon pulse: Temporal width, spectral width and time band- width product of Airy plasmon pulse. Here we have used the ISO international standard definition of pulse width given by 4σ (4· standard deviation). 'S' stands for source, numbers 1 to 8 refer to the respective locations in Fig. 3.8 a. The time bandwidth product for a transform-limited Gaussian pulse is 1.27 (0.44 for FWHM definition). Note that the time bandwidth product becomes minimum at the highest intensity spot (denoted by point 5 in Fig. 3.8 a.) for the Airy plasmon pulse. Table reproduced from the reference [228].

Fig. 3.7. The study focuses on the ultrafast nano-optical dynamics of SPP propagation on the metal-dielectric interface. The numerical simulations have been performed using again Lumerical FDTD solutions. We expect that the influence due to inclined incidence is small as evident by the plot of generation efficiency. Therefore, we have here considered only normal incidence case. The central wavelength is chosen to be 745 nm, which is the center of the plateau of high excitation efficiency for normal incidence in Fig. 3.7. Fig. 3.8 shows the spatio-temporal dynamics of pulsed Airy plasmons. The spatial characteristics are recorded by temporal averaging of Airy plasmon pulse. Such a time-integrated image is depicted in Fig. 3.8 a. It clearly shows that the Airy plasmon pulse has all the characteristic properties such as self-bending and non-diffracting nature of Airy plasmons. Furthermore, the temporal evolution is depicted in Fig. 3.8 b. Several spatial points are chosen along the main lobe to visualize the tem-

poral shape of intensity. These points are numbered as 1 to 8 in Fig. 3.8 a. The dotted curve is the source signal with a 50.24 fs offset. As is evident in Fig. 3.8 b at point 1, the maximum temporal intensity is enhanced due to near field effects and then it dropped significantly at point 2. After this spatial point, the main lobe starts rebuilding itself with the side lobes, and the intensity increases monotonically. The intensity becomes maximum at point 5 and then the beam starts significantly diverging as clearly can be seen at points 7 and 8. For spatiotemporal characterization, it is important to have a quantitative picture of the time-bandwidth product. So we have also calculated the bandwidth at each spatial point shown in Fig. 3.8 c. The time-bandwidth product ($\Delta t \Delta \nu$) is presented in the table III.1. It shows that the product becomes minimum at maximum intensity points. These finding motivated us to further investigate possibilities of spatiotemporal coupling at the hot-spot of such non-diffracting surface plasmon pulses and will be subject of investigating in the next chapter.

3.4. Summary of results and related publication

The result of the above original research has been published in the peer-reviewed journal 'OSA Continuum' [228]. Airy plasmons propagation dynamics was investigated for a broad range of wavelengths using multiphoton PEEM and rigorous numerical simulations. The experimental and numerical results show good agreement. The constructive and destructive interference of the total electromagnetic field were mapped with n-PEEM. We have also developed a semianalytical formulation to quantify the Airy like plasmon generation efficiency from the diffraction grating and it is estimated to be $\approx 58\%$ under normal incidence and $\approx 62\%$ for 4° inclined incidence. This study provides a viable route to study ultra short Airy plasmon pulses and their spatio-temporal evolution. Furthermore, an active control over the trajectory could be obtained by employing 2D materials instead of metals. One such configuration could be the excitation of pulsed Airy plasmons on graphene, in which acceleration of the main lobe can be changed by tuning the Fermi energy of graphene [235].

IV. Spatiotemporal evolution of Airy surface plasmon pulses

In the previous chapter, we have investigated Airy plasmons generated by a diffraction grating. The diffraction grating was optimized for CW excitation. The generated plasmons have been studied numerically and experimentally. In this chapter, we explore the Airy plasmons generation under ultrashort pulse excitation. This particular type of plasmons has been termed as 'Airy plasmon pulses'. The generation of Airy plasmon pulses requires the optimization of the grating geometry for broadband pulsed excitations. The optimization process is discussed in detail in this chapter. The optimized design is investigated using numerical methods. We have also assisted our numerical results with an analytical and semi-analytical model. The spatiotemporal dynamics of Airy plasmon pulses is discussed in detail. A physical model is developed to understand the spatiotemporal dynamics of Airy plasmon pulse evolution. The chapter is organized as follows: in section 1, we design and optimize the Airy grating for efficient broadband Airy plasmon pulse generations. Section 2 provides analytical, semi-analytical, and numerical modeling schemes and their comparison. We further investigate in section 3 the spatiotemporal dynamics of Airy plasmon pulses in detail and develop a physical model to incorporate the space-dependent pulse evolution. Section 4 summarizes the results and provide routes for further research in this direction.
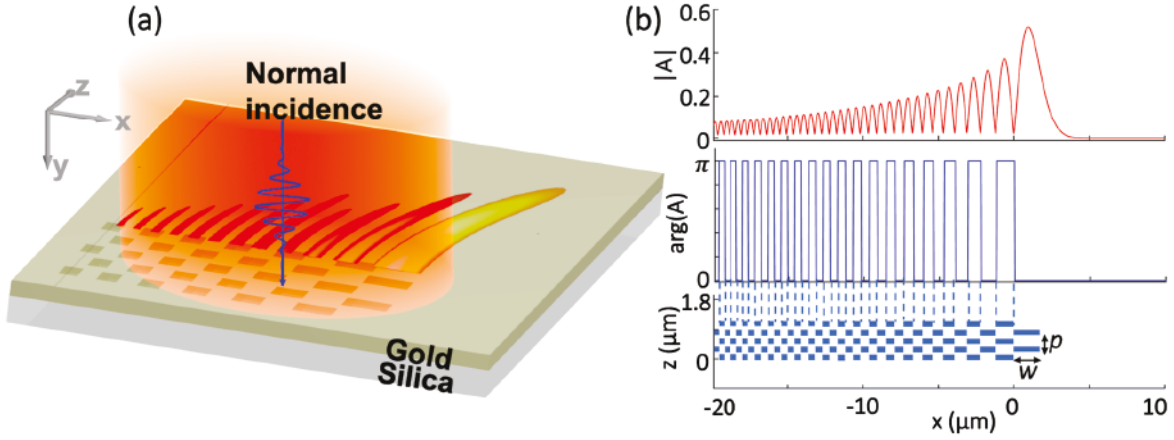
60

Figure 4.1. (a) Schematic of the sample layout: the grating is excited from the top (airside) at normal incidence (y-axis) with a femtosecond laser pulse. Pulsed Airy plasmons are excited by a diffraction pattern at the gold-air interface. The diffraction grating consists of 2.5 periods of the slit pattern. An image of an analytically calculated time-averaged Airy plasmon pulse is overlaid with the sample layout on the homogeneous gold surface after the grating (not to scale). (b) Absolute value and phase of the airy function. The varying width of the grating along the x-direction is in accordance with the zeros of the airy profile. Each consecutive column is displaced in the z-direction by $p/2$ to match the phase change of π, where p is the period of the grating. The half-width of the main lobe is $x_0 = 700\,\mathrm{nm}$. Each full period of the grating is composed of two elements to imprint the initial phase profile of the Airy wave. The slits are $(150\,\mathrm{nm})$ thick (in the z-direction) and the grating period in the z-direction is $p = 745\,\mathrm{nm}$.

4.1. Design and optimization of Airy grating

Airy plasmons are 1D non-diffracting, self-accelerating plasmonic beams propagating on a metal-dielectric interface. Since its first theoretical proposal by Siviloglou and Christodoulides [10], Airy plasmons have been experimentally observed contemporarily by Minovich et al. [96], Zhang et al. [95], and Li et al. [97]. Every experimental method has its advantages, but the method by Minovich et al. [96] is particularly interesting for our research work. The grating design [96] imprinted on the metal surface generates the Airy profile and simultaneously couples the free-space electromagnetic radiation to a metal-dielectric interface. This integrated design has been

optimized for a single wavelength. A high plasmon coupling efficiency was achieved for CW excitation by creating 11 grating periods. The new design adapts the Airy grating for CW excitation [96] to broadband ultrashort pulse excitations. Fig. 4.1(a) depicts the schematics of the sample layout. An ultrashort Gaussian pulse excites the grating from the top (air) side on the Gold surface. The permittivity of Gold is taken from Johnson and Christy as shown in Fig. 2.1. An image of a time-integrated Airy plasmon pulse is laid at the grating edge. The image is analytically calculated and is shown here just for an illustrative purpose. Fig. 4.1(b) shows the absolute value, the initial phase of the Airy function, and the Airy grating design. The Airy function is truncated by the finite size of the grating in transverse x-direction. The width of the grating slits in each column varies in the transverse x-direction defined by the roots of the Airy function, except the first column. The slit widths of the first column are chosen to be the full width of the Airy main lobe ($x_0 = 1.4\,\mu m$). Each consecutive column is displaced in the z-direction by half of the grating period, to imprint the initial phase shift of π of the Airy function. In this design, the grating period in the z direction is $p = 745\,nm$ and the thickness of the slit in the z-direction is 150 nm. In this section, the focus is to optimize the Airy grating for broadband Airy plasmons generations. This is achieved by calculating the Airy plasmons generation efficiency for different numbers of periods and slit thicknesses. The tool was developed and utilized in the last chapter to calculate the Airy plasmons generation efficiency from a grating (see section 3.3). Here, we reiterate the basic idea. The idea is that scattered fields from the grating are assumed to be made of Airy plasmons mode and non-Airy plasmons modes. The quantification of Airy plasmons modes from the scattered fields can be obtained using overlap integral formalism. This formalism is used in many situations in optics such as a beam from a laser has to be coupled into an optical fiber, or the mode of a master laser has to be matched with a slave laser. If the complex amplitude profile of the two beams is well matched in a certain plane, they will remain matched during further propagation. Therefore the overlap integral formula provides a quantification of a particular mode with respect to all possible modes in the optical system. We are
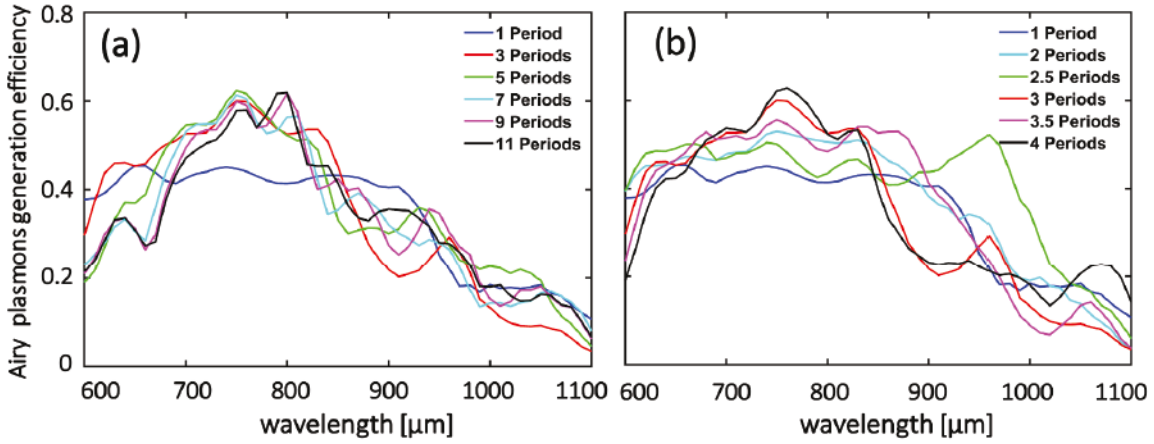
Figure 4.2. Design optimization for broadband Airy plasmons generation. Airy plasmons generation efficiency is calculated using Eq. (3.15) for a different number of periods. (a) for periods 1, 3, 5, 7, 9, and 11 the optimum generation efficiency is for 3 periods. (b) Optimizing the grating further for 3 periods. The generation efficiency is calculated for periods 1, 2, 2,5 3.5, and 4. The bandwidth is highest for 2.5 periods which is chosen for further spatio-temporal analysis.

quantifying the Airy plasmons mode generation from the grating with analytical Airy plasmons. Mathematically, the Airy plasmons generation efficiency is calculated by using formula 3.15.

Fig. 4.2 depicts the optimization results for the number of periods of the grating. Fig. 4.2(a) shows the Airy plasmons generation efficiency for the excitation wavelength range $\lambda = 600$ to $1100 \, \text{nm}$ for the number of periods 1, 3, 5, 7, 9, and 11. It can be noticed that the efficiency is maximum for $800 \, \text{nm}$ for 11 number of periods, which is desired for CW excitation at $800 \, \text{nm}$. However, the purpose of optimization in this case is to obtain a grating with the largest generation bandwidth, while maintaining a reasonable overall efficiency. Careful observation reveals that period 3 has the largest bandwidth with significant efficiency, therefore we decide to optimize the grating further around period 3. Figure 4.2(b) shows the Airy plasmons generation efficiency for number of periods 1, 2, 2.5, 3, 3.5, and 4. The generation bandwidth is the largest for 2.5 periods. It can also be noticed that periods 2.5 also has a higher generation

efficiency for longer wavelengths ranging from 900 nm to 1000 nm. In this optimization scheme, the slits thickness in z-direction was chosen to be 150 nm. Hence, the Airy grating with periods 2.5 and slit thickness 150 nm is the optimized design for generating Airy plasmon pulses. This design provides not only the largest generation bandwidth with significant generation efficiency but also a 77% reduction of overall grating size in the z-direction over previously reported design [96, 228].

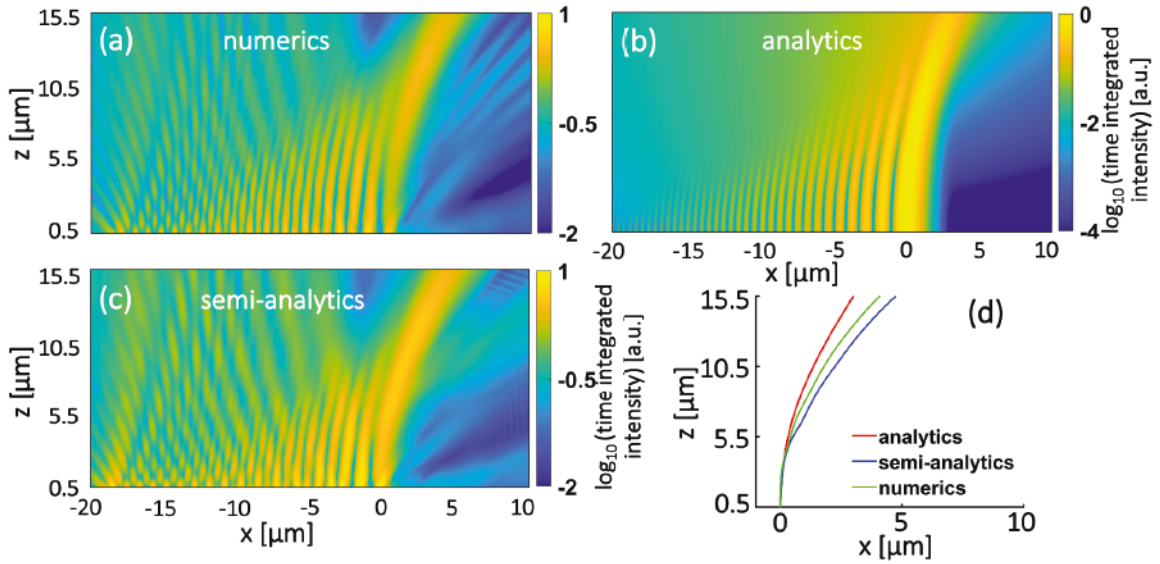## 4.2. Analytical, semi-analytical and numerical models

Figure 4.3. Numeric and semi-analytical model of Airy plasmon pulse excited by 6 fs Gaussian pulse centered at 800 nm. (a) Logarithmic plot of time-integrated intensity calculated using Finite Difference Time Domain method (FDTD). (b) Analytically calculated time-integrated intensity under paraxial approximation on logarithmic scale. (c) The time-domain response is calculated semi-analytically by using the impulse response of the grating. (d) The trajectory of the main lobe is compared for analytical, semi-analytical, and numerical models. The three models agree well with similar main lobe propagation trajectories.

Airy plasmon pulses are generated using the optimized grating obtained in the previous section. We have used Lumerical FDTD solutions to simulate the numeri-

cal spatiotemporal fields from the grating. For spatiotemporal simulation as depicted in Fig. 4.3 a of the manuscript, the spatial resolution is $\Delta x = \Delta y = \Delta z = 5\,\mathrm{nm}$ and temporal resolution is $\Delta t = 0.0095\,\mathrm{fs}$. The scattered field is recorded 5 nm above the interface in both space and time. The successive time frame for the time monitor is 0.3 fs (sampling rate=3278.66THz and down sampling time=32). In this case, the simulation time is 700 fs, which is enough for 20 fs pulse excitation. The large simulation region 38 μm × 0.6 μm × 44 μm ensures that there is no field reflected from the boundaries. The numerical model is assisted with an analytical and a semi-analytical model. Figure 4.3 shows the comparison of these models both qualitatively and quantitatively. In figure 4.3 (a), the logarithmic plot of the time-integrated Airy plasmon pulse is shown. We observe the generation of Airy lobes which are propagating along a bend trajectory and preserve their shape along the propagation direction. An analytically calculated time-integrated Airy plasmon pulse as shown in figure 4.3 (b) depicts the similar behavior of lobes. The analytical calculation is based on the nonparaxial solution of Airy plasmons 3.1.2 by superimposing the spectral components of 6 fs Gaussian pulse. The parameters were chosen for the half-width of the main lobe and the exponential apodization parameters are $x_0 = 0.7\,\mu m$ and $a = 0.04$. It is interesting to note that the spectral components of the nonparaxial solution of the Airy plasmon at longer wavelengths show breaking in main lobes intensity but superimposing the spectral component for 6 fs ultrashort pulse shows a better shape-preserving quality with a smoothly varying main lobe profile. Figure 4.3 (c) shows the time-integrated intensity using our semi-analytical model. In the semi-analytical model, the time domain response is calculated from the impulse response of the grating. The method can be divided into four steps:

- The impulse response function of the grating is calculated in Fourier domain using the FDTD simulation under CW excitation for wavelengths ranging from 600 nm to 1100 nm: $impulse(\nu)$.

- The spectrum of the input signal is obtained by Fourier transforming the transform-

limited Gaussian pulse: $signal(v)$.

- The impulse response of the system is multiplied by the input spectrum: $impulse(v) \cdot signal(v)$.

- Finally, the inverse Fourier transform of $impulse(v) \cdot signal(v)$ is computed to obtain the time domain response of the grating.

This is a standard method to calculate the time-domain response of a grating to an arbitrarily shaped pulse. Fig. 4.3(c) is qualitatively similar to the numerical simulation results in Fig. 4.3(a). It captures details of the generated Airy plasmons, as well as other plasmonic modes that are generated from the grating. The trajectory of the main lobe is compared for the analytical, semi-analytical, and numerical models in Fig. 4.3(d). It can be observed that the bending trajectory agrees quite well. It is also worth mentioning here that the analytical and the semi-analytical model have their limitations. In the analytical model, it is assumed that the Airy function is exponentially truncated and the semi-analytical model inherently assumes that there is no space-time coupling. The numerical model solves Maxwell's equations rigorously. The differences in the bending trajectory may be attributed to these differences in the models. Overall there is a good agreement between different models. The above analysis builds confidence in the accuracy of the numerical model and paves us a way to further investigate the spatiotemporal dynamics of Airy plasmon pulses numerically.

4.3. Spatiotemporal dynamics of Airy plasmon pulses

Intriguingly, Airy plasmon pulses have properties similar to their CW counterparts. Despite the ultrashort pulse excitation, Airy plasmon pulses propagate along a curved trajectory with self-similar field profiles. The time-integrated picture of the Airy plasmon pulse sets the stage for investigating it's spatiotemporal properties. In this section, our focus is to study the spatiotemporal evolution of Airy plasmon pulses. We divide it into two subsections, the first subsection deals with the temporal and spectral profile

and the second section is dedicated to developing a geometrical model to holistically incorporate the diffraction effects.

4.3.1. Temporal and spectral evolution of Airy lobes

The fact that Airy plasmon pulses are self-accelerating and non-diffracting makes them particularly interesting for studying their temporal and spectral evolution. Fig. 4.4 depicts such a spatiotemporal picture. In Fig. 4.4 (a), a time-averaged propagation of an Airy plasmon pulse is shown. We have chosen at first 8 equidistant spatial points on the main lobe's trajectory. These points are represented by numbers 1 to 8. The corresponding 3D plot for the temporal and spectral intensity distribution is shown in Fig. 4.4 (b) and (c) at the chosen spatial points. The intensities are normalized and have been plotted in a co-moving frame of reference as shown in Fig. 4.4 (b).
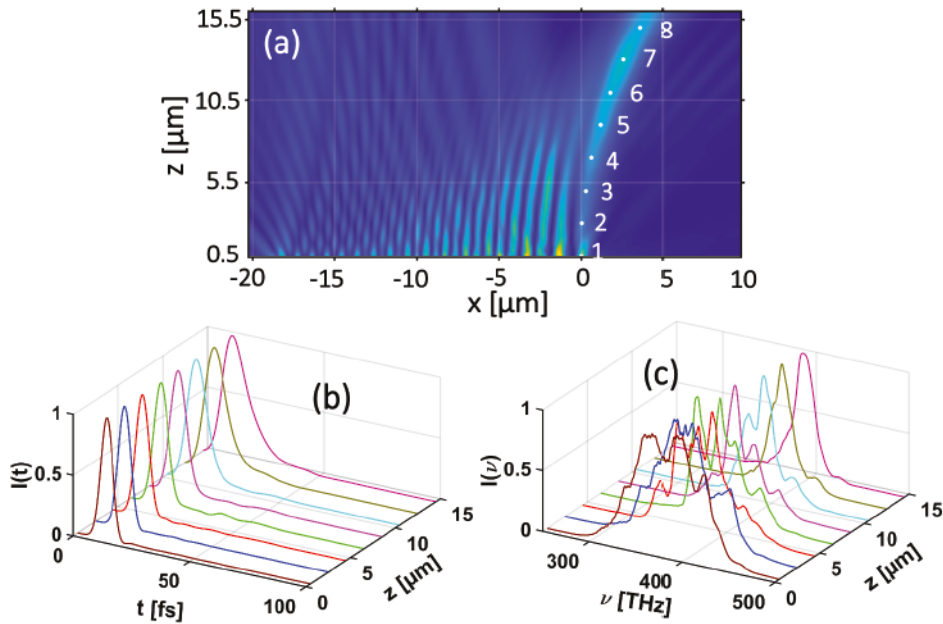

Figure 4.4. Temporal and spectral intensity evolution of main lobe: (a) Logarithmic plot for time-integrated Airy plasmon pulse intensity. (b) 3D plot for temporal intensity distribution at 8 equidistant points on the main lobe of the Airy plasmon pulse. (c) 3D plot for spectral intensity distribution at 8 equidistant points on main lobe of Airy plasmon pulse.

The initial Gaussian-like pulse profile evolves to acquire in an asymmetric shape. The 3D plot provides a cursory view of the pulse profile changes over propagation. The details of pulse shape and its interdependence on the grating design will be discussed quantitatively later in this section. Fig. 4.4 (c) represents the normalized spectral intensity plots. It can be noticed that the excitation grating results in a broadband spectral bandwidth at the initial propagation distance, which validates our diffraction grating design. However, the spectral width decreases significantly over the propagation distance of $15\,\mu$m. This poses the challenge to preserve the initial coupled bandwidth over the propagation distance. Another challenge is to have minimal temporal width for the available spectral width at longer distances. This problem may be solved by using a chirped pulse excitation to compensate for the dispersion effects, however, this requires first to calculate the spectral phase. Fig. 4.5, depicts the spectral
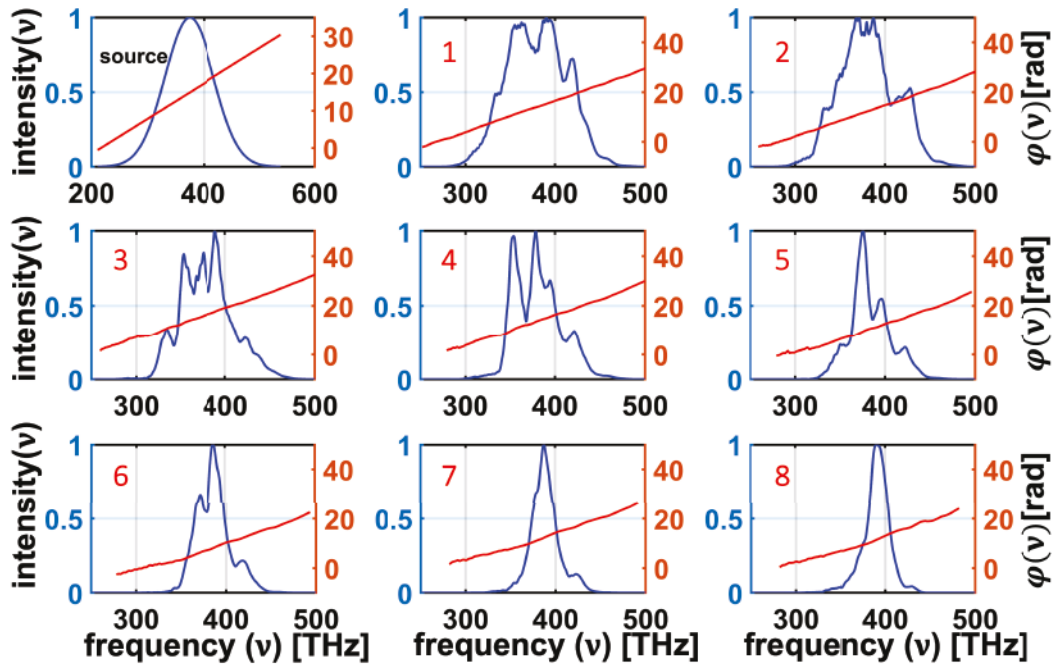

Figure 4.5. Spectral phase evolution plotted with corresponding spectral intensity at 8 equidistant spatial points on main lobe of Airy plasmon pulse as indicated in Fig. 4.4 (a). First subplot shows the spectral intensity and phase of a transform-limited incident source.

phase change over the 8 different spatial points on the main lobe. The first subplot of Fig. 4.5 shows the initial spectrum and phase of the transform-limited Gaussian pulse. The initial phase is linear, which is expected for a transform-limited pulse. The other 8 subplots correspond to the 8 different spatial points on the main lobe which had been shown in Fig. 4.4 (a). As can be seen, the spectral phase exhibits changes from a flat phase to a curved phase, however, the change is still small for all propagation distances. Therefore applying a second order negative chirp in the initial incident pulse would have a rather small impact on focusing the temporal pulse on propagation. Even though the spectral phase analysis is not so fruitful in pulse shaping, the temporal and spectral aspects are still worth exploring, which are the next subject of our investigation. The optimization of the diffraction grating (or Airy grating) depicted in Fig. 4.2 provides the largest excitation bandwidth, however, the maximum generation efficiency is only 52%. The moderate generation efficiency is the signature of a significant contribution of non-Airy plasmons to the total scattered field from the diffraction grating. It is important to comprehend the effects of non-Airy modes on the pulse shape and their evolution. The different excited modes are generated from the complex diffraction grating. Therefore, we compare the complex grating to a simple design of a single-column of slits. Our purpose is twofold: first, to carefully look at the Airy pulse profile evolution over the propagation distance and second, to uncover, if any, grating design-dependent dynamics. Fig. 4.6 (a) shows the time-integrated Airy plasmon pulse with 8 different locations at which temporal and spectral intensities are calculated. The temporal and spectral intensities are averaged over a transverse width of $0.7\,\mu m$ on the main lobe. In Fig. 4.4, we have not performed any spatial averaging because our goal was to calculate the spectral phase. The averaging in the present case is shown by white bars. The spatially averaged temporal intensities are plotted in Fig. 4.6 (c). The temporal profile has mainly the primary lobe with small secondary lobe contributions. An enlarged view of the secondary lobes is shown in the inset figure. At the first position $z = 0.5\,\mu m$, we observe only the primary pulse. The pulse starts spreading at subsequent propagation distances due to
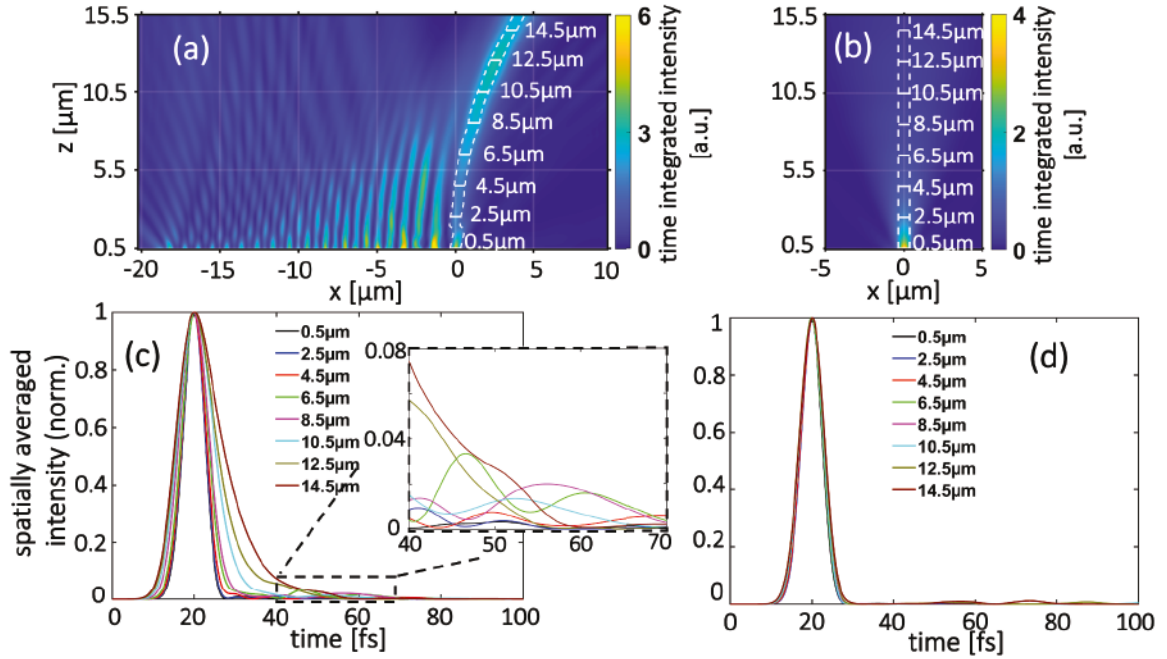
Figure 4.6. Spatial and temporal dynamics of plasmons excited by Airy grating and single-column slits: (a) Time integrated Airy plasmon pulse evolution. The white band follows the main lobe propagation and has a width of $0.7\,\mu m$. (b) Time integrated intensity of single column slits (having 2 periods with slit width $w = 1.4\,\mu m$, thickness $150\,nm$ and period $p = 745\,nm$). A White rectangular region with a width $0.7\,\mu m$ is used for spatial averaging along the x-direction. (c) Temporal intensity profile at 8 spatial locations starting from $z = 0.5\,\mu m$ at each $2\,\mu m$ distance in a co-moving frame over time. The temporal intensity is averaged over spatial width of $0.7\,\mu m$ (shown by white bars in (a)). In the inset, an enlarged view of the pulse profile for the temporal window $40\,fs$ to $70\,fs$ is also shown. (d) Temporal profile for Gaussian reference pulse spatial averaged over white bars at 8 subsequent propagation distances as shown in Fig. 4.6 (b).

dispersion effects. The secondary pulse profiles appear for propagation distances between positions $z = 4.5\,\mu m$ and $z = 10.5\,\mu m$, as shown in the inset of Fig. 4.6 (c). The secondary pulse contribution may be regarded as a diffracting non-Airy plasmons contribution from the grating. A geometrical model describing this diffraction grating effect on the pulse spreading will be discussed in detail in the next section. For positions $z = 12.5\,\mu m$ and $z = 14.5\,\mu m$, the primary pulse profile spreads largely due to

dispersion, and the secondary pulse profile is clearly absent.

As pointed out before to understand the complex grating effects, a simple single column slits design is considered as benchmark design. The time-integrated plasmons intensity scattered from the benchmark design is shown in Fig. 4.6 (b). It can be noticed that the pulsed plasmons generated from this simple structure, diffract quickly and the intensity becomes significantly lower already after $z = 5 \, \mu m$. For comparison purposes, the temporal intensities of the benchmark design are spatially averaged over the same transverse width $(0.7 \, \mu m)$ at the same distances as in the Airy grating case. Pulse spreading is negligible over the propagation distance of $z = 15 \, \mu m$ as can be expected from this simple configuration of slits. A quantitative comparison of the
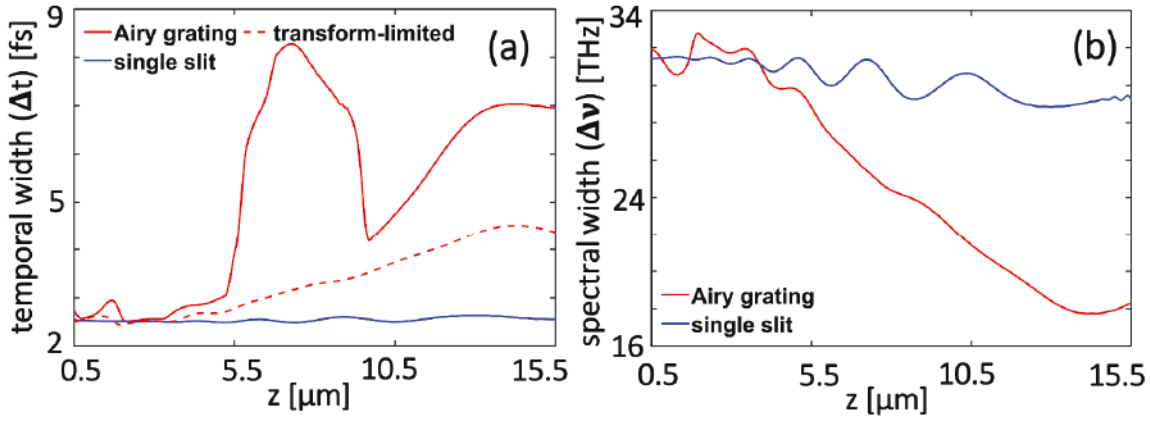

Figure 4.7. Comparison of the temporal and spectral width for the main lobe for excitation by Airy grating and single-column slits: (a) Temporal width over the propagation distance. The width changes abruptly in certain region, which may be attributed to non-Airy plasmon modes contributions. The dotted red curve shows the transform-limited temporal width. (b) Spectral width evolution over propagation direction. The spectral bandwidth decreases significantly over the propagation distance. Corresponding temporal broadening for the transform-limited case is larger than first column slits; however, the temporal width change for the Airy grating has spatial dependence.

pulse spreading is provided in the next Fig. 4.7 for both designs over all propagation distances. Temporal (Δt) and spectral $(\Delta \nu)$ widths are calculated by taking the second-order moment of the spatially averaged temporal and spectral intensities. For

Airy plasmon pulses spatial averaging is performed over the dashed white region on the main lobe as shown in Fig. 4.6 (a). In the case of the benchmark design (figure Fig. 4.7 (b)) the spatial average is calculated over the white box region. The transverse width of the spatial averaging is 0.7 μm in both cases. Fig. 4.7 (a) shows the temporal width change over the propagation distance. The main lobe of the Airy plasmon pulse undergoes appreciable changes, whereas the temporal width remains almost constant for the reference Gaussian pulse. At a distance approximately $z = 5$ μm there is a sharp increase in the temporal width of the Airy plasmon pulse, reaching a peak value, and then it decreases again. This hump in temporal width may be attributed to the contribution of the non-Airy plasmonic beams propagating from the diffraction grating and crossing the main lobe region. A justification of this hypothesis will be discussed in the next subsection. After this hump, the temporal width increases monotonically, which is due to planar metallic dispersion effects. In Fig. 4.7 (b), the spectral width for the main lobe of the Airy plasmon pulse decreases monotonically. A transform-limited temporal width of the pulse is calculated corresponding to the Airy pulse's spectral width. This is shown by a red dotted line in Fig. 4.7 (a). From Fig. 4.7 (a) and (b), it can be inferred that the hump in the temporal width variation is mainly due to the secondary pulses which arise from the diffraction grating geometry.

4.3.2. Geometrical model for spatio-temporal dynamics of Airy plasmon pulses

In our discussion on the temporal dynamics of Airy plasmons, it was found that abrupt changes in the temporal width have strong interdependence on the grating parameters. In this section, we explore systematically the dynamics of the temporal pulse width for the main lobe and the first 10 side lobes. Fig. 4.8 (a) shows once again, the time-integrated intensity of the Airy plasmon pulse, but this time we investigate the temporal width evolution for many lobes. The propagation distance of the side lobes is taken to the distance where the time-averaged intensity has decayed to 25 times the
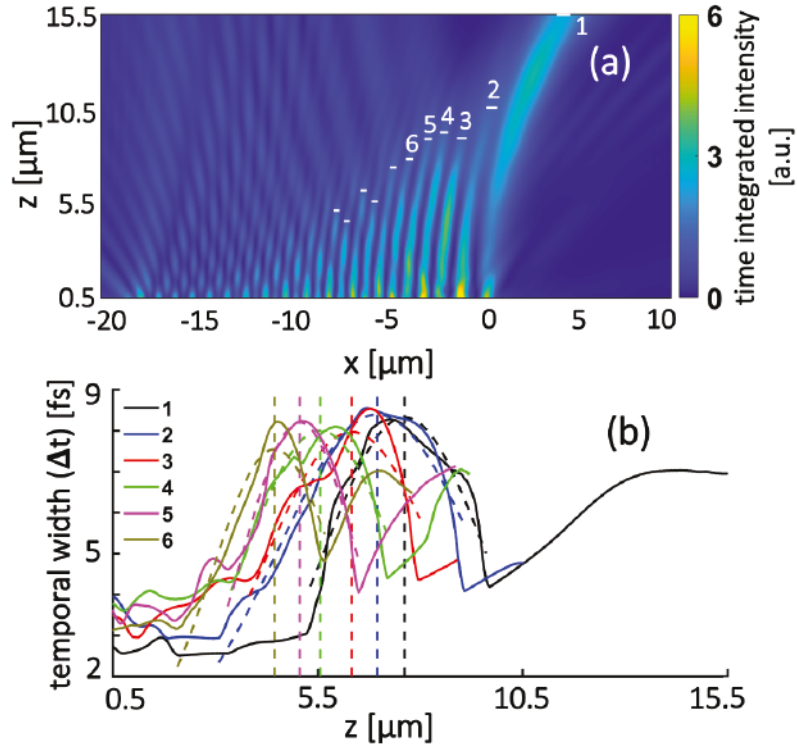
Figure 4.8. Space-dependent temporal dynamics and its interdependence on side lobes: (a) Time-integrated intensity on a linear scale. White bars illustrate the width over which spatial averaging is performed for calculating the temporal width corresponding to each lobe. Label 1 to 6 denotes the first 6 Airy lobes. (b) Temporal widths over the propagation distance for the main lobe (1) and the first five side lobes (2-6). A Gaussian fit has been performed for the humps in the temporal width region of lobes. Hump distances (shown as dotted vertical lines) are defined as the first order moment of the fitted curve.

background intensity. The temporal pulse length is evaluated by spatially averaging the lobes over a width which is indicated by the white bars in Fig. 4.8 (a) and which is equal to the respective grating column being responsible for the lobe's excitation. In Fig. 4.8 (a), the first six lobes are denoted by labels 1 to 6. The corresponding temporal width for the lobes 1 to 6 is shown in Fig. 4.8 (b). The typical hump, where the pulse length abruptly increases and then decays, is found for all lobes. As discussed before, the humps are characteristics of a secondary pulse profile as shown in Fig. 4.8 (c). The appearance and decay of secondary pulses, which are delayed with respect to the main

pulse, are inherently involved in the humps profile. The center of mass of these humps is calculated by applying Gaussian fits. The center of mass or the hump's position is denoted by vertical dashed lines for each respective lobes. This position will be called hump distance Z_n. It can be observed that as the lobe number n increases, the hump distance for the lobe shifts towards smaller propagation distances.
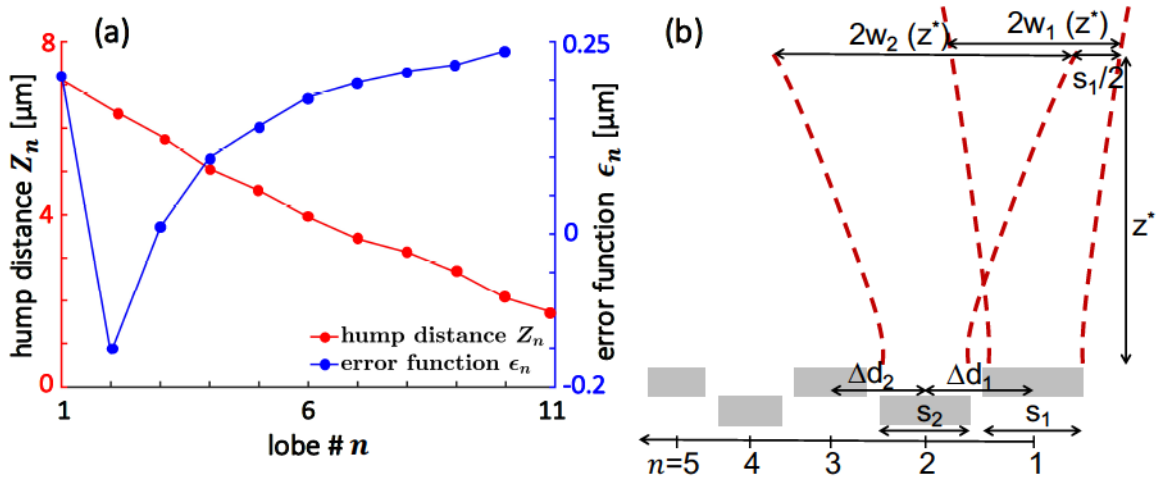

Figure 4.9. A grating parameter-dependent geometrical model for the description of the spatio-temporal dynamics: (a) red: Hump distance Z_n for the lobes $n = 1 \ldots 11$ derived from the rigorous simulation, which illustrates at which propagation distance z the secondary pulse appears on the lobe's trajectory leading to a sudden increase in the overall pulse length. blue: Error value ϵ_n of Eq. 4.1, which indicates the discrepancy of where our simple geometrical model predicts the appearance of the secondary pulse from where it really appears in the rigorous numerical simulations. (b) Sketch of a simple geometrical model to explain the occurrence of the secondary pulses in the Airy lobe's trajectory.

To understand and explain the observed temporal dynamics of Airy plasmon pulses, we developed a simple geometrical model. This model particularly incorporates the characteristic positions of the humps in the consecutive lobes shown in Fig. 4.8 (b). The model is validated by comparing it to the already presented findings from the rigorous numerical simulations. We start by having a look at the hump distance Z_n, which is plotted for the individual lobes $n = 1 \ldots 11$ in Fig. 4.9 (a). The plot captures the trend that for larger lobe numbers n the humps occur already for shorter propaga-

tion distances z. This observation is explained by our model, which assumes that the used binary excitation grating gives rise to a significant non-Airy plasmon mode contribution. These non-Airy parts of the excitation evolve on a different trajectory than the Airy plasmon mode. Hence, both parts interfere, which is observed as a perturbation of the Airy lobe's pulse dynamics. Our physical model describes this interference according to the scheme depicted in Fig. 4.9 (b). The scheme is based on the assumption that the trajectories of both parts of the excitation can be modeled approximately by Gaussian beams. The sketch shows the binary grating elements, from which Airy and non-Airy plasmon pulses are excited. To obtain the quantitative description of the physical model, each grating element is characterized by two parameters: its transverse size s_n and its distance to the next grating element Δd_n, where 'n' stands for nth Airy lobe originating from the nth grating element. Our model assumes that the secondary pulses, which had been shown in Fig. 4.6 (c), appear when the non-Airy part of the excitation crosses a lobe of the Airy-part of the excitation. Assuming that the non-Airy part of the excitation can be modelled by a Gaussian beam, a secondary pulse should appear at a propagation distance, when this non-Airy part of the excitation of grating element $n + 1$ overlaps spatially with lobe n, which originated from grating element n.

To verify this assumption by an analytical expression, we model both, the trajectory of the Airy-lobe as well as non-Airy part by a simple Gaussian model. In the case of the Gaussian model, the analytical solution for the temporal pulse width evolution can be obtained in the first-order approximation [163]. The analytical solution for the evolution of the half-width $w_n(z)$ of a Gaussian beam, which is excited by slit n, is calculated by assuming that the slit's size s_n determines the initial half-width of the Gaussian as $w_n(0) = s_n/2$. If the half-width $w_n(z)$ characterizes the spreading of the non-Airy part as well as the trajectory of the Airy lobe n, the interference of the two, should occur at a propagation distance z^* for which

$$w_n(z^*) + \Delta d_n - s_n/2 - w_{n+1}(z^*) = \epsilon_n \doteq 0. \tag{4.1}$$

This condition considers that the non-Airy part originating from slit $n+1$ spreads faster than the Airy-lobe from slit n moves to the side. Since the size s_{n+1} is smaller than s_n, this gives rise to a more rapid Gaussian beam diffraction from slit $n+1$. The condition is therefore fulfilled if the spreading of a Gaussian beams caught up with its neighbor at a distance $\Delta d_n - s_n/2$. Fig. 4.9 (a) shows the error function ϵ_n of Equation 4.1, which illustrates that our model is quantitatively sufficiently close to the rigorous numerical simulations to support the stated general ideas of the model. However, it is clear that our model is just a very simple geometric representation of a complex scattering problem, which can't explain all details. One drawback of this model is that it does not consider the Airy lobe's caustics. The additional limitation comes from the paraxial approximation of Gaussian beam propagation, which is increasingly wrong for smaller slit sizes as can be seen from the growing absolute value of the error function ϵ_n for larger lobe numbers n in Fig. 4.9 (a). Despite these limitations, the model could be utilized for tailoring the non-Airy plasmon part to shape the Airy plasmon's pulse profile, e.g. by tuning the geometrical parameters of the grating.

The scattered fields from the grating have many modes, which makes the analysis very complex. However, a general trend in temporal and spectral behaviors can be observed by taking a spatial average over the planar metallic region. Three spatial regions are chosen for our analysis. The first region has 10 lobes, the second has 20 lobes and the third contains the full simulation area. The spatial averaging of Airy plasmon pulse intensity is performed between red curves (Fig. 4.10(a) and (b)) for the first and second regions in the transverse direction. For the third region, the spatial averaging is over the entire simulation domain in the transverse direction. Fig. 4.10 (c) shows the temporal width over the propagation distance after averaging the intensity in the transverse direction. In the case of the second and third regions, the temporal width changes randomly in the shaded region and increases monotonically after $z = 3\,\mu$m (the vertical dashed line). For the first region with 10 lobes, the temporal width changes monotonically over the entire propagation distances. This is an interesting trend in temporal width evolution and results from the finite size of the grating.
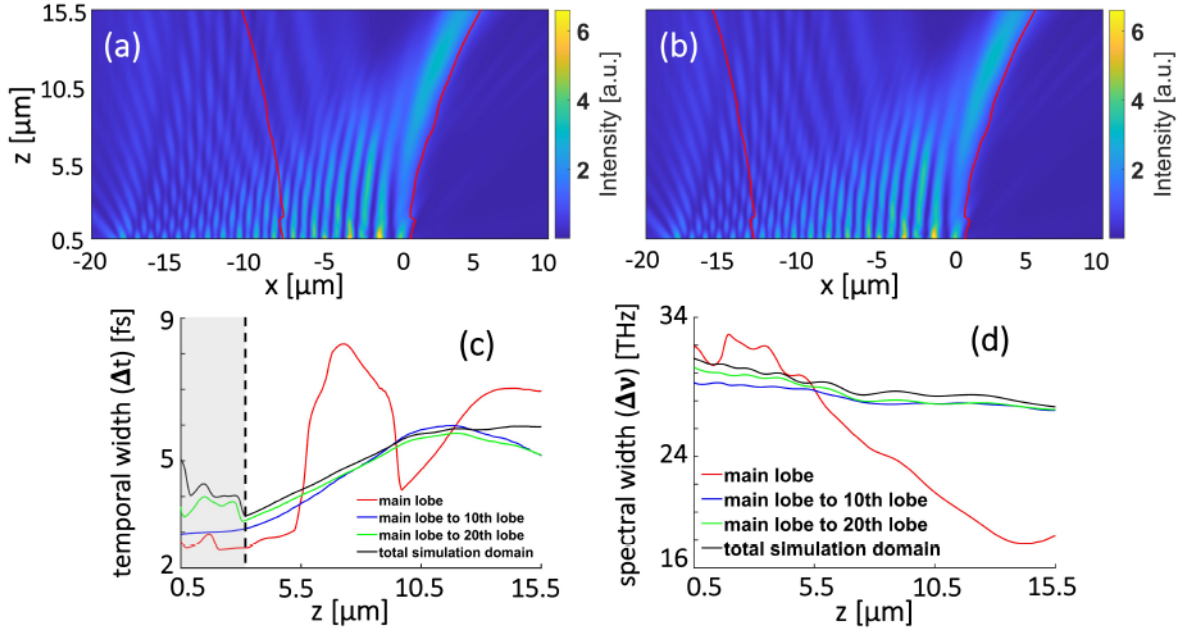
Figure 4.10. Average temporal and spectral width trend over different spatial regions: (a) Time-integrated intensity of Airy plasmons with spatial region of 10 lobes. The area between the red curves is used for spatial averaging. (b) same image as in figure (a) but with 20 lobes spatial region. (c) temporal width comparison for spatially averaged regions of 10 lobes, 20 lobes and total simulation domain. (d) spectral width evolution for spatially averaged regions of 10 lobes, 20 lobes, and total simulation domain. In Figures c and d, the main lobe's temporal and spectral width are added for reference.

When the spatial averaging region is increased, the contribution of the non-Airy modes increases. This results in randomly scattered fields distribution in the near fields.

In this chapter, we have formed a solid framework of understanding of Airy plasmon pulse dynamics, on which future research ideas can be laid out. Here, we provide an outlook for possible future research directions. One could use a curved grating for changing the slope of hump distance curve in Fig. 4.9 (a) and potentially achieve temporal focusing for minimal spot size in space and time. Furthermore, the input pulse shape can be used as an additional degree of freedom to control and engineer the pulsed plasmonic beams on the metal-dielectric interface. An example of this pulsed plasmonic beam can be Airy-Airy plasmonic pulsed beams, which uses Airy pulse as

an incident source and can exploit its non-dispersive properties for non-varying pulse shape. These engineering methods provide only the passive control of the pulsed beam on the metal-dielectric interface. Active control of the shape and spatiotemporal properties may be achieved by utilizing the tunable properties of 2d materials such as Graphene.

4.4. Summary and related publication

In summary, we studied analytically, semi-analytically, and numerically the spatiotemporal evolution of Airy plasmon pulses. A diffraction grating has been optimized for the generation of broadband Airy plasmons. The optimization is performed for a maximum bandwidth of the Airy plasmon generation, resulting in a broad generation bandwidth from $\lambda = 600\,\text{nm}$ to $1100\,\text{nm}$. The grating size is also reduced to just 2.5 periods, much shorter than previously reported diffraction gratings. The optimized grating is used to efficiently generate ultrashort Airy plasmon pulses. The numerical results are quantitatively compared with analytical and semi-analytical models and are found in good agreement. The numerically simulated results are further explored for the spatiotemporal dynamics of Airy plasmon pulses. A study of spectral phase evolution on the main lobe suggests that chirped pulse excitation may not be optimal for temporal width control with this grating design. Temporal and spectral intensity evolution characteristics are investigated in detail by calculating the temporal and spectral width variation over the propagation distance. After comparing with a benchmark design, it is concluded that the scattered field from the grating has significant non-Airy modes contributions. The shape of the temporal width for different lobes has been systematically explored and a grating-parameter-dependent geometrical model is developed. The geometrical model is used to predict the distance at which the temporal distance increases abruptly. This geometrical model may be used to tune the grating parameters for temporal focusing to provide spatio-temporal pulsed beams with highly localized spot-size. The results of this work have been submitted for review in a peer-reviewed

optics journal [236].

V. Summary and outlook

This thesis aimed to add a new layer of knowledge to our existing knowledge base of propagation invariant beams. There have been substantial collaborative efforts in carefully designing and executing this aim. This thesis can be encapsulated in two major projects, one project belongs to Airy plasmons and their experimental investigation using n-PEEM and another project is on spatiotemporal pulsed Airy plasmons. In this last chapter of the thesis, we provide a summary of our main results and provide our perspective for future directions.

We have started our work based on the established work in the field of Airy plasmons and took a step forward by investigating the Airy plasmons using the state-of-the-art experimental technique n-PEEM. PEEM is a tool to directly visualize and measure the electromagnetic field from a metallic surface through photoemission. The photoemitted electron yield provides a map of the electromagnetic field at the surface. The photoemission is a nonlinear multiphoton process and therefore the photoemitted electron yield is sensitive to the excitation wavelength. A diffractive grating based on Minovich et al. [96] was optimized for a lower resonant wavelength as compared to the original design [96]. In the experimental configuration, we used a home-built tunable optical parametric chirped pulse amplifier, which excites the diffraction grating with a Gaussian beam of diameter $80\,\mu m$ over $670\,nm$ to $840\,nm$ wavelengths range. The surface plasmons emitted from the grating interfere with the incident light source and the resultant interference pattern is mapped with the n-PEEM. The measured electron yield by the n-PEEM captures the region of constructive and destructive interference and provides the a clear contrast between higher and lower photoemission yield. In

80

addition to this phase information, there are also other advantages of using PEEM over the previously used NSOM method [96]. In NSOM, the presence of a scanning probe perturbs the field being measured, so the measurement may not be a true representation of the unperturbed field properties of interest. The scanning time in NSOM is also large, which poses further challenges. PEEM has overcome these challenges and has proven to be a versatile tool in measuring electromagnetic fields at metallic surfaces. The optimization of our grating and theoretical verification of experimental results were performed using large scale 3D simulations. We have used the open-source software MEEP and the commercial software Lumerical for this purpose. These software tools are based on the finite difference time domain method. The numerical and experimental results show a good agreement. Both results exhibit the Airy plasmons self-accelerating and propagation invariant features. In the experiment, it has been observed that photoemission yield becomes very low for wavelengths above 750 nm due to the lower photon energy being insufficient to extract photoelectrons in the PEEM by a two photon process and the much lower efficiency of the three photon process. This sets a limitation on the experimental investigation for broader excitation spectrum, but the good correspondence between experimental and numerical results has motivated us to extrapolate the numerical study. A quantitative analysis was performed to calculate the Airy plasmon generation efficiency of the diffraction grating over 600 nm to 1100 nm wavelength range. We have used modal overlap calculations to obtain the Airy plasmons' generation efficiency. The modal overlap integral formula measures the overlap between a numerical solution and the analytically derived Airy wave profile. The Airy plasmons' generation efficiency was found to be large, which opens up the possibility to short-pulse excitation of the grating. We performed preliminary numerical studies using 20 fs Gaussian pulse excitation on the grating to generate pulsed Airy plasmons.

The broadband generation of pulsed Airy plasmons has motivated us to take one step forward into investigating the spatiotemporal evolution of Airy plasmon pulses. In this project, we have first optimized the grating response for ultrashort pulse exci-

tations. In the first project, the grating was optimized for a resonant wavelength and had lower generation efficiencies for higher wavelengths. The modal overlap integral formula has been utilized once again for the optimization of the generation bandwidth. The slit thickness and number of periods have been two important parameters over which the grating has been optimized while keeping the fabrication feasibility in mind for future experimental studies. The generation bandwidth is found to be largest for a slit width of 150 nm and periods 2.5. The optimized configuration is then investigated for the spatiotemporal evolution of Airy plasmon pulses using analytical, semi-analytical, and numerical methods. The analytical model is based on the nonparaxial Airy wave solution developed in the first project. The time-averaged intensity of an Airy plasmon pulse is calculated by superimposing the nonparxaial Airy plasmons for the spectral components of a 6 fs pulse. The time-averaged intensity exhibits nondiffracting and self-accelerating properties similar to their CW counterparts. Further, a semi-analytical model was applied to calculate the time-domain response of the grating. A semi-analytical model is a standard method to efficiently calculate the time-domain response to an arbitrary signal in a linear system. The analytical and semi-analytical models were then compared with the rigorous 3D finite-difference time-domain method, calculated using a commercial Lumerical-FDTD electromagnetic solver. The time-averaged intensity calculated using the three different models was in good agreement. The generated pulsed beam maintains quasi-nondiffracting and self bending properties. The main lobe trajectory was also compared for the three models and agreed fairly well. Spatiotemporal analysis of the complex Airy grating is challenging. The challenge has been overcome by first comparing the spatiotemporal dynamics with a simple design. As discussed in chapter 4 of the thesis, the specific features of temporal dynamics were better understood as a result of the comparison with the benchmark design. These specific features of temporal dynamics were utilized in developing a deeper understanding of Airy plasmon pulses' dynamics. A physical model incorporates the temporal width features of pulsed Airy plasmons' lobes and predicts the pulse broadening based on the superposition of scattered fields from the

grating.

The investigations in the field of spatiotemporal dynamics of Airy plasmon pulses suggest that the Airy grating can provide temporally focussed nondiffracting spatiotemporal pulsed beams with highly localized spot size. The experimental verification of the pulsed Airy plasmons' spatiotemporal evolution can be carried out by combining PEEM with ultrafast laser excitation in a configuration known as time-resolved PEEM. There has been a long-standing fascination to produce propagation invariant wave packets in plasmonics. Our research concludes that an ultrashort Airy plasmon pulse retains its non-diffracting characteristics. These interesting results pave the path for generating 'plasmonic bullets' by combining the Airy pulse as an ultrafast excitation on the Airy grating. However one has to be careful in the case of ultrashort excitation, as space-time coupling is inherent in such cases. Recently, a numerical study [237] has shown the generation of propagation invariant pulsed SPP wave packets by utilizing spatiotemporal correlations. This approach is similar to free space space-time light sheets [110–113], except for the fact that correlations stem from the SPP light cone rather than the free-space light cone. The space-time coupled ultrashort subwavelength SPP wave packets have shown orders of magnitude larger propagation invariant length compared to traditional Gaussian pulsed SPP wave packets. 'Plasmonic bullets' may unleash the hidden potential of plasmonics.

References

[1] M. V. Berry and N. L. Balazs. »Nonspreading wave packets«.
In: *Am. J. Phys.* 3 (1979).

[2] E. Schrödinger.
»An undulatory theory of the mechanics of atoms and molecules«.
In: *Physical Review* 28.6 (1926), p. 1049.

[3] J. Durnin. »Exact solutions for nondiffracting beams. I. The scalar theory«.
In: *JOSA A* 4.4 (1987), pp. 651–654.

[4] J. Durnin, J. Miceli Jr, and J. Eberly. »Diffraction-free beams«.
In: *Physical Review Letters* 58.15 (1987), p. 1499.

[5] J. C. Gutiérrez-Vega, M. Iturbe-Castillo, and S. Chávez-Cerda.
»Alternative formulation for invariant optical fields: Mathieu beams«.
In: *Optics Letters* 25.20 (2000), pp. 1493–1495.

[6] M. A. Bandres, J. C. Gutiérrez-Vega, and S. Chávez-Cerda.
»Parabolic nondiffracting optical wave fields«.
In: *Optics Letters* 29.1 (2004), pp. 44–46.

[7] D. McGloin and K. Dholakia. »Bessel beams: diffraction in a new light«.
In: *Contemporary Physics* 46.1 (2005), pp. 15–28.

[8] R. Stützle, M. Göbel, T. Hörner, E. Kierig, I. Mourachko, M. Oberthaler,
M. Efremov, M. Fedorov, V. Yakovlev, K. Van Leeuwen, et al.
»Observation of nonspreading wave packets in an imaginary potential«.
In: *Physical Review Letters* 95.11 (2005), p. 110405.

[9] J. C. Gutiérrez-Vega and M. A. Bandres. »Helmholtz–gauss waves«.
In: *JOSA A* 22.2 (2005), pp. 289–298.

[10]   G. A. Siviloglou and D. N. Christodoulides.
       »Accelerating finite energy Airy beams«.
       In: *Optics Letters* 32.8 (2007), pp. 979–981.

[11]   J. Turunen and A. T. Friberg. »Propagation-invariant optical fields«.
       In: *Progress in Optics* 54 (2010), pp. 1–88.

[12]   Y. Hu, G. A. Siviloglou, P. Zhang, N. K. Efremidis, D. N. Christodoulides,
       and Z. Chen.
       »Self-accelerating Airy beams: generation, control, and applications«.
       In: *Nonlinear Photonics and Novel Optical Phenomena*. Springer, 2012,
       pp. 1–46.

[13]   M. A. Bandres, I. Kaminer, M. Mills, B. Rodríguez-Lara, E. Greenfield,
       M. Segev, and D. N. Christodoulides. »Accelerating optical beams«.
       In: *Optics and Photonics News* 24.6 (2013), pp. 30–37.

[14]   A. E. Minovich, A. E. Klein, D. N. Neshev, T. Pertsch, Y. S. Kivshar, and
       D. N. Christodoulides.
       »Airy plasmons: non-diffracting optical surface waves«.
       In: *Laser & Photonics Reviews* 8.2 (2014), pp. 221–232.

[15]   U. Levy, S. Derevyanko, and Y. Silberberg. »Light modes of free space«.
       In: *Progress in Optics* 61 (2016), pp. 237–281.

[16]   L. Schiff. *Quantum Mechanics*. 3rd ed. Vol. 15.
       McGraw-Hill Education, 1968.

[17]   O. Vallée and M. Soares. *Airy Functions and Applications to Physics*.
       World Scientific, 2004.

[18]   D. M. Greenberger. »Comment on "Nonspreading wave packets"«.
       In: *American Journal of Physics* 48.3 (1980), pp. 256–256.

[19]   R.-S. Penciu, V. Paltoglou, and N. K. Efremidis. »Closed-form expressions
       for nonparaxial accelerating beams with pre-engineered trajectories«.
       In: *Optics Letters* 40.7 (2015), pp. 1444–1447.

[20]   M. Berry. »Stable and unstable Airy-related caustics and beams«.
       In: *Journal of Optics* 19.5 (2017), p. 055601.

References

[21] Y. A. Kravtsov and Y. I. Orlov. *Caustics, catastrophes and wave fields*. Vol. 15. Springer Science & Business Media, 2012.

[22] D. Bongiovanni, Y. Hu, B. Wetzel, R. A. Robles, G. M. González, E. A. Marti-Panameño, Z. Chen, and R. Morandotti. »Efficient optical energy harvesting in self-accelerating beams«. In: *Scientific Reports* 5.1 (2015), pp. 1–7.

[23] B. K. Singh, R. Remez, Y. Tsur, and A. Arie. »Super-Airy beam: self-accelerating beam with intensified main lobe«. In: *Optics Letters* 40.20 (2015), pp. 4703–4706.

[24] G. Siviloglou, J. Broky, A. Dogariu, and D. Christodoulides. »Observation of accelerating Airy beams«. In: *Physical Review Letters* 99.21 (2007), p. 213901.

[25] D. M. Cottrell, J. A. Davis, and T. M. Hazard. »Direct generation of accelerating Airy beams using a 3/2 phase-only pattern«. In: *Optics Letters* 34.17 (2009), pp. 2634–2636.

[26] H. Dai, X. Sun, D. Luo, and Y. Liu. »Airy beams generated by a binary phase element made of polymer-dispersed liquid crystals«. In: *Optics Express* 17.22 (2009), pp. 19365–19370.

[27] T. Ellenbogen, N. Voloch-Bloch, A. Ganany-Padowicz, and A. Arie. »Nonlinear generation and manipulation of Airy beams«. In: *Nature Photonics* 3.7 (2009), pp. 395–398.

[28] D. Papazoglou, S. Suntsov, D. Abdollahpour, and S. Tzortzakis. »Tunable intense Airy beams and tailored femtosecond laser filaments«. In: *Physical Review A* 81.6 (2010), p. 061807.

[29] S. Longhi. »Airy beams from a microchip laser«. In: *Optics Letters* 36.5 (2011), pp. 716–718.

[30] I. M. Besieris, A. M. Shaarawi, and R. W. Ziolkowski. »Nondispersive accelerating wave packets«. In: *American Journal of Physics* 62.6 (1994), pp. 519–521.

[31] M. A. Bandres. »Accelerating beams«. In: *Optics Letters* 34.24 (2009), pp. 3791–3793.

[32] E.-Y. Song, G.-Y. Lee, H. Park, K. Lee, J. Kim, J. Hong, H. Kim, and B. Lee. »Compact generation of airy beams with C-aperture metasurface«. In: *Advanced Optical Materials* 5.10 (2017), p. 1601028.

[33] Z. Li, H. Cheng, Z. Liu, S. Chen, and J. Tian. »Plasmonic airy beam generation by both phase and amplitude modulation with metasurfaces«. In: *Advanced Optical Materials* 4.8 (2016), pp. 1230–1235.

[34] W. Hao, M. Deng, S. Chen, and L. Chen. »High-efficiency generation of Airy beams with Huygens' metasurface«. In: *Physical Review Applied* 11.5 (2019), p. 054012.

[35] B. Yu, J. Wen, L. Chen, L. Zhang, Y. Fan, B. Dai, S. Kanwal, D. Lei, and D. Zhang. »Polarization-independent highly efficient generation of Airy optical beams with dielectric metasurfaces«. In: *Photonics Research* 8.7 (2020), pp. 1148–1154.

[36] R. Feng, B. Ratni, J. Yi, K. Zhang, X. Ding, H. Zhang, A. de Lustrac, and S. N. Burokur. »Versatile Airy-Beam Generation Using a 1-Bit Coding Programmable Reflective Metasurface«. In: *Physical Review Applied* 14.1 (2020), p. 014081.

[37] H. Li, W. Hao, X. Yin, S. Chen, and L. Chen. »Broadband generation of airy beams with hyperbolic metamaterials«. In: *Advanced Optical Materials* 7.20 (2019), p. 1900493.

[38] Q. Fan, W. Zhu, Y. Liang, P. Huo, C. Zhang, A. Agrawal, X. Luo, Y. Lu, C. Qiu, H. Lezec, et al. »Generation of photonic spin-controlled accelerating light beams along arbitrary curved trajectories«. In: *Nano Letters* 19.2 (2019), p. 1158.

[39] J. A. Davis, M. J. Mitry, M. A. Bandres, and D. M. Cottrell. »Observation of accelerating parabolic beams«. In: *Optics Express* 16.17 (2008), pp. 12866–12871.

[40] G. Siviloglou, J. Broky, A. Dogariu, and D. Christodoulides. »Ballistic dynamics of Airy beams«. In: *Optics Letters* 33.3 (2008), pp. 207–209.

References

[41]   Y. Hu, P. Zhang, C. Lou, S. Huang, J. Xu, and Z. Chen.
»Optimal control of the ballistic motion of Airy beams«.
In: *Optics Letters* 35.13 (2010), pp. 2260–2262.

[42]   J. W. Goodman. *Introduction to Fourier optics*.
Roberts and Company Publishers, 2005.

[43]   J. Wen, L. Chen, B. Yu, J. B. Nieder, S. Zhuang, D. Zhang, and D. Lei.
»All-dielectric synthetic-phase metasurfaces generating practical airy
beams«. In: *ACS Nano* 15.1 (2021), pp. 1030–1038.

[44]   J. Broky, G. A. Siviloglou, A. Dogariu, and D. N. Christodoulides.
»Self-healing properties of optical Airy beams«.
In: *Optics Express* 16.17 (2008), pp. 12880–12891.

[45]   Z. Bouchal, J. Wagner, and M. Chlup.
»Self-reconstruction of a distorted nondiffracting beam«.
In: *Optics Communications* 151.4-6 (1998), pp. 207–211.

[46]   P. Polynkin, M. Kolesik, J. V. Moloney, G. A. Siviloglou, and
D. N. Christodoulides.
»Curved plasma channel generation using ultraintense Airy beams«.
In: *Science* 324.5924 (2009), pp. 229–232.

[47]   P. Polynkin, M. Kolesik, and J. Moloney.
»Filamentation of femtosecond laser Airy beams in water«.
In: *Physical Review Letters* 103.12 (2009), p. 123902.

[48]   P. Panagiotopoulos, D. Papazoglou, A. Couairon, and S. Tzortzakis.
»Sharply autofocused ring-Airy beams transforming into non-linear
intense light bullets«. In: *Nature Communications* 4.1 (2013), pp. 1–6.

[49]   P. Panagiotopoulos, A. Couairon, M. Kolesik, D. G. Papazoglou,
J. V. Moloney, and S. Tzortzakis.
»Nonlinear plasma-assisted collapse of ring-Airy wave packets«.
In: *Physical Review A* 93.3 (2016), p. 033808.

[50]   C. Liu, L. Niu, K. Wang, and J. Liu. »3D-printed diffractive elements
induced accelerating terahertz Airy beam«.
In: *Optics Express* 24.25 (2016), pp. 29342–29348.

[51] E. R. Dowski and W. T. Cathey.
»Extended depth of field through wave-front coding«.
In: *Applied Optics* 34.11 (1995), pp. 1859–1866.

[52] W. T. Cathey and E. R. Dowski. »New paradigm for imaging systems«.
In: *Applied Optics* 41.29 (2002), pp. 6080–6092.

[53] S. Jia, J. C. Vaughan, and X. Zhuang. »Isotropic three-dimensional
super-resolution imaging with a self-bending point spread function«.
In: *Nature Photonics* 8.4 (2014), pp. 302–306.

[54] T. Vettenburg, H. I. Dalgarno, J. Nylk, C. Coll-Lladó, D. E. Ferrier,
T. Čižmár, F. J. Gunn-Moore, and K. Dholakia.
»Light-sheet microscopy using an Airy beam«.
In: *Nature Methods* 11.5 (2014), pp. 541–544.

[55] J. Nylk, K. McCluskey, M. A. Preciado, M. Mazilu, Z. Yang,
F. J. Gunn-Moore, S. Aggarwal, J. A. Tello, D. E. Ferrier, and K. Dholakia.
»Light-sheet microscopy with attenuation-compensated
propagation-invariant beams«. In: *Science Advances* 4.4 (2018), eaar4817.

[56] D. G. Grier. »A revolution in optical manipulation«.
In: *Nature* 424.6950 (2003), pp. 810–816.

[57] J. Baumgartl, M. Mazilu, and K. Dholakia.
»Optically mediated particle clearing using Airy wavepackets«.
In: *Nature Photonics* 2.11 (2008), pp. 675–678.

[58] J. Baumgartl, G. M. Hannappel, D. J. Stevenson, D. Day, M. Gu, and
K. Dholakia.
»Optical redistribution of microparticles and cells between microwells«.
In: *Lab on a Chip* 9.10 (2009), pp. 1334–1336.

[59] H. Cheng, W. Zang, W. Zhou, and J. Tian. »Analysis of optical trapping
and propulsion of Rayleigh particles using Airy beam«.
In: *Optics Express* 18.19 (2010), pp. 20384–20394.

[60] Z. Zheng, B.-F. Zhang, H. Chen, J. Ding, and H.-T. Wang.
»Optical trapping with focused Airy beams«.
In: *Applied Optics* 50.1 (2011), pp. 43–49.

[61]   Z. Zhang, D. Cannan, J. Liu, P. Zhang, D. N. Christodoulides, and Z. Chen. »Observation of trapping and transporting air-borne absorbing particles with a single optical beam«. In: *Optics Express* 20.15 (2012), pp. 16212–16217.

[62]   A. Mathis, F. Courvoisier, L. Froehly, L. Furfaro, M. Jacquot, P.-A. Lacourt, and J. M. Dudley. »Micromachining along a curve: Femtosecond laser micromachining of curved profiles in diamond and silicon using accelerating beams«. In: *Applied Physics Letters* 101.7 (2012), p. 071110.

[63]   M. Manousidaki, D. G. Papazoglou, M. Farsari, and S. Tzortzakis. »Abruptly autofocusing beams enable advanced multiscale photo-polymerization«. In: *Optica* 3.5 (2016), pp. 525–530.

[64]   N. Götte, T. Winkler, T. Meinl, T. Kusserow, B. Zielinski, C. Sarpe, A. Senftleben, H. Hillmer, and T. Baumert. »Temporal Airy pulses for controlled high aspect ratio nanomachining of dielectrics«. In: *Optica* 3.4 (2016), pp. 389–395.

[65]   N. K. Efremidis and D. N. Christodoulides. »Abruptly autofocusing waves«. In: *Optics Letters* 35.23 (2010), pp. 4045–4047.

[66]   D. G. Papazoglou, N. K. Efremidis, D. N. Christodoulides, and S. Tzortzakis. »Observation of abruptly autofocusing waves«. In: *Optics Letters* 36.10 (2011), pp. 1842–1844.

[67]   Y. Jiang, K. Huang, and X. Lu. »Propagation dynamics of abruptly autofocusing Airy beams with optical vortices«. In: *Optics Express* 20.17 (2012), pp. 18579–18584.

[68]   A. V. Novitsky and D. V. Novitsky. »Nonparaxial Airy beams: role of evanescent waves«. In: *Optics Letters* 34.21 (2009), pp. 3430–3432.

[69]   N. K. Efremidis, Z. Chen, M. Segev, and D. N. Christodoulides. »Airy beams and accelerating waves: an overview of recent advances«. In: *Optica* 6.5 (2019), pp. 686–701.

[70] J. Dorfmüller, R. Vogelgesang, R. T. Weitz, C. Rockstuhl, C. Etrich, T. Pertsch, F. Lederer, and K. Kern. »Fabry-Pérot resonances in one-dimensional plasmonic nanostructures«. In: *Nano Letters* 9.6 (2009), pp. 2372–2377.

[71] K. Awazu, M. Fujimaki, C. Rockstuhl, J. Tominaga, H. Murakami, Y. Ohki, N. Yoshida, and T. Watanabe. »A Plasmonic Photocatalyst Consisting of Silver Nanoparticles Embedded in Titanium Dioxide«. In: *Journal of the American Chemical Society* 130.5 (2008), pp. 1676–1680.

[72] L. Martin-Moreno, F. Garcia-Vidal, H. Lezec, K. Pellerin, T. Thio, J. Pendry, and T. Ebbesen. »Theory of extraordinary optical transmission through subwavelength hole arrays«. In: *Physical review letters* 86.6 (2001), p. 1114.

[73] G. Gay, O. Alloschery, B. V. De Lesegno, C. O'Dwyer, J. Weiner, and H. Lezec. »The optical response of nanostructured surfaces and the composite diffracted evanescent wave model«. In: *Nature Physics* 2.4 (2006), pp. 262–267.

[74] P. K. Jain, X. Huang, I. H. El-Sayed, and M. A. El-Sayed. »Review of some interesting surface plasmon resonance-enhanced properties of noble metal nanoparticles and their applications to biosystems«. In: *Plasmonics* 2.3 (2007), pp. 107–118.

[75] J. N. Anker, W. P. Hall, O. Lyandres, N. C. Shah, J. Zhao, and R. P. Van Duyne. »Biosensing with plasmonic nanosensors«. In: *Nanoscience and Technology: A Collection of Reviews from Nature Journals* (2010), pp. 308–319.

[76] A. M. Shrivastav, U. Cvelbar, and I. Abdulhalim. »A comprehensive review on plasmonic-based biosensors used in viral diagnostics«. In: *Communications Biology* 4.1 (2021), pp. 1–12.

[77] V. Rutckaia and J. Schilling. »Ultrafast low-energy all-optical switching«. In: *Nature Photonics* 14 (2020), pp. 4–6.

[78] Z. Xie, W. Yu, T. Wang, H. Zhang, Y. Fu, H. Liu, F. Li, Z. Lu, and Q. Sun. »Plasmonic nanolithography: a review«. In: *Plasmonics* 6.3 (2011), pp. 565–580.

References

[79] A. A. Maradudin, J. R. Sambles, and W. L. Barnes. *Modern plasmonics*. Elsevier, 2014.

[80] J. Shao, E. A. Josephs, C. Lee, A. Lopez, and T. Ye. »Electrochemical etching of gold within nanoshaved self-assembled monolayers«. In: *ACS Nano* 7.6 (2013), pp. 5421–5429.

[81] W. Srituravanich, N. Fang, C. Sun, Q. Luo, and X. Zhang. »Plasmonic nanolithography«. In: *Nano letters* 4.6 (2004), pp. 1085–1088.

[82] B. Walther, C. Helgert, C. Rockstuhl, F. Setzpfandt, F. Eilenberger, E.-B. Kley, F. Lederer, A. Tünnermann, and T. Pertsch. »Spatial and Spectral Light Shaping with Metamaterials«. In: *Advanced Materials* 24.47 (2012), pp. 6300–6304.

[83] N. Yu, R. Blanchard, J. Fan, Q. J. Wang, C. Pflügl, L. Diehl, T. Edamura, S. Furuta, M. Yamanishi, H. Kan, et al. »Plasmonics for laser beam shaping«. In: *IEEE Transactions on Nanotechnology* 9.1 (2009), pp. 11–29.

[84] X. Ni, N. K. Emani, A. V. Kildishev, A. Boltasseva, and V. M. Shalaev. »Broadband light bending with plasmonic nanoantennas«. In: *Science* 335.6067 (2012), pp. 427–427.

[85] X. Chen, Y. Zhang, L. Huang, and S. Zhang. »Ultrathin metasurface laser beam shaper«. In: *Advanced Optical Materials* 2.10 (2014), pp. 978–982.

[86] D. Wen, F. Yue, C. Zhang, X. Zang, H. Liu, W. Wang, and X. Chen. »Plasmonic metasurface for optical rotation«. In: *Applied Physics Letters* 111.2 (2017), p. 023102.

[87] W. Ye, F. Zeuner, and X. e. a. Li. »Spin and wavelength multiplexed nonlinear metasurface holography«. In: *Nat Commun* 7 (2016), p. 11930.

[88] M. Khorasaninejad, W. T. Chen, R. C. Devlin, J. Oh, A. Y. Zhu, and F. Capasso. »Metalenses at visible wavelengths: Diffraction-limited focusing and subwavelength resolution imaging«. In: *Science* 352.6290 (2016), pp. 1190–1194.

[89] W. Chen, A. Zhu, and V. e. a. Sanjeev. »A broadband achromatic metalens for focusing and imaging in the visible«. In: *Nature Nanotech* 13 (2018), pp. 220–226.

[90] B. Yu, J. Wen, X. Chen, and D. Zhang. »An achromatic metalens in the near-infrared region with an array based on a single nano-rod unit«. In: *Applied Physics Express* 12.9 (2019), p. 092003.

[91] O. Pérez-González, N. Zabala, A. G. Borisov, N. J. Halas, P. Nordlander, and J. Aizpurua. »Optical Spectroscopy of Conductive Junctions in Plasmonic Cavities«. In: *Nano Letters* 10.8 (2010), pp. 3090–3095.

[92] V. Vlasko-Vlasov, A. Rydh, J. Pearson, and U. Welp. »Spectroscopy of surface plasmons in metal films with nanostructures«. In: *Applied Physics Letters* 88.17 (2006), p. 173112.

[93] A. Salandrino and D. N. Christodoulides. »Airy plasmon: a nondiffracting surface wave«. In: *Optics Letters* 35.12 (2010), pp. 2082–2084.

[94] S. A. Maier. *Plasmonics: fundamentals and applications*. Springer Science & Business Media, 2007.

[95] P. Zhang, S. Wang, Y. Liu, X. Yin, C. Lu, Z. Chen, and X. Zhang. »Plasmonic Airy beams with dynamically controlled trajectories«. In: *Opt. Lett.* 36.16 (2011), pp. 3191–3193.

[96] A. Minovich, A. E. Klein, N. Janunts, T. Pertsch, D. N. Neshev, and Y. S. Kivshar. »Generation and Near-Field Imaging of Airy Surface Plasmons«. In: *Physical Review Letters* 107 (11 2011), p. 116802.

[97] L. Li, T. Li, S. M. Wang, C. Zhang, and S. N. Zhu. »Plasmonic Airy Beam Generated by In-Plane Diffraction«. In: *Physical Review Letters* 107 (12 2011), p. 126804.

[98] A. Libster-Hershko, I. Epstein, and A. Arie. »Rapidly Accelerating Mathieu and Weber Surface Plasmon Beams«. In: *Physical Review Letters* 113 (12 2014), p. 123902.

References

[99] I. Epstein and A. Arie. »Arbitrary Bending Plasmonic Light Waves«.
In: *Physical Review Letters* 112 (2 2014), p. 023903.

[100] A. E. Klein, A. Minovich, M. Steinert, N. Janunts, A. Tünnermann,
D. N. Neshev, Y. S. Kivshar, and T. Pertsch.
»Controlling plasmonic hot spots by interfering Airy beams«.
In: *Opt. Lett.* 37.16 (2012), pp. 3402–3404.

[101] W. Liu, D. N. Neshev, I. V. Shadrivov, A. E. Miroshnichenko, and
Y. S. Kivshar.
»Plasmonic Airy beam manipulation in linear optical potentials«.
In: *Opt. Lett.* 36.7 (2011), pp. 1164–1166.

[102] S. Keren-Zur, O. Avayu, L. Michaeli, and T. Ellenbogen.
»Nonlinear Beam Shaping with Plasmonic Metasurfaces«.
In: *ACS Photonics* 3.1 (2016), pp. 117–123.

[103] M. Henstridge, C. Pfeiffer, D. Wang, A. Boltasseva, V. M. Shalaev, A. Grbic,
and R. Merlin. »Accelerating light with metasurfaces«.
In: *Optica* 5.6 (2018), pp. 678–681.

[104] P. Saari. »Laterally accelerating Airy pulses«.
In: *Opt. Express* 16.14 (2008), pp. 10303–10308.

[105] I. Kaminer, M. Segev, and D. N. Christodoulides.
»Self-Accelerating Self-Trapped Optical Beams«.
In: *Physical Review Letters* 106 (21 2011), p. 213903.

[106] Y. Fattal, A. Rudnick, and D. M. Marom.
»Soliton shedding from Airy pulses in Kerr media«.
In: *Opt. Express* 19.18 (2011), pp. 17298–17307.

[107] C. Ament, P. Polynkin, and J. V. Moloney.
»Supercontinuum Generation with Femtosecond Self-Healing Airy Pulses«.
In: *Physical Review Letters* 107 (24 2011), p. 243901.

[108] D. Abdollahpour, S. Suntsov, D. G. Papazoglou, and S. Tzortzakis.
»Spatiotemporal Airy Light Bullets in the Linear and Nonlinear Regimes«.
In: *Physical Review Letters* 105 (25 2010), p. 253901.

[109] A. Chong, W. Renninger, and D. e. a. Christodoulides.
»Airy–Bessel wave packets as versatile linear light bullets«.
In: *Nature Photonics* 4 (2010), pp. 103–106.

[110] H. Kondakci and A. Abouraddy. »Diffraction-free space–time light sheets«.
In: *Nature Photonics* 11 (2017), pp. 733–740.

[111] H. E. Kondakci and A. F. Abouraddy.
»Airy Wave Packets Accelerating in Space-Time«.
In: *Physical Review Letters* 120 (16 2018), p. 163901.

[112] H. E. Kondakci, M. Yessenov, M. Meem, D. Reyes, D. Thul, S. R. Fairchild,
M. Richardson, R. Menon, and A. F. Abouraddy.
»Synthesizing broadband propagation-invariant space-time wave packets
using transmissive phase plates«.
In: *Opt. Express* 26.10 (2018), pp. 13628–13638.

[113] B. Bhaduri, M. Yessenov, D. Reyes, J. Pena, M. Meem, S. R. Fairchild,
R. Menon, M. Richardson, and A. F. Abouraddy.
»Broadband space-time wave packets propagating 70 m«.
In: *Opt. Lett.* 44.8 (2019), pp. 2073–2076.

[114] C. R. Menyuk, R. Schiek, and L. Torner.
»Solitary waves due to $\chi(2):\chi(2)$ cascading«.
In: *JOSA B* 11.12 (1994), pp. 2434–2443.

[115] R. Schiek, Y. Baek, and G. I. Stegeman. »One-dimensional spatial solitary
waves due to cascaded second-order nonlinearities in planar waveguides«.
In: *Physical Review E* 53 (1996), pp. 1138–1141.

[116] R. Iwanow, R. Schiek, G. I. Stegeman, T. Pertsch, F. Lederer, Y. Min, and
W. Sohler. »Observation of Discrete Quadratic Solitons«.
In: *Physical Review Letters* 93 (2004), p. 113902.

[117] R. Schiek and T. Pertsch. »Absolute measurement of the quadratic
nonlinear susceptibility of lithium niobate in waveguides«.
In: *Optical Materials Express* 2 (2012), pp. 126–139.

[118] Y. S. Kivshar and G. P. Agrawal.
Optical solitons: from fibers to photonic crystals. Academic press, 2003.

References

[119]   J. C. Maxwell. »XXV. On physical lines of force«.
        In: *The London, Edinburgh, and Dublin Philosophical Magazine and Journal
        of Science* 21.139 (1861), pp. 161–175.

[120]   J. C. Maxwell. »VIII. A dynamical theory of the electromagnetic field«.
        In: *Phil. Trans. R. Soc.* 155 (1865), pp. 459–512.

[121]   R. M. Fano, R. B. Adler, and L. J. Chu.
        Electromagnetic fields, energy, and forces. Taylor & Francis, 1963.

[122]   W. Hansen. »A type of electrical resonator«.
        In: *Journal of Applied Physics* 9.10 (1938), pp. 654–663.

[123]   R. W. King and C. W. Harrison Jr.
        ANTENNAS AND WAVES: A MODERN APPROACH. Tech. rep. 1969.

[124]   C. A. Balanis. *Antenna theory: analysis and design.*
        John wiley & sons, 2015.

[125]   A. Alù and N. Engheta. »Tuning the scattering response of optical
        nanoantennas with nanocircuit loads«.
        In: *Nature Photonics* 2.5 (2008), pp. 307–310.

[126]   J. D. Jackson. *Classical electrodynamics.* 1999.

[127]   L. D. Landau, J. Bell, M. Kearsley, L. Pitaevskii, E. Lifshitz, and J. Sykes.
        Electrodynamics of continuous media. Vol. 8. elsevier, 2013.

[128]   N. Engheta and R. W. Ziolkowski.
        Metamaterials: physics and engineering explorations.
        John Wiley & Sons, 2006.

[129]   S. Zouhdi, A. Sihvola, and A. P. Vinogradov.
        Metamaterials and plasmonics: fundamentals, modelling, applications.
        Springer Science & Business Media, 2008.

[130]   J. Schilling. »The quest for zero refractive index«.
        In: *Nature Photonics* 5.8 (2011), pp. 449–451.

[131]   J. Kanungo1 and J. Schilling. »Experimental determination of the
        principal dielectric functions in silver nanowire metamaterials«.
        In: *Applied Physics Letters* 97.2 (2010), p. 021903.

[132] C. Menzel, C. Helgert, C. Rockstuhl, E.-B. Kley, A. Tünnermann,
T. Pertsch, and F. Lederer. »Asymmetric Transmission of Linearly
Polarized Light at Optical Metamaterials«.
In: *Physical Review Letters* 104 (2010), p. 253902.

[133] C. Menzel, C. Rockstuhl, and F. Lederer.
»Advanced Jones calculus for the classification of periodic metamaterials«.
In: *Physical Review A* 82 (2010), p. 053811.

[134] R. A. Shelby, D. R. Smith, and S. Schultz.
»Experimental verification of a negative index of refraction«.
In: *Science* 292.5514 (2001), pp. 77–79.

[135] V. G. Veselago. »The Electrodynamics of Substances with Simultaneously
Negative Values of ε and μ«.
In: *Physics-Uspekhi* 10.4 (1968), pp. 509–514.

[136] K. B. Alici and E. Özbay.
»Radiation properties of a split ring resonator and monopole composite«.
In: *Physica Status Solidi (b)* 244.4 (2007), pp. 1192–1196.

[137] J. B. Pendry. »Negative refraction makes a perfect lens«.
In: *Physical Review Letters* 85.18 (2000), p. 3966.

[138] A. Alù and N. Engheta.
»Achieving transparency with plasmonic and metamaterial coatings«.
In: *Physical Review E* 72.1 (2005), p. 016623.

[139] N. Zheludev and Y. Kivshar. »From metamaterials to metadevices«.
In: *Nature Mater* 11 (2012), pp. 917–924.

[140] I. Staude and J. Schilling. »Metamaterial-inspired silicon nanophotonics«.
In: *Nature Photonics* 11.5 (2017), pp. 274–284.

[141] A. Sprafke and J. Schilling. »9 - Non-resonant dielectric metamaterials«.
In: *Dielectric Metamaterials*.
Ed. by I. Brener, S. Liu, I. Staude, J. Valentine, and C. Holloway.
Woodhead Publishing, 2020, pp. 249–288.

References

[142] M. Gilaberte Basset, F. Setzpfandt, F. Steinlechner, E. Beckert, T. Pertsch, and M. Gräfe. »Perspectives for applications of quantum imaging«. In: *Laser & Photonics Reviews* 13.10 (2019), p. 1900097.

[143] R. W. Boyd. *Nonlinear optics*. Academic press, 2020.

[144] R. Loudon. *The quantum theory of light*. OUP Oxford, 2000.

[145] C. Gerry, P. Knight, and P. L. Knight. *Introductory quantum optics*. Cambridge university press, 2005.

[146] P. Drude. »Zur Elektronentheorie der Metalle«. In: *Annalen der Physik* 306.3 (1900), pp. 566–613.

[147] P. Drude. »Zur elektronentheorie der metalle; II. Teil. galvanomagnetische und thermomagnetische effecte«. In: *Annalen der physik* 308.11 (1900), pp. 369–402.

[148] A. Sommerfeld. »Zur elektronentheorie der metalle auf grund der fermischen statistik«. In: *Zeitschrift für Physik* 47.1-2 (1928), pp. 1–32.

[149] A. Sommerfeld and H. Bethe. »Elektronentheorie der metalle«. In: *Aufbau der zusammenhängenden Materie*. Springer, 1933, pp. 333–622.

[150] P. B. Johnson and R. W. Christy. »Optical constants of the noble metals«. In: *Physical Review B* 6.12 (1972), p. 4370.

[151] F. Bloch. »Über die quantenmechanik der elektronen in kristallgittern«. In: *Zeitschrift für Physik* 52.7 (1929), pp. 555–600.

[152] L. Rayleigh. »XXVI. On the remarkable phenomenon of crystalline reflexion described by Prof. Stokes«. In: *The London, Edinburgh, and Dublin Philosophical Magazine and Journal of Science* 26.160 (1888), pp. 256–265.

[153] E. Yablonovitch. »Inhibited spontaneous emission in solid-state physics and electronics«. In: *Physical Review Letters* 58.20 (1987), p. 2059.

[154] S. John. »Strong localization of photons in certain disordered dielectric superlattices«. In: *Physical Review Letters* 58.23 (1987), p. 2486.

[155]   T. Pertsch, P. Dannberg, W. Elflein, A. Bräuer, and F. Lederer.
»Optical Bloch oscillations in temperature tuned waveguide arrays«.
In: *Physical Review Letters* 83.23 (1999), p. 4752.

[156]   C. Sheppard. »Approximate calculation of the reflection coefficient from a
stratified medium«. In: *Pure and Applied Optics: Journal of the European
Optical Society Part A* 4.5 (1995), p. 665.

[157]   B. Osting. »Bragg structure and the first spectral gap«.
In: *Applied Mathematics Letters* 25.11 (2012), pp. 1926–1930.

[158]   J. Joannopoulos, S. Johnson, J. Winn, and R. Meade.
Photonic Crystals: Molding the Flow of Light 2nd edn Princeton Univ.
Princeton University Press, 2008.

[159]   M. Kolle. *Photonic structures inspired by nature.*
Springer Science & Business Media, 2011.

[160]   T. F. Krauss, M. Richard, and S. Brand. »Two-dimensional
photonic-bandgap structures operating at near-infrared wavelengths«.
In: *Nature* 383.6602 (1996), pp. 699–702.

[161]   A. Blanco, E. Chomski, S. Grabtchak, M. Ibisate, S. John, S. W. Leonard,
C. Lopez, F. Meseguer, H. Miguez, J. P. Mondia, et al.
»Large-scale synthesis of a silicon photonic crystal with a complete
three-dimensional bandgap near 1.5 micrometres«.
In: *Nature* 405.6785 (2000), pp. 437–440.

[162]   I. Hosein, M. Ghebrebrhan, J. Joannopoulos, and C. Liddell.
»Dimer shape anisotropy: A nonspherical colloidal approach to
omnidirectonal photonic band gaps«.
In: *Langmuir* 26.3 (2010), pp. 2151–2159.

[163]   B. E. Saleh and M. C. Teich. *Fundamentals of photonics.*
john Wiley & sons, 2019.

[164]   S. AW and J. Love. *Optical waveguide theory.* 1983.

[165]   G. T. Reed and A. P. Knights. *Silicon photonics: an introduction.*
John Wiley & Sons, 2004.

[166]   F. W. Wise. »Generation of light bullets«. In: *Physics* 3 (2010), p. 107.

References

[167] S. Minardi, F. Eilenberger, Y. V. Kartashov, A. Szameit, U. Röpke,
J. Kobelke, K. Schuster, H. Bartelt, S. Nolte, L. Torner, et al.
»Three-dimensional light bullets in arrays of waveguides«.
In: *Physical Review Letters* 105.26 (2010), p. 263901.

[168] G. P. Agrawal. *Fiber-optic communication systems*. Vol. 222.
John Wiley & Sons, 2012.

[169] H. F. Taylor and A. Yariv. »Guided wave optics«.
In: *Proceedings of the IEEE* 62.8 (1974), pp. 1044–1060.

[170] P. v. Tien. »Light waves in thin films and integrated optics«.
In: *Applied optics* 10.11 (1971), pp. 2395–2413.

[171] A. Yariv. *Optical Electronics*. 1985.

[172] F. Benabid, J. C. Knight, G. Antonopoulos, and P. S. J. Russell. »Stimulated
Raman scattering in hydrogen-filled hollow-core photonic crystal fiber«.
In: *Science* 298.5592 (2002), pp. 399–402.

[173] J.-L. Archambault, R. J. Black, S. Lacroix, and J. Bures.
»Loss calculations for antiresonant waveguides«.
In: *Journal of Lightwave Technology* 11.3 (1993), pp. 416–423.

[174] L. Novotny and B. Hecht. *Principles of nano-optics*.
Cambridge university press, 2012.

[175] R. Kingslake and R. Johnson. *Lens design fundamentals, 79*. 2010.

[176] D. Malacara and Z. Malacara. *Handbook of lens design*. Vol. 44. 1994.

[177] H. Sun. *Lens design*. CRC Press, 2017.

[178] M. Newman. *Computational physics*.
CreateSpace Independent Publ., 2013.

[179] S. S. M. Wong. *Computational methods in physics and engineering*.
World Scientific, 1997.

[180] R. B. G. Abdelwahab Kharab.
An Introduction to Numerical Methods: A MATLAB Approach.
Chapman and Hall/CRC, 2006.

[181]   D. N. Arnold.
        »Stability, consistency, and convergence of numerical discretizations«.
        In: *Encyclopedia of Applied and Computational Mathematics* (2015),
        pp. 1358–1364.

[182]   J. G. Charney, R. Fjörtoft, and J. v. Neumann.
        »Numerical integration of the barotropic vorticity equation«.
        In: *Tellus* 2.4 (1950), pp. 237–254.

[183]   R. Courant, K. Friedrichs, and H. Lewy.
        »Über die partiellen Differenzengleichungen der mathematischen Physik«.
        In: *Mathematische Annalen* 100.1 (1928), pp. 32–74.

[184]   P. D. Lax and R. D. Richtmyer.
        »Survey of the stability of linear finite difference equations«.
        In: *Communications on Pure and Applied Mathematics* 9.2 (1956),
        pp. 267–293.

[185]   J. Von Neumann and H. H. Goldstine.
        »Numerical inverting of matrices of high order«. In: *Bulletin of the
        American Mathematical Society* 53.11 (1947), pp. 1021–1099.

[186]   M. Born and E. Wolf. *Principles of optics: electromagnetic theory of
        propagation, interference and diffraction of light.* Elsevier, 2013.

[187]   O. S. Heavens. *Optical properties of thin solid films.*
        Courier Corporation, 1991.

[188]   F. Abelès. »La théorie générale des couches minces«.
        In: *Journal de Physique et le Radium* 11.7 (1950), pp. 307–309.

[189]   A. Taflove and S. C. Hagness.
        Computational electrodynamics: the finite-difference time-domain method.
        Artech house, 2005.

[190]   A. Taflove, A. Oskooi, and S. G. Johnson. *Advances in FDTD computational
        electrodynamics: photonics and nanotechnology.* Artech house, 2013.

[191]   K. S. Kunz and R. J. Luebbers.
        The finite difference time domain method for electromagnetics.
        CRC press, 1993.

[192] D. M. Sullivan. *Electromagnetic simulation using the FDTD method.*
John Wiley & Sons, 2013.

[193] A. Z. Elsherbeni and V. Demir. *The finite-difference time-domain method for electromagnetics with MATLAB simulations.*
The Institution of Engineering and Technology, 2016.

[194] Y. Liu, R. Mittra, T. Su, X. Yang, and W. Yu.
Parallel finite-difference time-domain method. Artech, 2006.

[195] A. Taflove and M. E. Brodwin.
»Numerical solution of steady-state electromagnetic scattering problems using the time-dependent Maxwell's equations«. In: *IEEE Transactions on Microwave Theory and Techniques* 23.8 (1975), pp. 623–630.

[196] J.-P. Berenger.
»A perfectly matched layer for the absorption of electromagnetic waves«.
In: *Journal of Computational Physics* 114.2 (1994), pp. 185–200.

[197] J. Van Bladel. »Some remarks on Green's dyadic for infinite space«. In: *IRE Transactions on Antennas and Propagation* 9.6 (1961), pp. 563–566.

[198] C.-T. Tai. *Dyadic Green functions in electromagnetic theory.* IEEE, 1994.

[199] R. Pregla, W. von Reden, H. Hoekstra, and H. Baghdasaryan.
»Beam propagation methods«. In: *Photonic Devices for Telecommunications.*
Springer, 1999, pp. 35–65.

[200] M. Feit and J. Fleck. »Light propagation in graded-index optical fibers«.
In: *Applied optics* 17.24 (1978), pp. 3990–3998.

[201] M. Feit and J. Fleck. »Computation of mode properties in optical fiber waveguides by a propagating beam method«.
In: *Applied Optics* 19.7 (1980), pp. 1154–1164.

[202] A. Neyer, W. Mevenkamp, L. Thylen, and B. Lagerstrom. »A beam propagation method analysis of active and passive waveguide crossings«.
In: *Journal of Lightwave Technology* 3.3 (1985), pp. 635–642.

[203] D. Yevick and M. Glasner.
»Analysis of forward wide-angle light propagation in semiconductor rib waveguides and integrated-optic structures«.
In: *Electronics Letters* 25.23 (1989), pp. 1611–1613.

[204] Y. Chung and N. Dagli.
»An assessment of finite difference beam propagation method«.
In: *IEEE Journal of quantum electronics* 26.8 (1990), pp. 1335–1339.

[205] Y. Chung and N. Dagli. »Explicit finite difference beam propagation method: application to semiconductor rib waveguide Y-junction analysis«.
In: *Electronics Letters* 26.11 (1990), pp. 711–713.

[206] R. Scarmozzino and R. M. Osgood.
»Comparison of finite-difference and Fourier-transform solutions of the parabolic wave equation with emphasis on integrated-optics applications«.
In: *JOSA A* 8.5 (1991), pp. 724–731.

[207] G. R. Hadley. »Transparent boundary condition for beam propagation«.
In: *Optics Letters* 16.9 (1991), pp. 624–626.

[208] C. Vassallo and F. Collino. »Highly efficient absorbing boundary conditions for the beam propagation method«.
In: *Journal of Lightwave Technology* 14.6 (1996), pp. 1570–1577.

[209] W. Huang, C. Xu, W. Lui, and K. Yokoyama. »The perfectly matched layer (PML) boundary condition for the beam propagation method«.
In: *IEEE Photonics Technology Letters* 8.5 (1996), pp. 649–651.

[210] E. Brigham. »The discrete Fourier transform«.
In: *The Fast Fourier Transform* (1974), pp. 91–109.

[211] G. R. Hadley. »Multistep method for wide-angle beam propagation«.
In: *Optics Letters* 17.24 (1992), pp. 1743–1745.

[212] I. Ilic, R. Scarmozzino, and R. M. Osgood.
»Investigation of the Padé approximant-based wide-angle beam propagation method for accurate modeling of waveguiding circuits«.
In: *Journal of Lightwave Technology* 14.12 (1996), pp. 2813–2822.

[213] T. Anada, T. Hokazono, T. Hiraoka, J.-P. Hsu, T. M. Benson, and P. Sewell. »Very-wide-angle beam propagation methods for integrated optical circuits«.
In: *IEICE Transactions on Electronics* 82.7 (1999), pp. 1154–1158.

[214] P. Clauberg and P. Von Allmen. »Vectorial beam-propagation method for integrated optics«.
In: *Electronics Letters* 27.8 (1991), pp. 654–655.

[215] M. Stern. »Semivectorial polarised finite difference method for optical waveguides with arbitrary index profiles«.
In: *IEE Proceedings J (Optoelectronics)* 135.1 (1988), pp. 56–63.

[216] P. Zhang, J. Prakash, Z. Zhang, M. S. Mills, N. K. Efremidis, D. N. Christodoulides, and Z. Chen. »Trapping and guiding microparticles with morphing autofocusing Airy beams«.
In: *Optics Letters* 36.15 (2011), pp. 2883–2885.

[217] P. Rose, F. Diebel, M. Boguslawski, and C. Denz. »Airy beam induced optical routing«.
In: *Applied Physics Letters* 102.10 (2013), p. 101101.

[218] A. Drezet, A. Hohenau, D. Koller, A. Stepanov, H. Ditlbacher, B. Steinberger, F. R. Aussenegg, A. Leitner, and J. R. Krenn. »Leakage radiation microscopy of surface plasmon polaritons«.
In: *Materials Science and Engineering: B* 149.3 (2008), pp. 220–229.

[219] A. E. Klein. »Scanning near-field optical microscopy: from single-tip to dual-tip operation«.
PhD thesis. Friedrich Schiller University, Germany, 2014.

[220] L. Novotny. »The history of near-field optics«.
In: *Progress in Optics* 50 (2007), p. 137.

[221] B. Hecht, B. Sick, U. P. Wild, V. Deckert, R. Zenobi, O. J. Martin, and D. W. Pohl. »Scanning near-field optical microscopy with aperture probes: Fundamentals and applications«.
In: *The Journal of Chemical Physics* 112.18 (2000), pp. 7761–7774.

[222] P. Bazylewski, S. Ezugwu, and G. Fanchini.
»A review of three-dimensional scanning near-field optical microscopy (3D-SNOM) and its applications in nanoscale light management«.
In: *Applied Sciences* 7.10 (2017), p. 973.

[223] D. Courjon. *Near-field microscopy and near-field optics*.
World Scientific Publishing Company, 2003.

[224] R. Mackenzie and G. D. Smith.
»Focused ion beam technology: a bibliography«.
In: *Nanotechnology* 1.2 (1990), p. 163.

[225] N. Bassim, K. Scott, and L. A. Giannuzzi.
»Recent advances in focused ion beam technology and applications«.
In: *Mrs Bulletin* 39.4 (2014), pp. 317–325.

[226] J.-S. Huang, V. Callegari, P. Geisler, C. Brüning, J. Kern, J. C. Prangsma, X. Wu, T. Feichtner, J. Ziegler, P. Weinmann, et al. »Atomically flat single-crystalline gold nanostructures for plasmonic nanocircuitry«.
In: *Nature Communications* 1.1 (2010), pp. 1–8.

[227] E. Krauss, R. Kullock, X. Wu, P. Geisler, N. Lundt, M. Kamp, and B. Hecht.
»Controlled growth of high-aspect-ratio single-crystalline gold platelets«.
In: *Crystal Growth & Design* 18.3 (2018), pp. 1297–1302.

[228] A. V. Singh, M. Falkner, M. Steinert, T. Kaiser, G. Isić, and T. Pertsch.
»Broadband spatio-temporal propagation characteristics of Airy plasmons«. In: *OSA Continuum* 3.7 (2020), pp. 1870–1878.

[229] W. Swiech, G. Fecher, C. Ziethen, O. Schmidt, G. Schönhense, K. Grzelakowski, C. M. Schneider, R. Frömter, H. Oepen, and J. Kirschner.
»Recent progress in photoemission microscopy with emphasis on chemical and magnetic sensitivity«. In: *Journal of Electron Spectroscopy and Related Phenomena* 84.1-3 (1997), pp. 171–188.

[230] L. Inc. *FDTD: 3D Electromagnetic Simulator*.

[231] T. Kaiser, M. Falkner, J. Qi, A. Klein, M. Steinert, C. Menzel, C. Rockstuhl, and T. Pertsch. »Characterization of a circular optical nanoantenna by nonlinear photoemission electron microscopy«.
In: *Applied Physics B* 122.3 (2016), p. 53.

[232] Y. Gong, A. G. Joly, P. Z. El-Khoury, and W. P. Hess.
»Nonlinear photoemission electron micrographs of plasmonic nanoholes in gold thin films«.
In: *The Journal of Physical Chemistry C* 118.44 (2014), pp. 25671–25676.

[233] A. Kubo, N. Pontius, and H. Petek. »Femtosecond microscopy of surface plasmon polariton wave packet evolution at the silver/vacuum interface«.
In: *Nano Letters* 7.2 (2007), pp. 470–475.

[234] L. Zhang, A. Kubo, L. Wang, H. Petek, and T. Seideman. »Imaging of surface plasmon polariton fields excited at a nanometer-scale slit«.
In: *Physical Review B* 84.24 (2011), p. 245442.

[235] C. Guan, T. Yuan, R. Chu, Y. Shen, Z. Zhu, J. Shi, P. Li, L. Yuan, and G. Brambilla. »Generation of ultra-wideband achromatic Airy plasmons on a graphene surface«. In: *Optics Letters* 42.3 (2017), pp. 563–566.

[236] A. V. Singh and T. Pertsch. »Broadband spatio-temporal propagation characteristics of Airy plasmons«. In: (submitted, 2021).

[237] K. L. Schepler, M. Yessenov, Y. Zhiyenbayev, and A. F. Abouraddy.
»Space–time surface plasmon polaritons: A new propagation-invariant surface wave packet«. In: *ACS Photonics* 7.11 (2020), pp. 2966–2977.

Publications

Publications in Peer-reviewed Journals

A. V. Singh and T. Pertsch, *Spatiotemporal propagation dyanamics of Airy plasmon pulses*, submitted, 2021.

A. V. Singh, F. Matthias, M. Steinert, T. Kaiser, G. Isič, and T. Pertsch, *Broadband spatio-temporal propagation characteristics of Airy plasmons*, OSA Continuum, **3(7)**, 1870–1878, 2020.

Conference Talks

A. V. Singh, M. Falkner, T. Kaiser, M. Zilk, M. Steinert, and T. Pertsch, *Airy Plasmon Pulses investigated by Multiphoton Photoemission Electron Microscopy (PEEM)*, The European Conference on Lasers and Electro-Optics, Munich, Germany, 2019.

A. V. Singh, M. Falkner, M. Steinert, M. Zilk, T. Kaiser, G. Isič, T. Pertsch, *Propagation characteristics of ultrawideband Airy surafce plasmons*, DoKDoK - Doctoral Student Conference on Optics, Friedrichroda, Thuringia, Germany, 2018.

Conference Posters

T. Kaiser, M. Falkner, **A. V. Singh**, M. Zilk, M. Steinert, and T. Pertsch, *Airy Plasmon Pulses investigated by Multiphoton Photoemission Electron Microscopy (PEEM)*, CLEO: QELS Fundamental Science 2019 San Jose, California United States, 2019.

M. Falkner, **A. V. Singh**, G. Isič, and T. Pertsch, *Characterization of Airy Surface Plasmon Polaritons by Photoemission Electron Microscopy*, Nanophotonics and Micro/Nano Optics International Conference, Belgrade, Serbia, 2018.

A. V. Singh, F. Matthias, M. Steinert, M. Zilk, C. Menzel, and T. Pertsch, *Investigation of Airy Surface Plasmon Polariton evolution on metallic surfaces by Photoemission Electron Microscopy*, International Conference on Fibre Optics and Photonics, Kanpur, India, 2016.

A. V. Singh, F. Matthias, C. Menzel, and T. Pertsch, *Investigation of Airy Surface Plasmon Polariton evolution on metallic surfaces by Photoemission Electron Microscopy*, DoK-DoK - Doctoral Student Conference on Optics, Eisenach, Thuringia, Germany, 2015.

Acknowledgement

This thesis has been the most important journey of my career and would have not been possible to finish it without the help of many individuals. I express my deep gratitude to all people who have been part of this journey.

I am thankful to my Ph.D. supervisor Prof. Dr. Thomas Pertsch for giving me the opportunity to pursue my research in the field of nano-optics at his group and partially funding my research work. His numerous invaluable suggestions have put my research work on the right track from time to time. I am grateful for his input in tackling challenging scientific projects and encouraging me to finish them on time. I am also thankful for the research funding offered by the 'Germany Academic Exchange Fellowship (DAAD)' award for the financial support of my stay in Germany. Prof. Pertsch's support has been crucial in receiving this fellowship.

Successful research works need mastery over a set of tools that requires extensive scientific training. I have been extremely lucky to receive such training in the beginning phase of my research career from my mentor Dr. Christoph Menzel. The training has given me a mindset of learning as my second nature. The process has distilled into me enough confidence to move step by step in the direction of achieving my academic goals and eventually contributing to the scientific community.

The research work has been a collective effort of our teamwork. I am thankful to my teammates Matthias Falkner, Matthias Zilk, Michael Steinert, and Dr. Thomas Kaiser for their help in shaping this work. Numerous discussions on contemporary research topics have widened my view and understanding of science and technology. I enjoyed the lunch and coffee-time discussions that have made the office hours fun. My special

Ehrenwörtliche Erklärung

Ich erkläre hiermit ehrenwörtlich, dass ich die vorliegende Arbeit selbständig, ohne unzulässige Hilfe Dritter und ohne Benutzung anderer als der angegebenen Hilfsmittel und Literatur angefertigt habe. Die aus anderen Quellen direkt oder indirekt übernommenen Daten und Konzepte sind unter Angabe der Quelle gekennzeichnet.

Bei der Auswahl und Auswertung folgenden Materials haben mir die nachstehend aufgeführten Personen in der jeweils beschriebenen Weise unentgeltlich geholfen:

1. Prof. Dr. Thomas Pertsch hat das Promotionsvorhaben betreut und in diesem Zusammenhang die in der Dissertation vorgestellten Themen einschließlich des "Physikalischen Modells" in Abschnitt 4.3.2 diskutiert.

2. Die experimentellen Arbeiten zu Airy-Plasmonen mittels n-PEEM wurden von Matthias Falkner durchgeführt. Die experimentellen und numerischen Ergebnisse wurden vor der Veröffentlichung gemeinsam mit Matthias Falkner, Dr. Thomas Kaiser und Prof. Dr. Thomas Pertsch diskutiert und interpretiert.

3. Die plasmonische Nanostruktur wurde von Michael Steinert hergestellt.

4. Matthias Zilk und Dr. Christoph Menzel waren maßgeblich an der Entwicklung analytischer Modelle und der Durchführung numerischer Simulationen beteiligt.

Weitere Personen waren an der inhaltlich-materiellen Erstellung der vorliegenden Arbeit nicht beteiligt. Insbesondere habe ich hierfür nicht die entgeltliche Hilfe von Vermittlungs- bzw. Beratungsdiensten (Promotionsberater oder andere Personen) in

Anspruch genommen. Niemand hat von mir unmittelbar oder mittelbar geldwerte Leistungen für Arbeiten erhalten, die im Zusammenhang mit dem Inhalt der vorgelegten Dissertation stehen.

Die Arbeit wurde bisher weder im In- noch im Ausland in gleicher oder ähnlicher Form einer anderen Prüfungsbehörde vorgelegt.

Die geltende Promotionsordnung der Physikalisch-Astronomischen Fakultät ist mir bekannt.

Ich versichere ehrenwörtlich, dass ich nach bestem Wissen die reine Wahrheit gesagt und nichts verschwiegen habe.

Jena, September 11, 2021   Amit Vikram Singh